Letter of Intent for PHENIX Reaction Plane Detector

J. Haggerty,   E. Kistenev,   R. Pak,   P. Steinberg
Brookhaven National Laboratory

A. Bickley
University of Colorado

B. Cole, J. Jia
Columbia University

P. Stankus
Oak Ridge National Laboratory

S. Esumi and Y.Ikeda
University of Tsukuba

T. Hemmick, V. Pantuev, B. Gutschow.
SUNY, Stony Brook

Y. Akiba, W. Xie
Riken-BNL Research Center, BNL

Content:

1. Overview and Physics Motivation

Event anisotropy is one of the most important observables in nucleus-nucleus collisions at RHIC. The large anisotropy amplitude, v_2, provides key evidence of the formation of a hot and dense partonic matter in Au+Au collisions at RHIC. Along with the discovery of jet suppression, the observation of large v_2 in Au+Au collisions is the basis of the conclusion in the RHIC white papers that a high density partonic medium is formed.

In early RHIC runs, the measurements of v_2 were mainly focused on that of light hadrons in low p_T ($p_T < 2$-3 GeV/c). Here the anisotropy is produced by the elliptic flow, and hydro-dynamical models can describe the data very well. Precise measurements of the v_2 as a function of p_T and particle species provide rich information on the properties of the fluid. Good agreement between the data and theory predictions of ideal hydrodynamic models indicate that the produced dense matter thermalizes very rapidly, and that the produced matter behaves almost as an ideal fluid.

Recently, we have observed that event anisotropy is not limited to light hadrons. We observed a large v_2 of single electrons from heavy quark decay. The v_2 of pi0's is not limited to the low p_T region, but retains a large value in the highest p_T region of the current data, up to ~10 GeV/c in p_T. Measurements of v_2 in rare observables such as electrons, photons, and high p_T particles can provide even richer information on the properties of partonic matter.

Figure 1.1 shows the preliminary data of the v_2 of single electrons from heavy quark decay (charm and beauty) presented at Quark Matter 2005. The data at low p_T favor the models that include quark level elliptic flow of charm. The large v_2 of charm decay electrons is a surprising discovery, and it shows that even heavy quarks participate in the collective motion of the produced matter. The data pose a challenge to the theories of energy loss and thermalization mechanism of heavy quarks in the dense matter. At high p_T, the v_2 strength seems to be reduced, and the reduction could be due to the contribution of *B* meson decay. It is expected that *B* meson decay becomes a significant source of single electrons above 2.5 GeV/c and that the v_2 of the beauty quark is small due to its large mass. Unfortunately, the statistical error in the high p_T region is rather large in this a quite interesting p_T region.

Figure 1.2 shows the preliminary v_2 data of neutral pions in various centralities. At high p_T, the value of the v_2 is somewhat reduced, but is still quite large (v_2 ~10 %) even at 7 or 8 GeV/c in p_T. In these high p_T regions, the cause of the v_2 is

considered to be due to jet quenching. Here the measurement of v_2, or the nuclear suppression factor relative to the reaction plane, provides information on the energy loss as a function of path length of fast partons in the medium. It is quite interesting to see how v_2 behaves at even higher p_T. However, as we see from the figure, the v_2 measurement in the high p_T region is limited by large statistical errors.
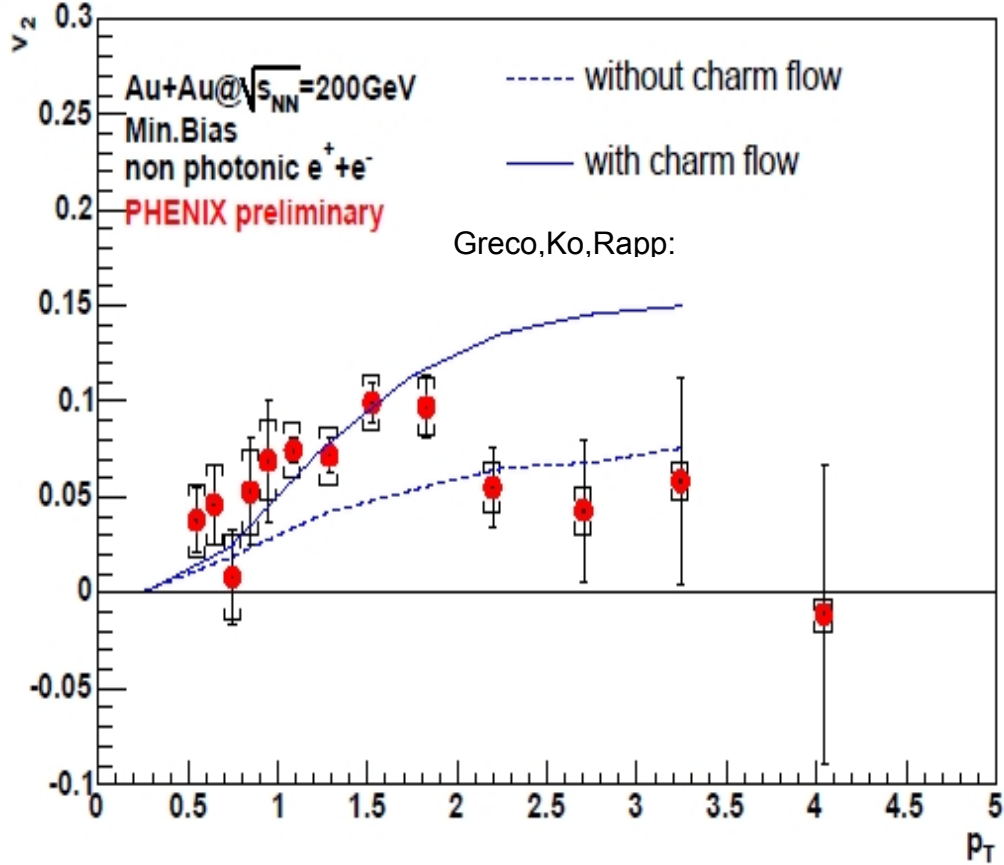

Figure 1.1: The elliptic flow strength, v2, of single electrons from heavy quark decay. The curves on the figure are charm coalescence model predictions with (solid) and without (dashed) charm quark flow.

There is growing interest in measuring the v_2 of other rare probes. Figure 1.3 shows an attempt to measure v_2 of the J/ψ particle from the RUN4 data set. If we observe a large v_2 of J/ψ, it could be strong evidence of the re-generation of J/ψ. Present data have very large statistical errors, and we can not draw any strong conclusion. The v_2 measurements of direct photons in intermediate p_T region are also very interesting. There is a theoretical prediction that jet-medium interaction can copiously produce direct photons in the intermediate p_T range. In this model, direct photon is emitted from quarks passing through the high density matter, and therefore the emission rate is larger for longer pass length of quarks in the medium.

This leads to a negative v_2 of direct photons. If a negative value of v_2 is indeed observed for direct photon in the intermediate p_T, it will be direct evidence of jet-medium interaction.

Measurements of the v_2 of these rare probes are limited by statistics. The statistical limitation of the v_2 measurements comes from two factors. One is the statistics of the signal (electrons, high pT particles, J/ψ etc) itself, and the other is the reaction plane resolution. The event anisotropy is measured relative to the reaction plane.
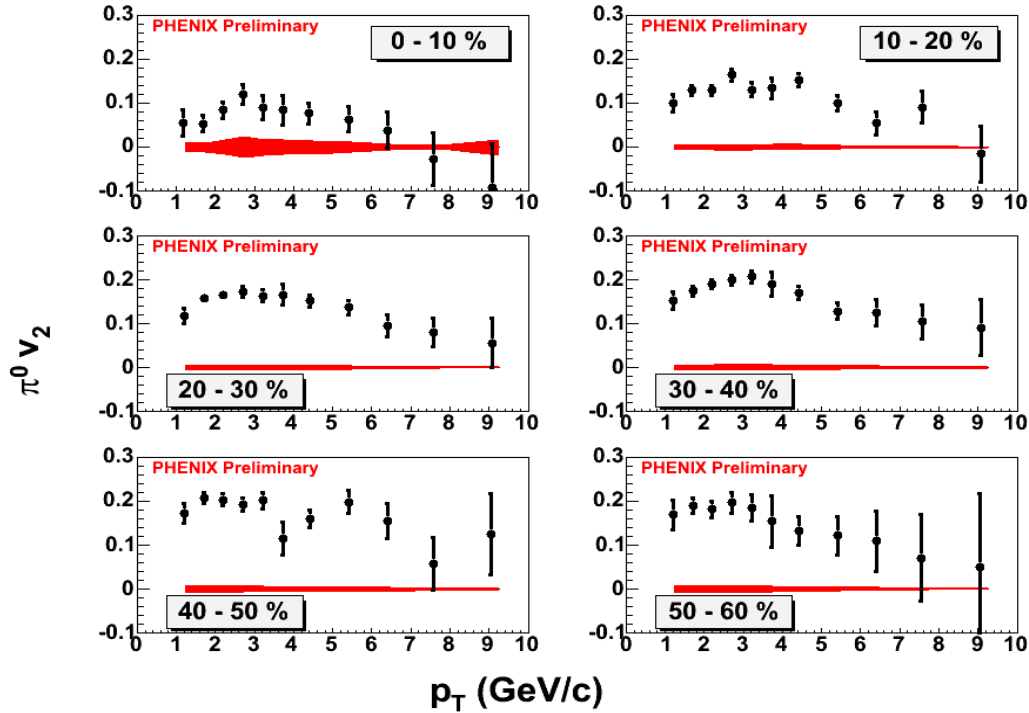

Figure 1.2: The v2 of neutral pions in Au+Au collision in various centrality bins.

Therefore, the finite resolution in reaction plane angle ψ_R smears the v_2 signal, and the observed strength v_2 (raw) is reduced.

The relation between the observed v_2 (raw) and the correct v_2 is as follows:

$$v_2 \text{ (raw)} = v_2 \text{ (true)}*<\cos2\Delta\psi> \tag{1}$$

Here $<\cos2\Delta\psi>$ is the correction factor of the reaction plane resolution, and sometimes it is simply called the "reaction plane resolution". The statistical error of the v2 measurement is approximately given by

$$\delta v_2 \text{ (raw)} \sim 1/\sqrt{(N_{signal})}. \tag{2}$$
$$\delta v_2 \text{ (true)} = \delta v_2 \text{ (raw)}/ <\cos2\Delta\psi> \sim (1/<\cos2\Delta\psi>)*1/\sqrt{(N_{signal})} \tag{3}$$

Here N_{signal} is the number of signal particles. The formula above shows that the error in the v_2 is amplified by a factor of $(1/<\cos2\Delta\psi>)$, and the statistical power of the measurement is reduced by a factor of $(1/<\cos2\Delta\psi>)^2$ due to the reaction plane resolution.
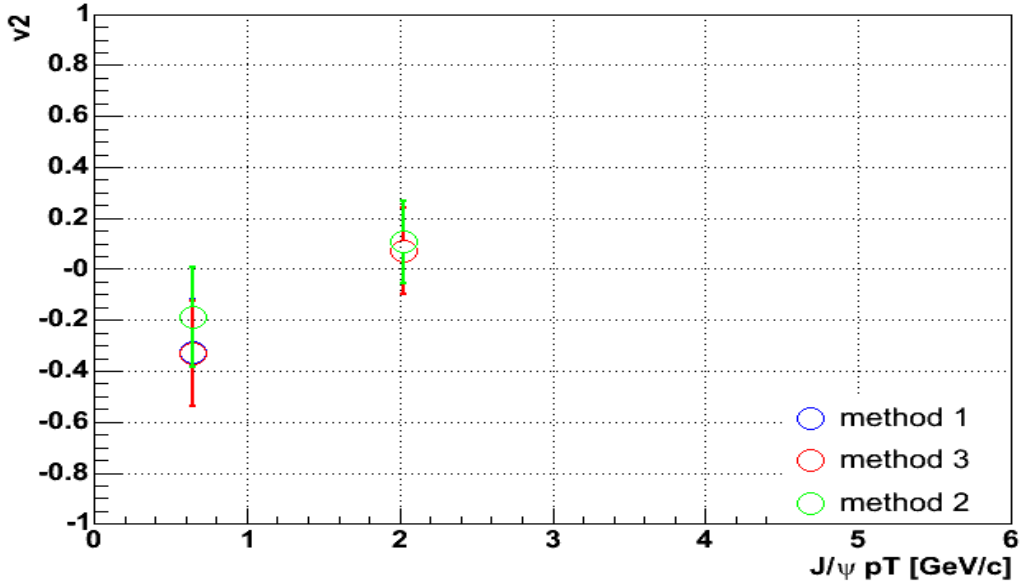

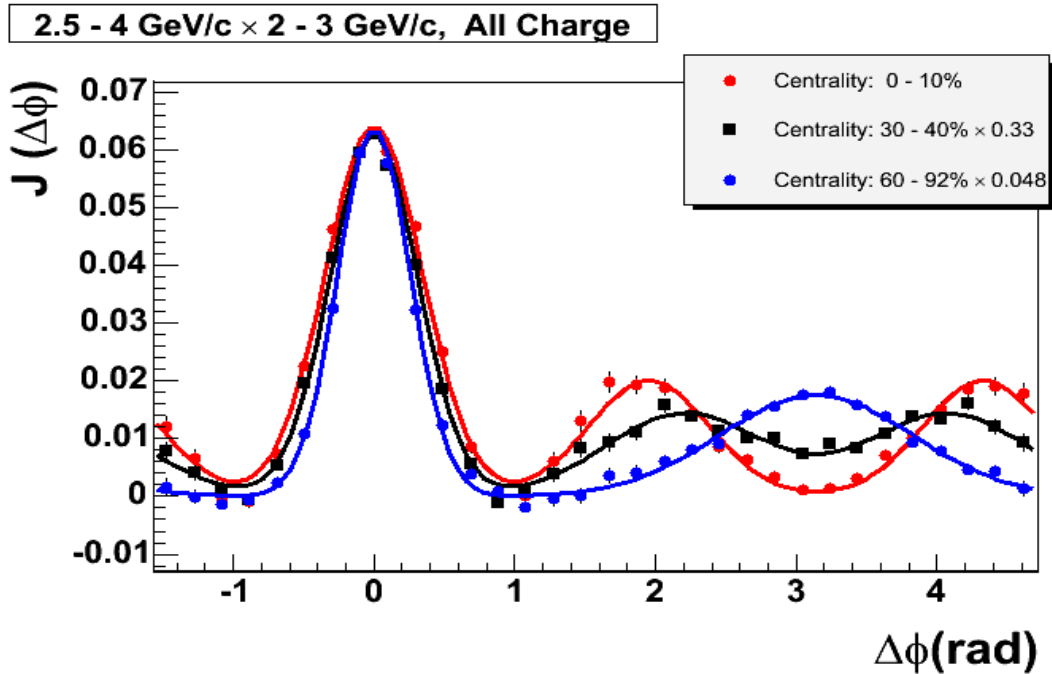Figure 1.3: The v2 of J/ψ in minimum bias Au+Au collisions.

Figure 1.4 Modification of jet shape in Au+Au collision at 200 GeV.

In PHENIX, we use the BBC to determine the reaction plane, and the values of $<\cos2\Delta\psi>$ are 0.1 to 0.4 in Au+Au collisions at 200 GeV. That is, the observed v_2 strength is only 10 to 40% of its real value, and the statistical power of the v_2 measurement is reduced by a factor of 1/6 to 1/100 compared with the ideal case, i.e. $<\cos2\Delta\psi>=1$. The situation is even worse for light ions such as Cu+Cu or at lower energy since in these collisions the reaction plane resolution provided by the BBC is even poorer. This relatively poor reaction plane resolution of the present PHENIX detector is a major limiting factor of our v_2 measurement of rare signals. Reaction plane determination by other methods, such as central arm tracks or v1 measurement by ZDC/SMD do not provide better reaction plane resolution

A good reaction plane measurement is also important for jet tomography. In figure 1.4, measurements of jet shape modification in Au+Au collisions is shown. Here, the modified jet shape is obtained carefully by subtracting the elliptic flow component from the two particle correlation function. Thus a better reaction plane determination and accurate measurements reduces the statistical and systematic error of the analysis.

In this Letter of Intent (LOI), we propose a new detector for reaction plane measurement in PHENIX. The reaction plane detector (RxPD) will have a reaction plane resolution of $<\cos2\Delta\psi>\sim0.7$ for minimum bias Au+Au collisions. The existing BBC detector has a resolution of $<\cos2\Delta\psi>\sim0.4$. Therefore, the new detector will improve the statistical power of v_2 measurements in PHENIX by about a factor of $(0.7/0.4)^2\sim3$.

2. Simulation study for a new reaction plane detector

2.1. Detector Performance

A reaction plane detector is defined and installed in PISA GEANT simulations to cover the front surface of the nosecone. The segmentation of the detector was studied and it was found that the 2nd moment reaction plane resolution was not strongly affected by the segmentation in phi above 8 segments. A converter in front of the detector was also studied in order to increase the effective statistics by including the conversion electrons from pi0's as well as to reduce low energy background from other detectors or materials. The scintillator thickness was studied to optimize the resolution. A cerenkov radiator option was also studied.

Figure.2.1.1 shows the new reaction plane detector. Figure.2.1.2 shows the side view of the detector with other elements in the IR, i.e. beam pipe and nosecone. Using a given geometry, a single particle simulation using charged and neutral pions was performed to prepare a mapping file that covers the full phase space

(rapidity, p_T, phi) first. The mapping file for the given geometry is used in the 2nd step of the simulation, which includes realistic multiplicity (charge pion and pi0) and flow (v2) depending on pT and rapidity.
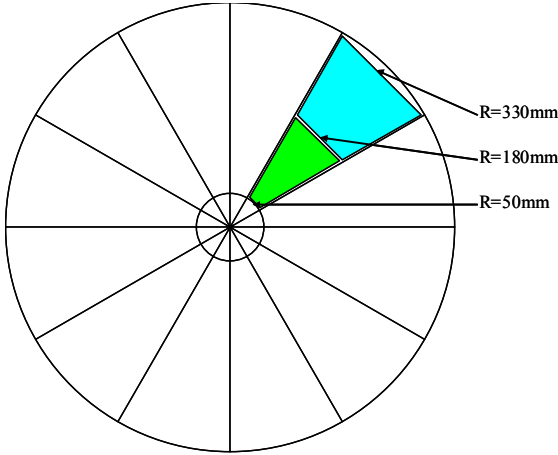

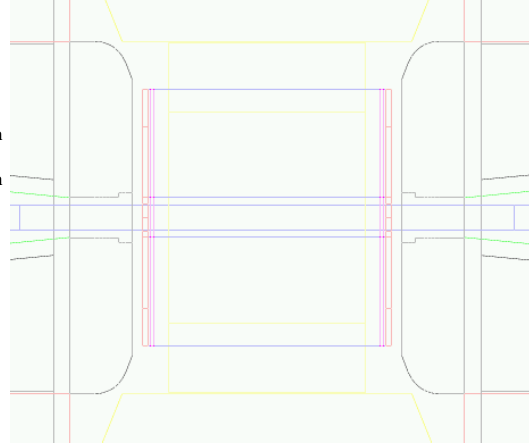Fig.2.1.1: the new reaction plane detector

Fig.2.1.2 : a side view of IR with the new r.p. detector

Figure 2.1.3 shows the mapping file information. The top-left shows the mapping ID which maps out full phase-space (rapidity, p_T, phi) with uniform distribution, minimum and maximum values and number of steps are described in the figure caption, where the 2 flat-top peak regions correspond to the 2 rapidity regions covered by this new detector. The top-right shows the x-y hit distribution on the detector, where 8 azimuthal angles have been chosen to map out [-π,π]. Only 8 steps in azimuthal angle sounds small, however the detector is symmetric in azimuth and the relative hit angle on the detector with respect to the original generated angle at vertex will also be used in the 2nd step of flow simulation described below, therefore the 8 steps was found to be reasonable to speed up simulation processes. It was also checked that an increasing this step from 8 to 32 did not affect the final results. The bottom-left shows the relative azimuthal angle of the hit on the detector with respect to the generated angle. The primary (direct) pion shows a sharp peak, where the width is given by the multiple scattering and magnetic field. While the width and tail from the secondary particles and conversion electrons from pi0's are wider and larger, they still show a strong peak at zero (original direction). The bottom-right shows the energy-loss distributions.

The 2nd step of the simulation is to include the realistic multiplicity distribution in eta, pT and phi measured in mid-central Au+Au collisions. The total multiplicity over 4π used in the 2nd step of simulation is about 2700 particles consisting equal amount of π+, π− and π0. Figure.2.1.4 shows the input flow (v2) value and multiplicity distribution as a function of p_T and rapidity. These values are taken

from experimental measurements at 200GeV Au+Au collisions and are used in the 2nd step of the flow simulation together with the above mapping file to include the
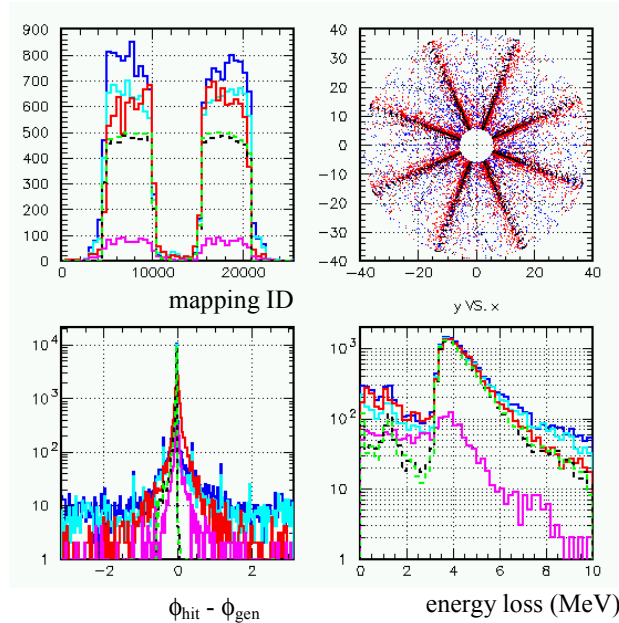
π^+ converter 0.5cm Brass
(direct π^+)
π^+ non-conv.
(direct π^+)
π^0 converter 0.5cm Brass
π^0 non-conv.

Fig.2.1.3 : mapping file generated by single particle monte-carlo,
rapidity : [-4,4 : 160]
pT : [0,4GeV/c : 20]
phi : [-π, π : 8]
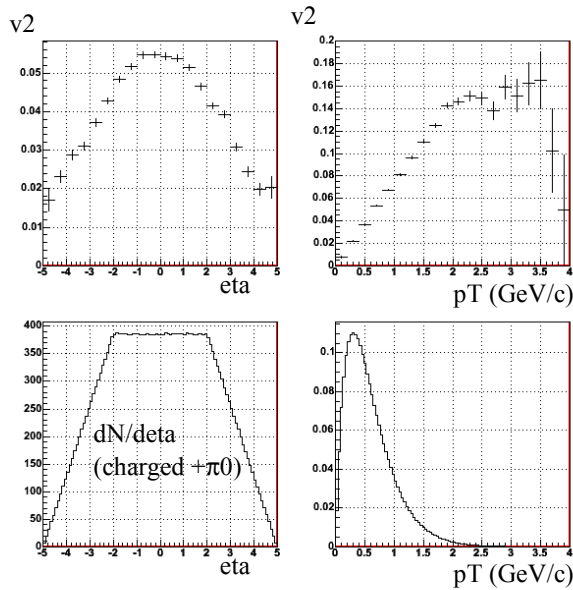
Fig.2.1.4 : input flow value and multiplicity distribution as a function of pT and rapidity, taken from the experimental measurements and used in the 2nd step of flow simulation to estimate the reaction plane resolution

detector response as well as the physical background seen by the detector. In the 1st step of PISA geant simulation, the geometry was fixed at z=+/−34cm and minimum and maximum radius of detector was 6cm and 39cm, but in the 2nd step of simulation the detector acceptance was limited between r=6cm and r=30cm, which corresponds to |eta| acceptance from 1.0 to 2.5. Figure.2.1.5 shows the x,y distribution in the detector. The left and right are the different representations of

the same figure. Figure 2.1.6 shows the relative azimuthal angle distribution with respect to the original track direction (top) and with respect to the reaction plane
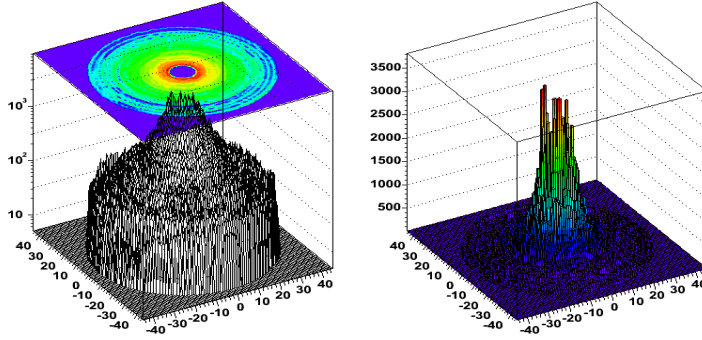
Fig.2.1.5 : x-y distribution of all the hits of the detector
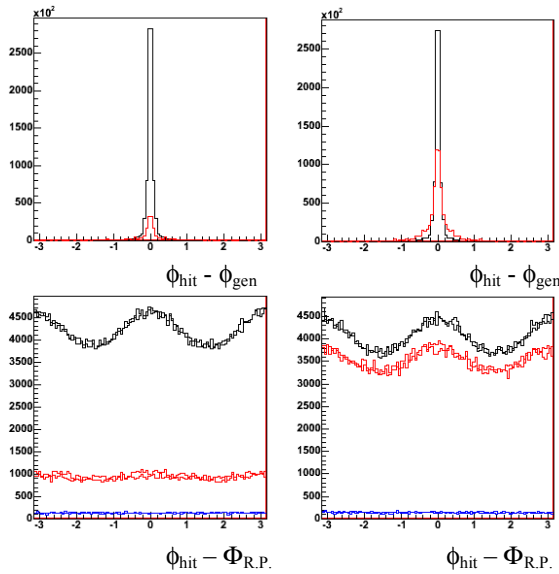
Fig.2.1.6 : (top) relative azimuthal angle distribution w.r.t. the original particle direction, (bottom) relative azimuthal angle distribution w.r.t. the reaction plane direction. (left) without converter, (right) with 0.5cm Brass converter. (black) primary tracks, (red) secondary tracks with same sign in pz and (blue) secondaries with opposite sign in pz. The red histograms in top figures include all secondaries

$\phi_{hit} - \phi_{gen}$

$\phi_{hit} - \phi_{gen}$

$\phi_{hit} - \Phi_{R.P.}$

$\phi_{hit} - \Phi_{R.P.}$

Fig.2.1.7 : (top) relative pulse height as a function of radial position of hit on the detector, (bottom) as a function of azimuthal position, with 3 different attenuation length are assumed(70, 43 and 30cm) from left to right.

relative light yield

attenuation length λ=70cm

λ=43cm

λ=30cm

radius (cm)

ϕ (rad)

direction. See details in the figure caption. Figure.2.1.7 shows the relative pulse height according to the distance of the hit from the pmt in order to include the attenuation loss of the scintillation light. The top (bottom) shows the pulse height as a function of radial (azimuthal) position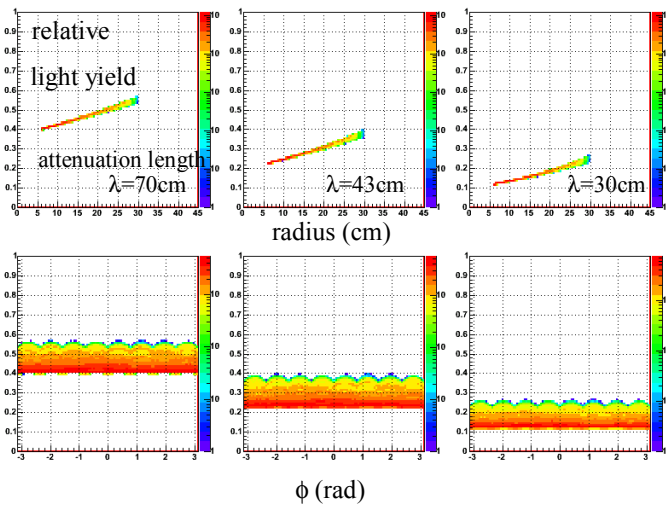 of the hits on the detector. The pmt position is assumed to be at r=70cm and the attenuation loss of light is the same for both the scintillator and the light guide. This simulation uses 8 segments in phi, therefore 8 sector structures are visible in the bottom figures. When summing up the total number of photo-electrons seen by the pmt, the linearity function is used to simulation the saturation effect of the pmt as seen in figure.2.1.8. This effect is taken from the HAMAMATSU pmt data sheet.
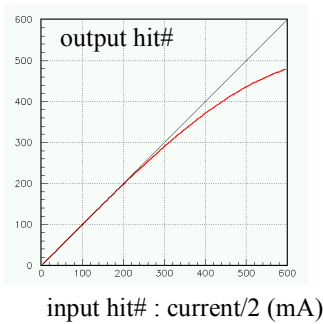

input hit# : current/2 (mA)

Fig.2.1.8 : non-linearity effect of pmt (red line) taken from HAMAMATSU pmt data sheet. Input charge (horizontal axis) vs output charge is shown in a unit of the number of MIP.

It was found that the energy loss weighting instead of the number of hits in the detector shows a significant reduction of the detector performance in terms of the resolution especially with the thin scintillator, the reason is shown in figure.2.1.9 and 2.1.10. See detail in the figure captions.

energy loss (MeV),   energy loss/4 (MeV)
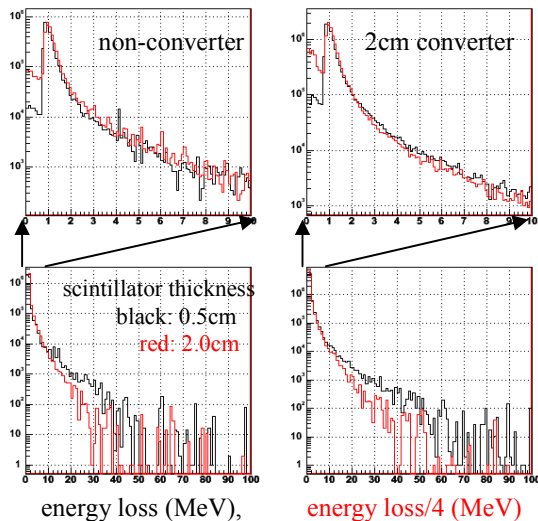
Fig.2.1.9 : normalized pulse height (energy loss) distribution per particle with (right) and without (left) converter. Top figures are expansion of the bottom figure. The horizontal scale is adjusted so that the different thickness radiator (black/red) can be compared in terms mip distribution shape. The long tail of distribution is larger for the thin scintillator, which is caused by the low energy back- ground (giving the large energy-loss tail) and the larger relative signal size in the thick radiator.

0.5cm scintillator   2.0cm scintillator

energy loss sum
per slat (MeV)

energy loss sum /4
per slat (MeV)

2cm converter
non-converter

total number of geant hits per slat

Fig.2.1.10 : The total number of geant hits per slat (horizontal) vs energy loss summation per slat (vertical). The left is with 0.5cm radiator and the right is with 2.0cm radiator. The correlation is better with the thick radiator. This also tells us that the long tail of the mip distribution affects the resolution together with Fig.2.1.9.

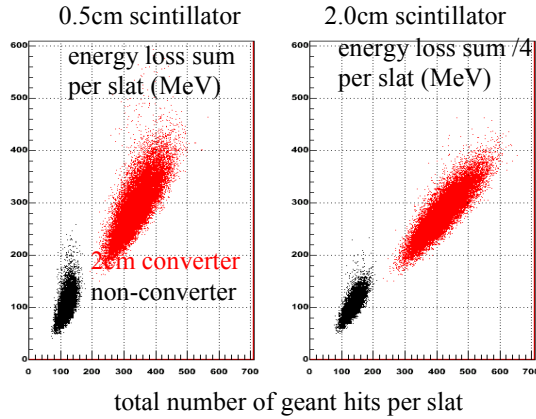If the resolution is affected largely by the tail of the mip distribution (coming from the landau distribution as well as from the low energy particle with small beta), it is clear that the cerenkov radiator might be better in terms of the mip distribution. The Figure.2.1.11 shows the correlation of the mip peak seen by the cerenkov radiator (horizontal axis) versus the one seen by the scintillation radiator (vertical axis). Both axes are normalized by the average number per track. The vertical band corresponds to the landau distribution of dE/dx energy loss and diagonal band corresponds to the correlated pulse height given by the common path length in the radiator. The number of cerenkov photons is calculated in GEANT for a given step L with the velocity β assuming the index of refraction n of a glass radiator ($N_0 * L * \sin^2\theta_C$: $\cos\theta_C = 1/n\beta$) with rather pessimistic value of $N_0=10$. The number of photoelectrons is smeared by the Poisson statistics as shown in figure.2.1.12. The same attenuation loss of light and pmt non-linearity were used for the cerenkov detector option.
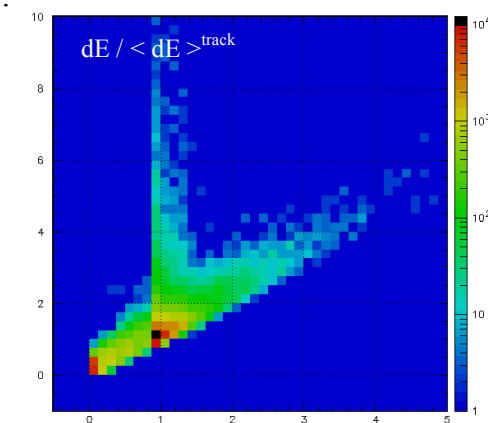

$dE / <dE>^{track}$
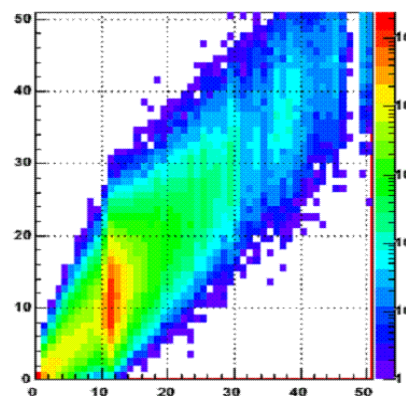
Fig.2.1.11 : Cherenkov (horizontal) vs scintillation (vertical)

Fig.2.1.12 : average Npe (input) vs Poisson Npe (output)

0.5cm radiator 2.0cm radiator 4.0cm radiator

dashed lines : dE / < dE >track
solid lines : $N_{p.e.}$ / < $N_{p.e.}$ > track

black :no-converter
red : 0.5cm Brass
blue : 2.0cm Brass
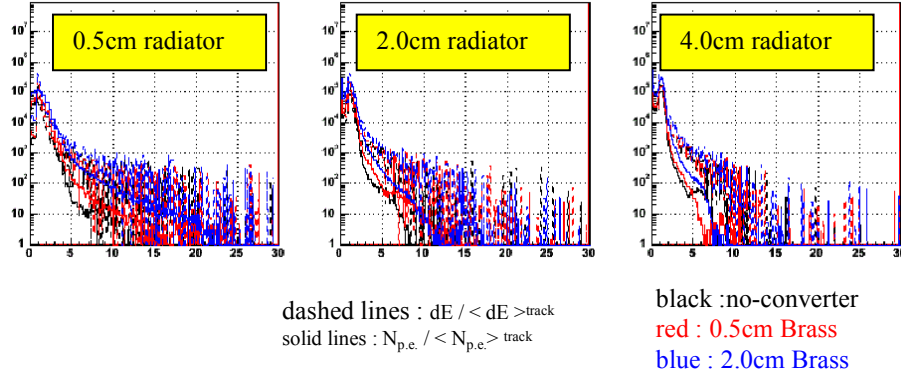
Fig.2.1.13 : The mip distributions with different radiators (left to right) and converter thicknesses (black, red and blue) are shown. The cerenkov radiator shown by the solid lines are wider around mip peak compared with the scintillator, however the larger pulse height tails are smaller. The thicker radiator also gives a smaller tail for both cases (cerenkov and scintillator).

converter thickness
0 0.5 2.0 cm

attenuation length
λ = 70 43 30 cm

$N_{p.e.}$* fac

fac=40   fac=10   fac=5

0.5cm radiator   2.0cm radiator   4.0cm radiator

dE* fac

fac=1   fac=1/4   fac=1/8

total number of geant hits per slat

Fig.2.1.14: The total number of GEANT hits per slat (horizontal) vs number of photoelectrons per slat (vertical) for the top figures and vs energy loss summation per slat for the bottom figures. From the left to the right, radiator thicknesses are varied (0.5, 2.0 and 4.0cm). The converter thickness and attenuation length are varied as described in top-middle panel.

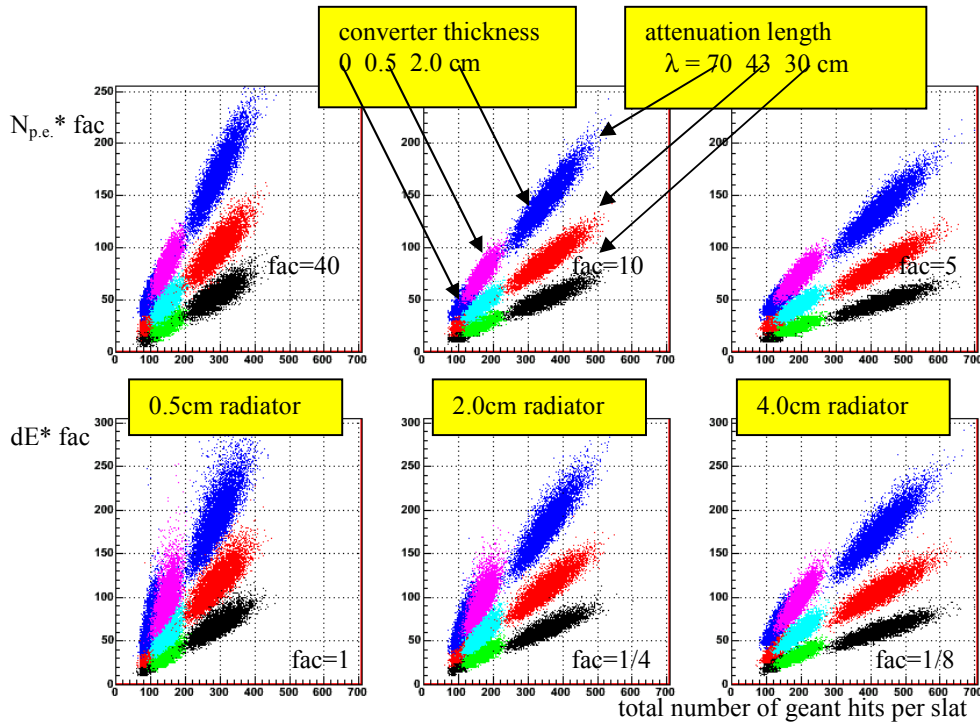Figure.2.1.13 and 2.1.14 show that the large pulse height tail is one of the sources of the worse (wide) correlation between the total number of real hits and the measured pulse height in the detector and it is the source of the worse resolution when using the dE/dx weighting of each slat to measure the reaction plane compared to the weighting based on the number of hits. Figure.2.1.15 shows the estimated reaction plane resolution, $<\cos2(\Phi_{meas.} - \Phi_{true})>$, for various cases. Different panels show different radiator and converter thicknesses, the different colors are different attenuation lengths 30, 43 and 70cm for black, red and blue, respectively. In each panel, different options of reaction plane resolution calculations are shown as a function of horizontal axis and as described in the figure caption. The option 0 and 1 are for existing central arm and bbc (combined).
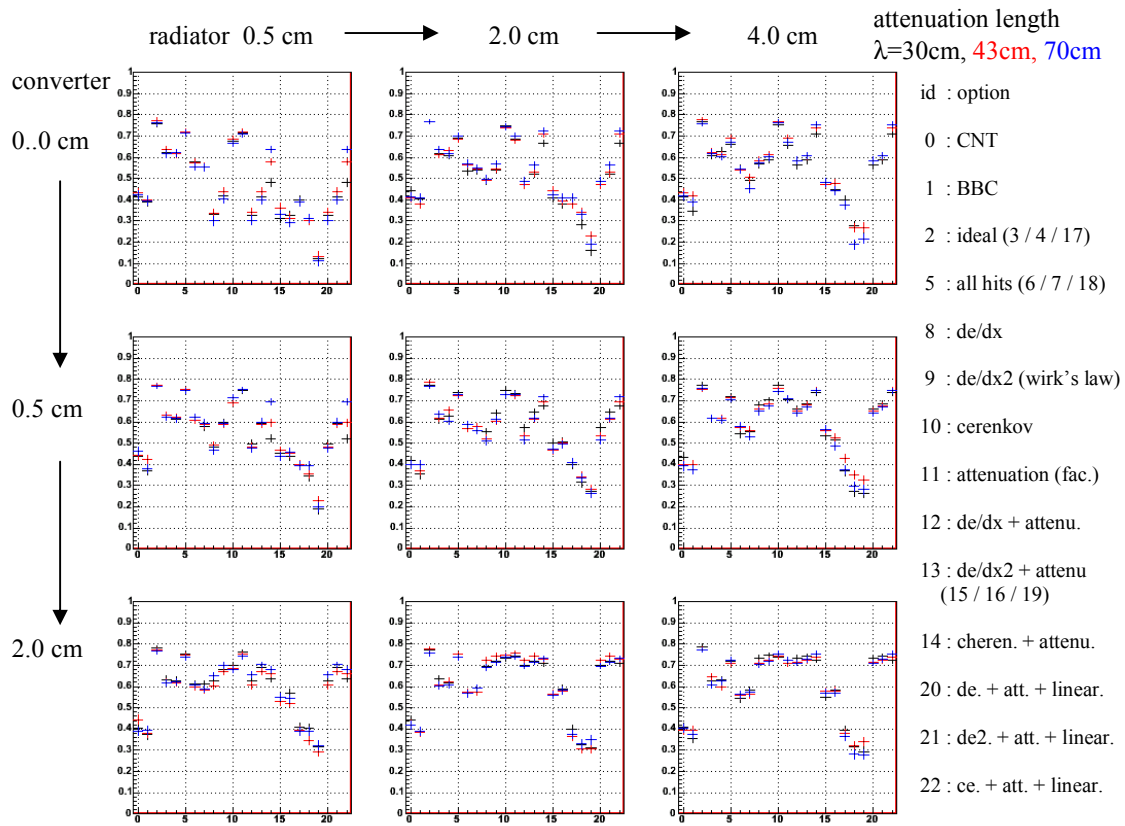

Fig.2.1.15 : reaction plane resolution estimated for various cases
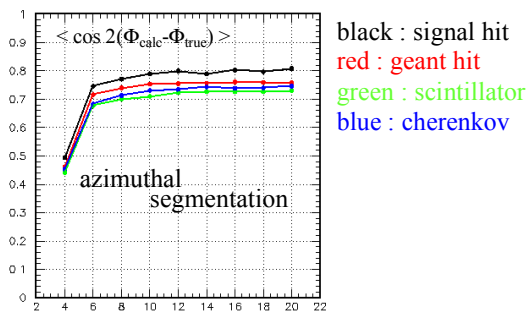

Fig.2.1.16 : reaction plane resolution as a function of detector segmentation in azimuthal angle with 2cm radiator, 2cm Brass converter and 30cm attenuation length. Down to 6-8 segmentations, the reaction plane resolution is not much deteriorated.

The option 2 is with the ideal detector, which measures all the primary charged pions, the option 3, 4 are for arm only and option 17 is the product of 3 and 4 (correlation between 3 and 4), which is a way experimentally to estimate the resolution without knowledge of true reaction plane. The option 5 is with all the GEANT hits including secondary hits, the option 6, 7, and 18 are the "option 5 version" of 3, 4 and 17. The option 8 is with energy loss weighting with scintillation detector. The option 9 includes Wirk's law, which is a saturation effect of scintillation light for a large energy loss, which effectively reduces the large tail of mip distribution, therefore the resolution is slightly improved compared with the option 8. The option 10 is with cerenkov detector option. Even with rather pessimistic N_0 value, the cerenkov radiator seems to be still better, because of the smaller tail of mip distribution. The option 11 is with the attenuation effect without including the photon counting fluctuation. The option 12, 13 and 14 include the attenuation loss of photon for option 8, 9 and 10, respectively. The attenuation loss is only visible for the cerenkov detector option with thin radiator and thin converter, where photo- electron statistics is limited. The option 15, 16, and 19 are the "option 13 version" of 3, 4 and 17. The option 20, 21 and 22 include the linearity effects of pmt for option 12, 13 and 14, respectively .Figure.2.1.16 shows the segmentation dependence of the reaction plane resolution. This shows that the reaction plane resolution does not depend strongly on the segmentation above 6-8 segmentations. Based on all above calculations, a basic design of the 8 segments per arm has been chosen for this proposal with a 2cm thick scintillation radiator plus 2cm of Brass converter in front.

The cerenkov radiator seems to be better slightly especially for the thinner radiator and thinner converter case. Although the light yield has been estimated realistically for both scintillation and cerenkov detector cases, there are still some unknown factors like light transmission. The effective acceptance can also be more clearly defined in the case of the scintillator, because of the very different light yield between the two. The light yield will not be well defined in case of cerenkov radiator, because of cerenkov light from the light guide. The difference between the two cases is also small for the thick radiator and thick converter. Therefore some more R&D studies including hardware for the future upgrade are needed in the case of the cerenkov detector. We'll make a scintillation detector with usual light guide for this year because of the time constraints.

2.2. Background Study using Hijing

The original T0 detector has been modified to fit the role of the RXP detector. It has two panels sitting at D = ±34cm with inner and out radii of Rin = 5 and Rout = 39cm, each panel has 8 sectors. Most of the results presented are for D = ±39cm, but we also performed simulations for D = ±34cm, for which we mention explicitly. Each RxPD detector panel consists of a 2cm thick scintillator (fixed), in front of which we implemented a 1.5 cm brass converter, 4cm brass converter or no converter. There is a 0.25 cm gap between the scintillator and the converter. The different setups used in this study are summarized in Table.1. For events occurring at z = 0, we can calculate the rapidity of the detector as

$$\eta = \ln\left(\sqrt{\left(\tfrac{D}{R}\right)^2 + 1} + \tfrac{D}{R} \right)$$

Thus the rapidity range is 0.79-2.61 for D = 34cm and 0.88-2.75 for D = 39cm. The background level is estimated using simulated HIJING events in PISA. Hijing events are generated with an impact parameter range of 0-2 fm. Figure 2.2.1 shows the comparison of the PHOBOS measurement of the event multiplicity with the generated HIJING events. The HIJING multiplicity reproduces the rapidity dependence of the data, but it's overall scale is about 20% higher than 0-6% central Au + Au events. This indicates that the simulation is more central than 0-6%. The total number of charged hadrons in the rapidity range covered by the RxPD is about 2000.

2.2.1 Background sources

There are many sources of background. Figure 2.2.2 shows the R:Z distribution of all background particles except for photons from the decay of $\pi 0$ or η which is called

Table 2.2.1: The detector setups in simulation.

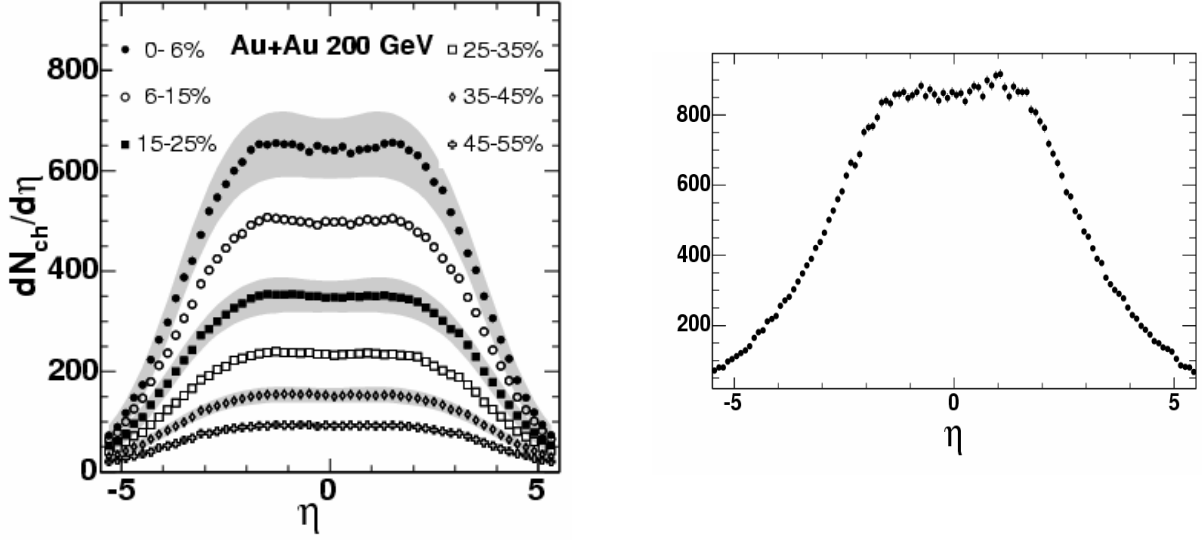| Z (cm)	R_{in} (cm)	R_{out} (cm)	Convertor(cm)
39	5	39	0
39	5	39	1.5
34	5	39	4

Figure 2.2.1: a) Charged hadron multiplicity from PHOBOS measurement, b) Event multiplicity from hijing event generator.

vertex photons and being treated as a separate source of primary particles. Most of the background comes from the pole tips, the outer frames or the RxPD detector itself. The backgrounds are composed of many different particle species and some can interact or decay more than 10 times before hitting the RxPD detector.
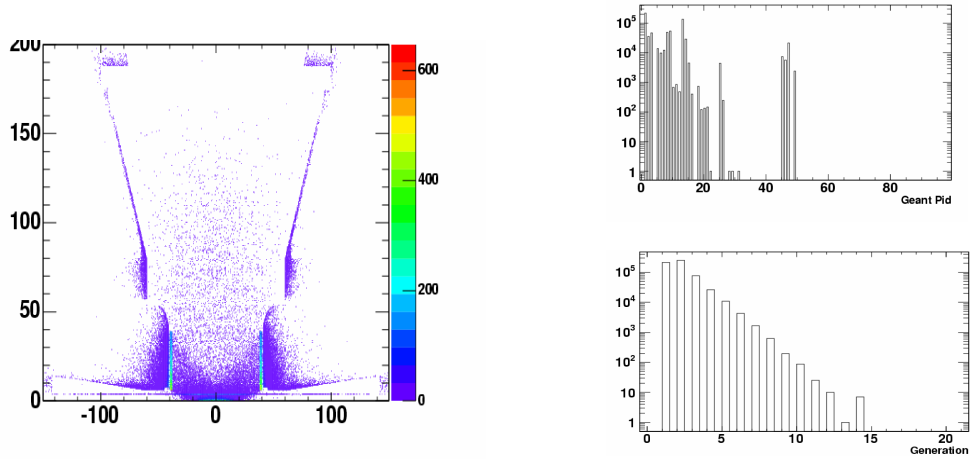

Figure 2.2.2:   (left) Origination point of all secondaries in R:Z. (right top) GEANT id of the secondaries. (right bottom) generation number.

We can better illustrate the behavior of the background by dividing them according to the shapes of their R:Z distributions as shown in figure 2.2.3. The main backgrounds are decay photons, neutrons, decay pions, protons and muons. In figure. 2.2.4, the momentum distributions for 9 different sources are shown. The primary particle and vertex photons are shown by markers and all secondaries are shown by lines of various colors. The decay photon has a sharp peak at small momentum, and the electron spectrum follows closely with the photons. The

other sources of background do not peak at zero. In particular the neutron spectrum has a sharp peak around 500 MeV, but its high pT tail merges with that of the protons. Also there is a significant contribution of alpha particles at low momentum (< 500 MeV).
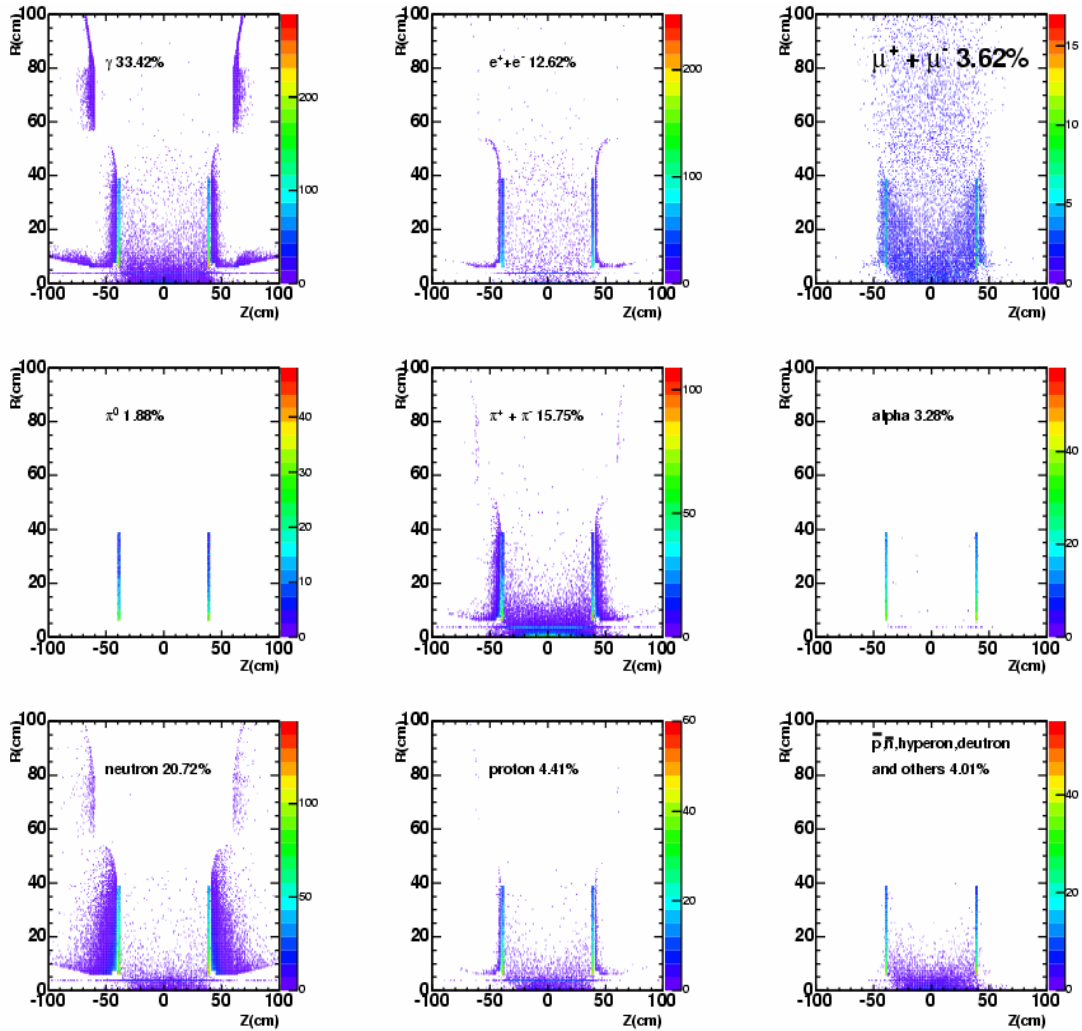

Figure 2.2.3: The background R:Z distribution and their relative fraction for 9 different sources of background.

2.2.2. Radial distribution

Figure 2.2.5a shows the hit density distribution on the X-Y plane of the detector without the converter. There is a much greater hit density at small R, and the boundaries of the 8 sectors are clearly visible along the azimuthal direction. In figure 2.2.5b, we show the radial dependence of primary particles hits, photons from primary π^0, η decay (vertex photons) and the secondary background particles. The primary hadrons has the steepest fall off as function of R that naturally reflects a steeper dependence on η. The secondary particles have a much weaker R dependence, which means a flatter η dependence. Fig.2.2.6a shows the same distribution but for charged hadrons only. In fig.2.2.6b, the distributions are
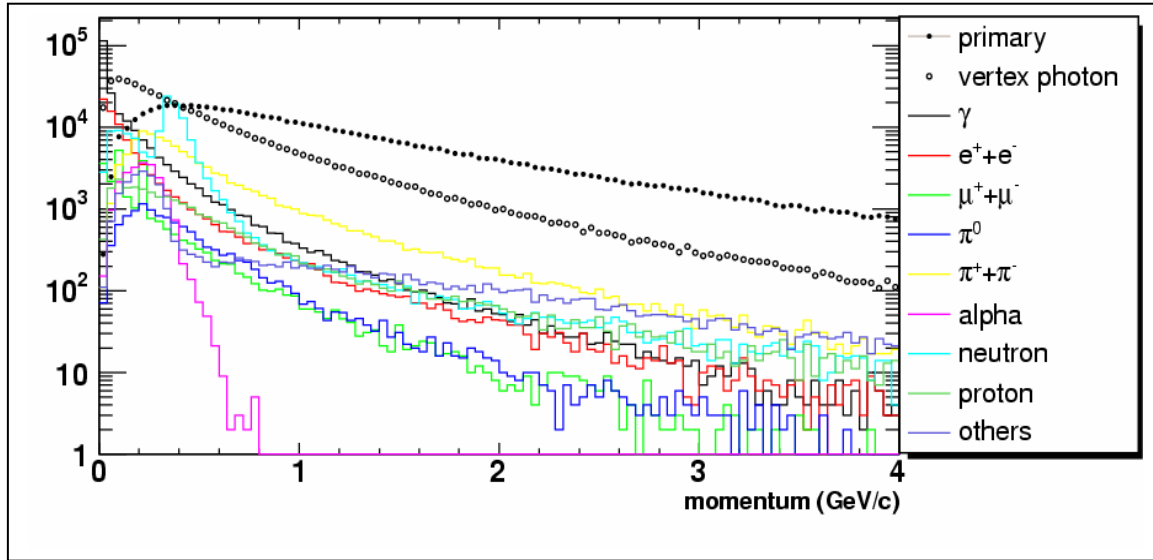
Figure 2.2.4: Momentum distribution for primary, vertex photons and other secondaries.

weighted by their dE/dx. One can see a similar R dependence in primary and background. In addition, at large R, the contribution from background is almost at the same level as the primary particles. So if one wants to reduce the relative contribution from background, it is better to go to more forward regions. From fig.2.2.6b, we can also see that there is an angular dependence of the per particle energy deposition. This is because the total path length of the particle in the scintillator depends on the angle of incidence. Figure 2.2.7 shows the average energy loss of the particle as function of R in the RXP detector. Clearly the decay particle on average has a larger energy loss than the primary hadrons, most likely due to the fact that they contain more heavy particles (such as protons) or they have a larger angle of incidence due to the additional smearing in the decay process.
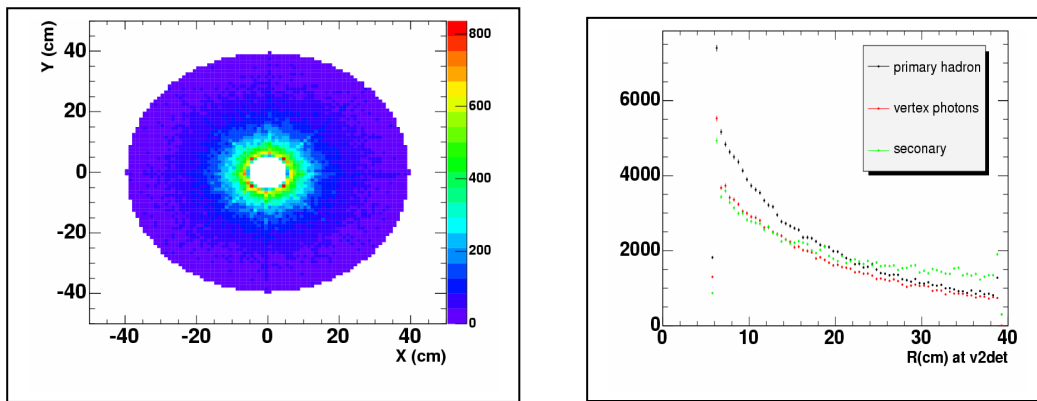
Figure 2.2.5: a) Hit distribution in X-Y plane at RXP detector, b) The radial dependence of the multiplicity distribution for primary particles, vertex photons and background.

To find out why decays have a larger energy loss than primaries, in figure 2.2.8, we compare the energy loss distributions from various sources. Clearly we see that the heavier particle in the decays (especially protons) has on average a larger energy loss, which leads to this difference.
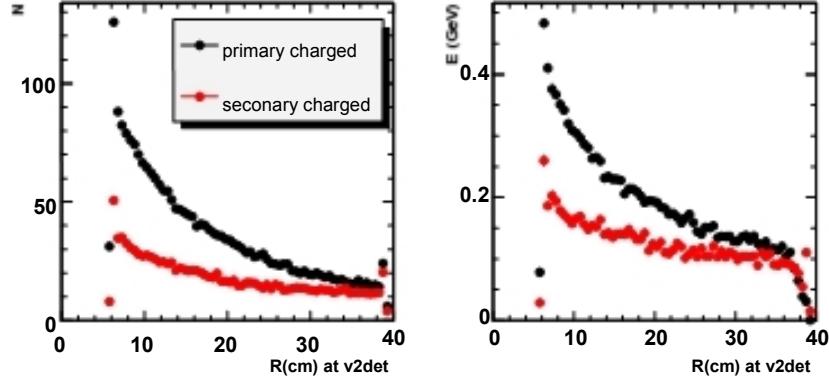
Figure 2.2.6: a) The radial dependence of the multiplicity distribution for primary charged particles and background charged particles per event. b) The dedx deposition for the two per event.
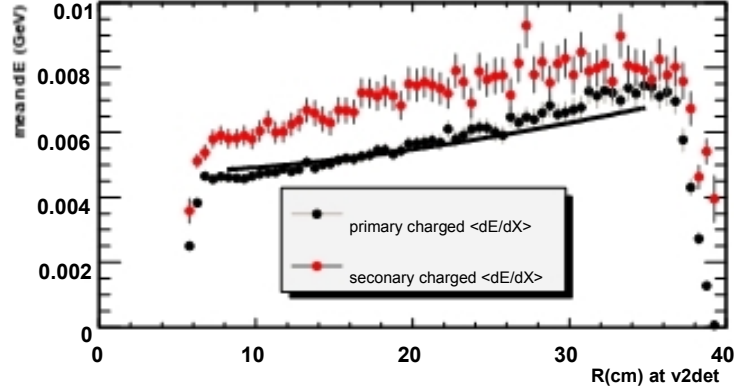

Figure 2.2.7: The average energy deposition per particle as function of R, the line is a fit taking into account the angle of incidence.

2.2.3. Distribution with converters

The converter is located in front of the scintillator. Its main purpose is to generate conversion electrons that can increase the RP resolution. Figure 2.2.9 and figure 2.2.10 shows all secondary vertex locations around the scintillator and a 1.5 cm thick converter. In the right panel, we also show the GEANT particle id distribution. Comparing with figure 2.2.2, we see a huge enhancement of photons and electron and positrons. One can see that there is a concentration of secondary sources at the lower right corner of the converter. Those are mainly very soft electrons/photons that hit the scintillator, which are mostly removed with a 100 MeV/c cut. To better illustrate this point, in figure 2.2.11 we show the density distribution in the z direction in the converter. One can clearly see the contribution from z=37.25-38.75cm where the converter sits. And the spike around 38.75cm are mostly very soft stuff (< 1MeV/c) and can be suppressed by a soft momentum cut. However these soft electrons might bias the RP calculation to whatever their parent particle are, because the RP resolution depends on the
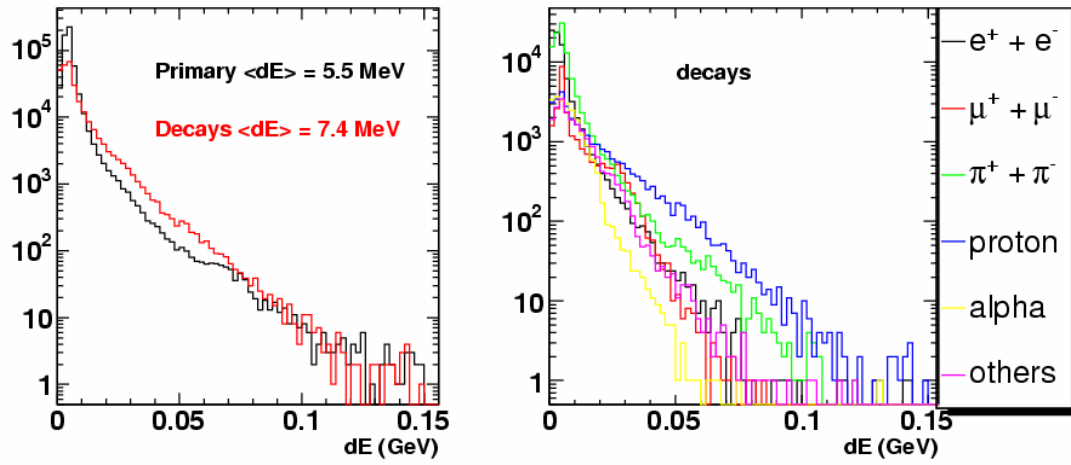
Figure 2.2.8: a) The energy loss distribution for primary and decays. b) The energy loss distributions for various sources of decays.

total number of particles and their energy deposition in the scintillator
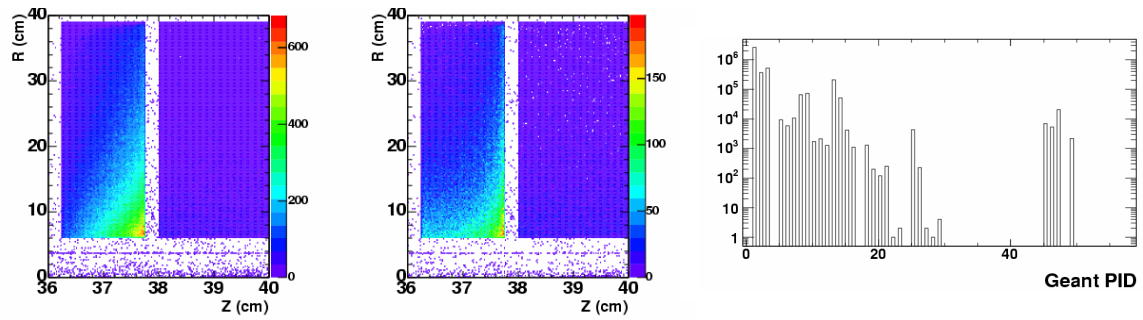
Figure 2.2.9: The vertex distribution of secondaries for a) all particles. b) particles that deposit energy in the scintillator. c) GEANT particle id distribution for secondary particles

Figure 2.2.10: Similar to figure.2.2.9, but with momentum > 100 MeV/c .

Figure 2.2.11: a) The momentum distribution of the conversions at low momentum, b) The background z vertex distribution for various momentum cuts.

With a converter the number of particles and energy deposition in the scintillator is greatly enhanced. Figure 2.2.12 shows the secondary electron momentum distribution and energy loss distribution for various converter thicknesses. One notices that the increase in electro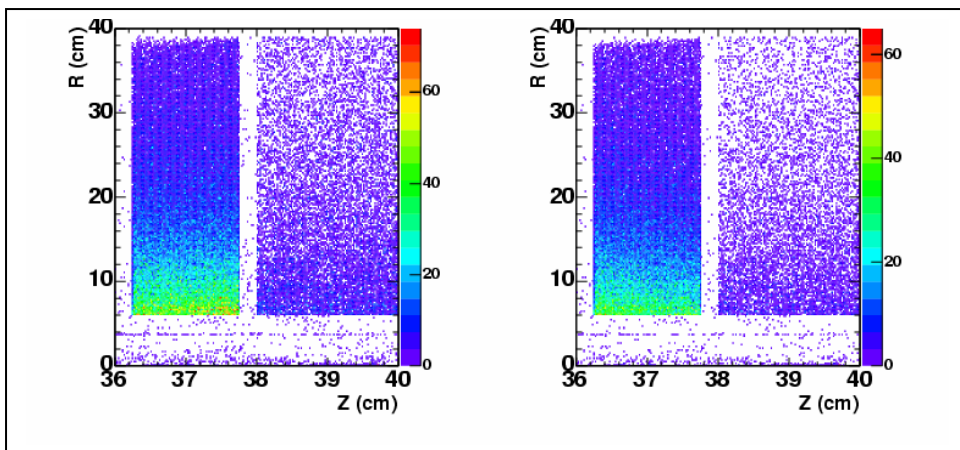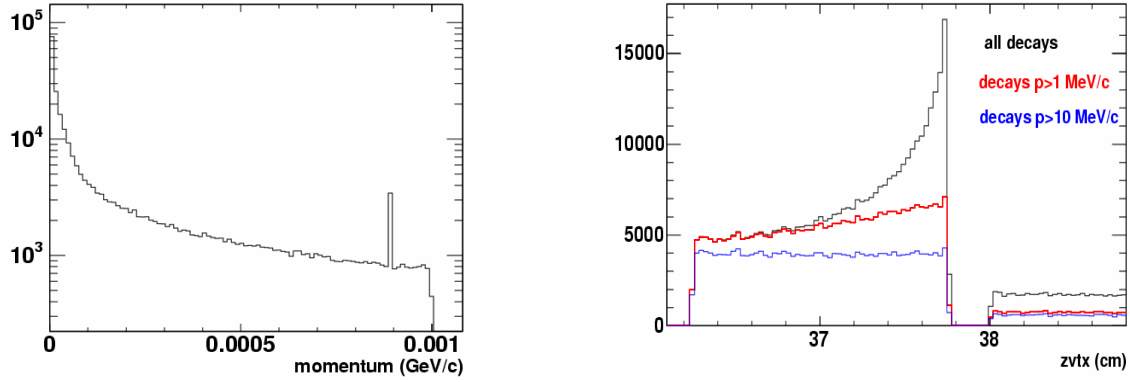n yield between the 4cm converter and 1.5 cm converter is factor of 2 but mostly concentrated at very small momentum. However, in the energy loss distribution the increase is more uniformly a factor of 2 across the whole dE distribution. The mean energy loss changes by about 10% in the three cases.
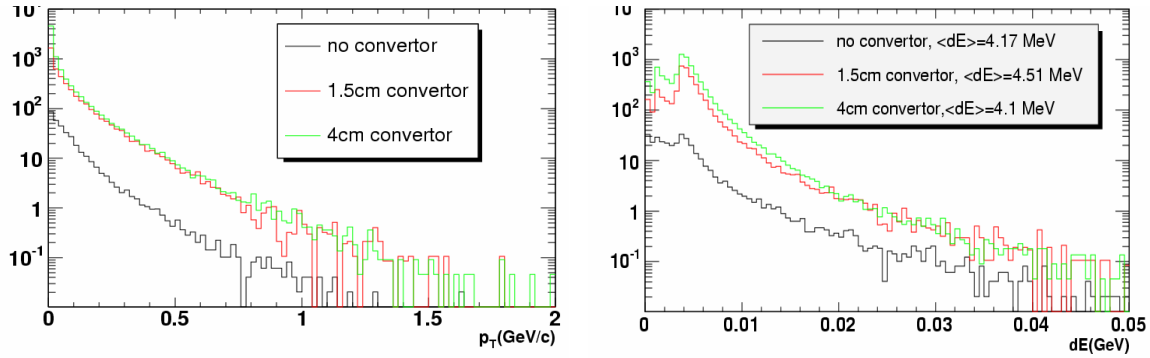
Figure 2.2.12: a) Momentum distribution and b) Energy loss distributions for various converter thicknesses.

In figure 2.2.13, we show the radial distribution of the secondaries with and without a converter. The shapes of the distributions in all three cases are similar to each other. In Table.2.2.2, we summarize the results of the detector occupancy study using events with z vertex less than 20cm. The occupancy in the detector is large, about 230 charged particles per sector without a converter and 826 charged particles with a converter. Including the converter greatly enhances the number of charged particles in the detectors, in the meanwhile the primary hadrons and vertex photon flux to the detector is reduced.

Figure 2.2.13: The radial dependence for various convertor thicknesses for a) all secondaries b) charged particle only (mostly e+e-).

Table 2.2.2: Summarizing detector occupancy.

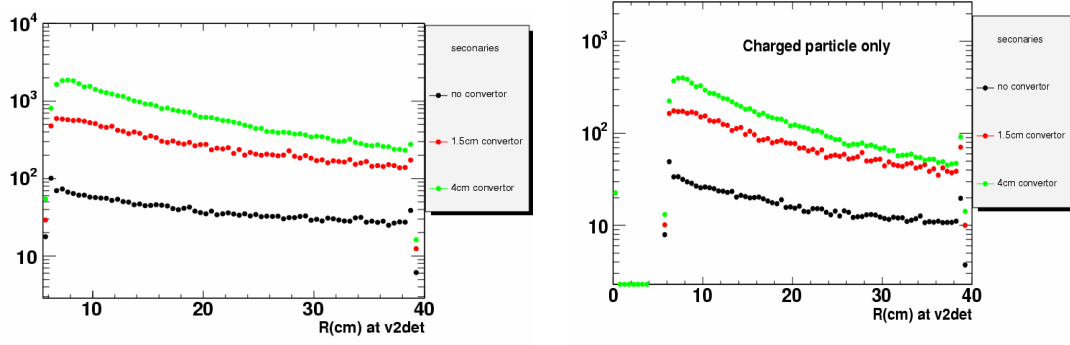|	no convertor (157 events)
per event	2882 (primary)+ 2313(vertex photons) + 2746(secondary)
per sector	180 (primary) +144(vertex photons)+ 172(secondary) = 496
Per sector charged particle only	151 (primary) + 78(secondary)=229
	1.5cm convertor (141 events)
per event	2436 (primary) +1152(vertex photons) +19081(secondary)
per sector	152 (primary) + 72(vertex photons)+ 1193(secondary) = 1417
Per sector charged particle only	132 (primary) + 391(secondary e+e-)=472
	4cm convertor (259 events)
per event	1872 (primary) + 438 (vertex photons) + 45390(secondary)
per sector	117 (primary) + 27(vertex photons)+ 2837(secondary) = 2981
Per sector charged particle only	103 (primary) + 723(secondary e+e-)=826

2.2.4. Dependence on collision vertex

Since the RxPD is only 40 cm away from z = 0cm, its pseudorapidity coverage depends on the event vertex. Figure 2.2.14 shows the vertex dependence of the charged particle multiplicity and the total energy deposition as a function of collisions vertex. We count only the signal in the RxPD at positive Z. Each point in the figure is one event. For the primary and vertex photons, we see a strong vertex dependence, especially approaching the location of the RXP detector. This simply reflects the reduction of the detector acceptance when the collision is close in z to the detector. However, there is a weaker vertex dependence from the background particles, mostly like due to the smearing effect of the scattering or decay process. If one count the total energy deposition in the detector, one notice that the dip disappeared. In fact we sees a small increase of total energy approaching the location of the RxPD detector. This is simply due to change in angle of incidence.

When the collision vertex is close to the detector, the mean angle of incidence become smaller, thus leads to a longer path length in the detector, thus a bigger energy loss per particle. This bias effect is the biggest for the primary particles and needs to be corrected through a standard calibration procedure.
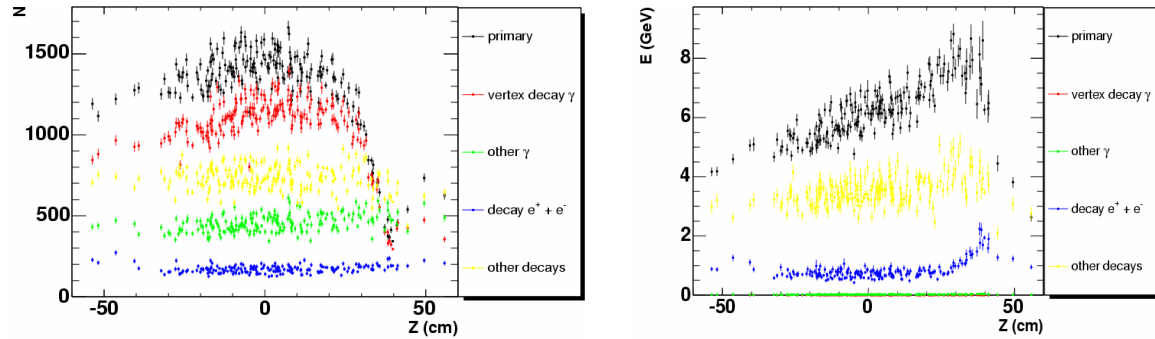

Figure 2.2.14: Vertex dependence of a) multiplicity b) total energy deposition for various sources.

We can also study the vertex with the converter. Shown in figure 2.2.15 are the results for with a 1.5 cm converter. Different from previous case, one can notice that the electrons multiplicity distribution has a similar dip around the RXP detector location. However, since the conversion happens inside the convertor, the weighting due to the angle of incidence is much weaker. Thus after weighting by the energy loss as shown in the right panel, the dip is filled a bit, but clearly is still there.
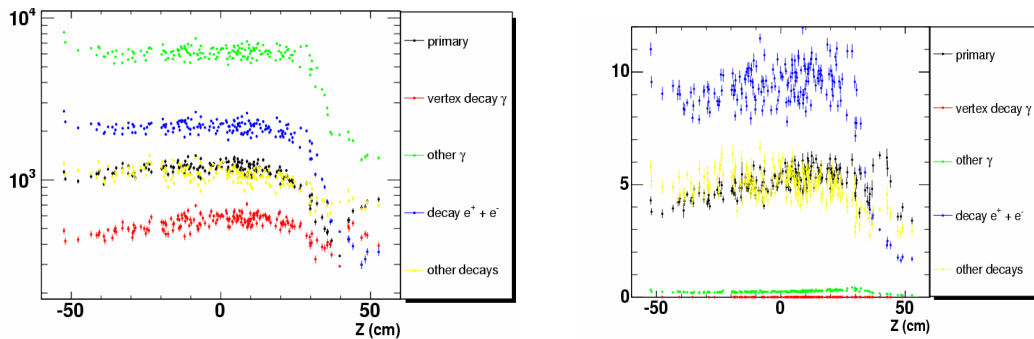
Figure 2.2.15: Vertex dependence of a) multiplicity b) total energy deposition for various sources with 1.5 cm convertor.

2.2.5. Effect of decay on RP resolution

The two dominating factors in the determination of reaction plane are 1) the size of v2 (or eccentricity) which depends on the event centrality 2) the number of primary particles in the events. To the first order, the RP resolution is determined by the detector acceptance, which directly controls the number particles that can be detected. We also decide to include a converter in front of the RXPD so that neutral particles can be used to improve the RP resolution.

Due to decay and interaction of the particle with material before reaching the detector, and also due to additional background particles, we need to estimate how

they affect the RP resolution. There are mainly five smearing effects 1) Due to bending, the ϕ at RXP is different from ϕ at vertex ($\phi 0$); 2) Decay particle ϕ is different from their parent ϕ at vertex. 3) Finite granularity of the RXP which is 45°, 4) Each decaying primary particle or through interaction with material (especially converter) can produce multiple particle, thus they have a bigger weight than other primary particles. 5) Each particle is weighted by energy deposition instead of their p_T. In current study we will evaluate the effects of the first two. Issues related to the last three items have been studied in Chapter (Shinichi). Figure 2.2.16 shows the smearing effect from bending, the two peaks around 0 represents the two opposite charged particles. The amount of bending decreases for higher momentum particles. Figure 2.2.17 shows the difference of the ϕ of the decay particle from the original primary particle at the vertex. Clearly, different types of background have different amount of smearing. The decay photons, conversion electrons and neutrons for examples have relatively large deflection and flat distribution. With just 0.5 GeV/c momentum cut, however, all distributions become rather flat.
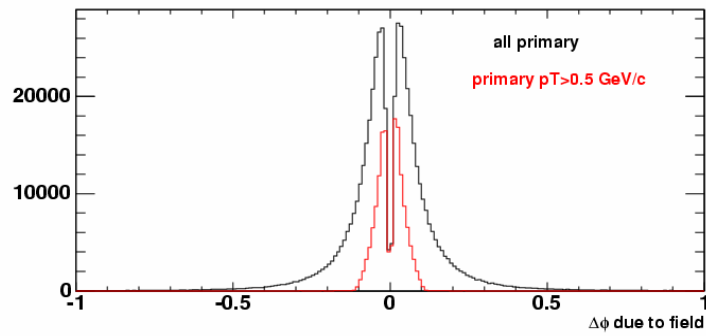

Figure 2.2.16: The difference between azimuthal angle at RXP and azimuthal angle at vertex with no momentum cut (black) and with 0.5 GeV/c momentum cut (red).
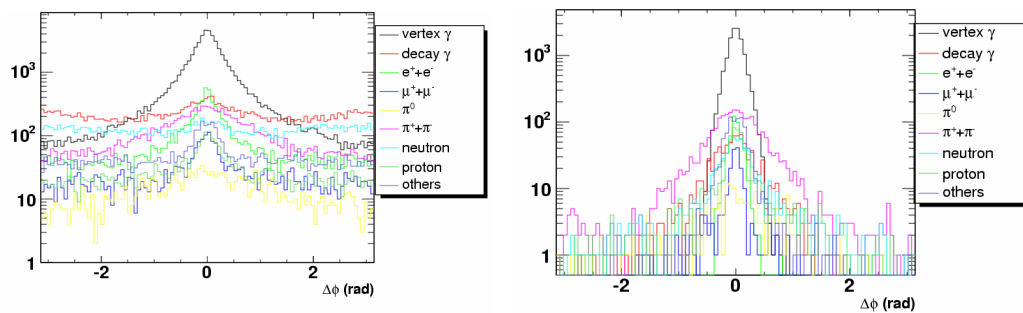

Figure 2.2.17: difference of the Á of the decay particle from the original primary particle at the vertex for various type of particles a) all, b) with momentum > 0..5 GeV/c
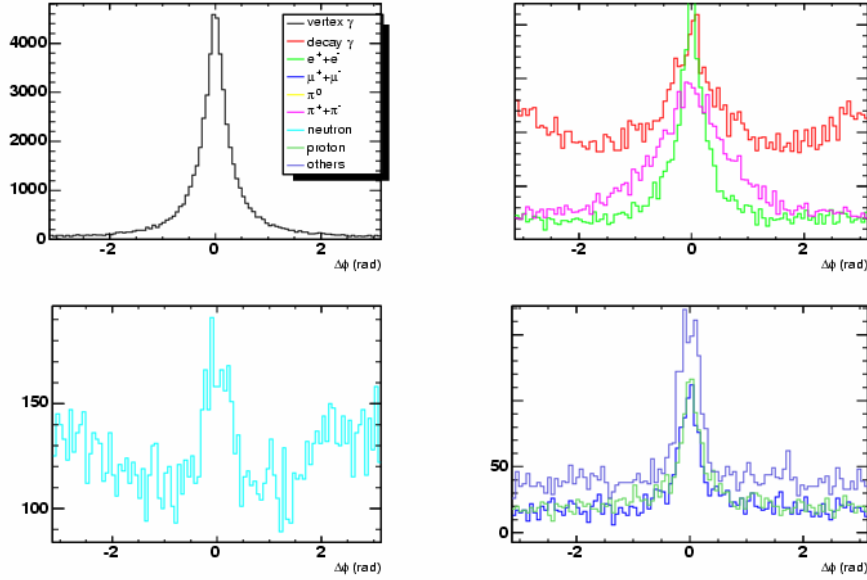
Figure 2.2.18: Same as Figure.17a, but plotted on a linear scale.

We would like to estimate the RP resolution for 20-30% Au+Au collisions, where the combination of the v2 and multiplicity would give the best resolution. However, since we haven't simulated the hijing data for mid-centrality, we only use every third particle in the event, which is leads to an event multiplicity of about $dN/d\eta = 280$ charged particles per event. We assume the background should scale with event multiplicity. For each event, we define a RP direction, for each particle with given p_T and η, we apply a weight on each primary particle as

$$w = 1 + 2v2(pT ,\eta)\cos2(\phi_0 - \psi_{RP})$$

without energy loss weighting and

$$w = (1 + 2v_2(pT ,\eta)\cos2(\phi_0 - \psi_{RP}))dE$$

with energy loss weighting. For the secondary particle, it's weight is calculated using it's corresponding primary particle's p_T ,η and $\phi0$. Thus one can determine a reaction plane direction event by event. The results of the study are presented in figure 2.2.19. What is plotted is the difference of the measured RP compared with the input RP for 1) using only primary charged particles and it's ϕ 0 at the vertex, 2) using only primary charged particles and the ϕ at the detector, 3) using all charged particles and the ϕ at the detector. 1) is the ideal case and 3) is the more realistic case. We calculate the RP angle for with and without the energy loss weighting. The obtained RP resolution is summarized in Table 2.2.3. Without dE/dx weighting, the calculated RP resolution with secondary particles are around 0.75, and including a converter seems decreasing the resolution a little bit. However, when one uses the dE/dx weighting, this decrease is not apparent anymore. Further higher statistic study is needed to clarify this.

.

In Summary we have study the background contribution using HIJING simulation. The occupancy is about 200 charged particle per sector. Including a converter decreases the number of primary particle while increasing the number of conversions and secondary particles. The occupancy reaches about 470 charged particles per sector for a 1.5cm converter, and 830 charged particles per sector for a 4cm converter. Preliminary studies indicate that the secondary decay particles improve the RP resolution

Table 2.2.3: Summarizing RP resolution for events with |z vertex| < 20cm.
no dedx weight

$<\cos2(\Psi_{mea} - \Psi_{real})>$	Primary charged ϕ_0	Primary charged ϕ	all charged ϕ
No convertor	0.80 ± 0.03	0.79 ± 0.03	$0.78 \pm 0:04$
1.5cm convertor	0.76 ± 0.03	0.76 ± 0.03	$0.84 \pm 0:04$
4 cm convertor	0.76 ± 0.03	0.75 ± 0.03	$0.84 \pm 0:04$

dE/dx weight

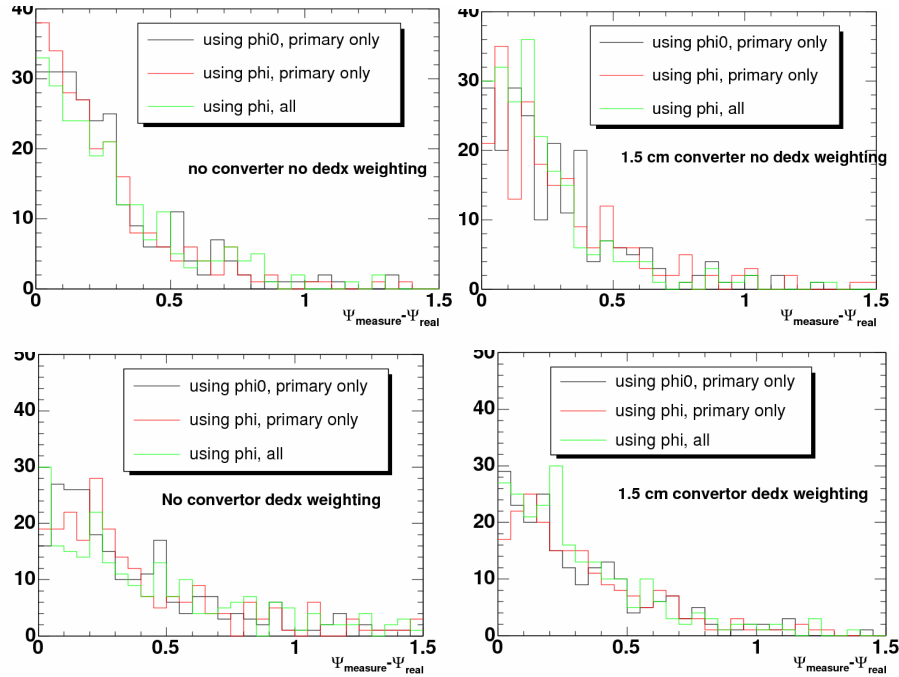| $<\cos2(\Psi_{mea} - \Psi_{real})>$	Primary charged ϕ_0	Primary charged ϕ	all charged ϕ
No convertor	0.66 ± 0.07	0.64 ± 0.06	$0.54 \pm 0:05$
1.5cm convertor	0.67 ± 0.04	0.67 ± 0.04	$0.73 \pm 0:05$
4 cm convertor	0.67 ± 0.04	0.67 ± 0.04	$0.78 \pm 0:05$

Figure 2.2.19: Simulation of three cases for a) no converter no dedx weighing, b) 1.5 cm converter no dedx weighing, c) no converter with dedx weighting, d) 1.5 cm converter with dedx weighing.

2.3 Jet auto-correlation effect

Particles from jet fragmentation are strongly correlated with each other in azimuth and rapidity. The correlation in azimuth can bias the determination of the RP direction. In heavy-ion collisions, the typical jet multiplicity, $<\sigma_{jet}>$, is small compare with the total multiplicity, N_{AA}, thus the bias effect on the RP determination is on the order of

$$\delta\Psi \sim \frac{\langle\sigma_{jet}\rangle}{N_{AA}} << 1$$

If the jet direction is uncorrelated with the RP, the presence of the jet can smear the measured reaction plane direction, leading to worsening of the RP resolution, the resulting RP angle resolution $\Delta\Psi'$ is related to the original angular resolution $\Delta\Psi$ via

$$\Delta\Psi'^2 = \Delta\Psi^2 + \delta\Psi^2$$

Typically, $\delta\Psi << \Delta\Psi$, so $\Delta\Psi'$ is very close to $\Delta\Psi$. However, $\delta\Psi$ is not random, in fact the size and the sign of $\delta\Psi$ is tightly correlated with the di-jet direction. As drawn schematically in Fig.2.3.1, the presence of jet always bias the RP angle towards the jet direction. So $\delta\Psi$ reaches maximum when the jet direction is in out of plane direction and it is close to zero when the jet direction is parallel to the RP direction. For this reason, the resulting jet rate will have a fake positive v_2, even if the original jet production is unrelated to the true RP direction. The size of the fake v_2 is proportional to $\delta\Psi$.
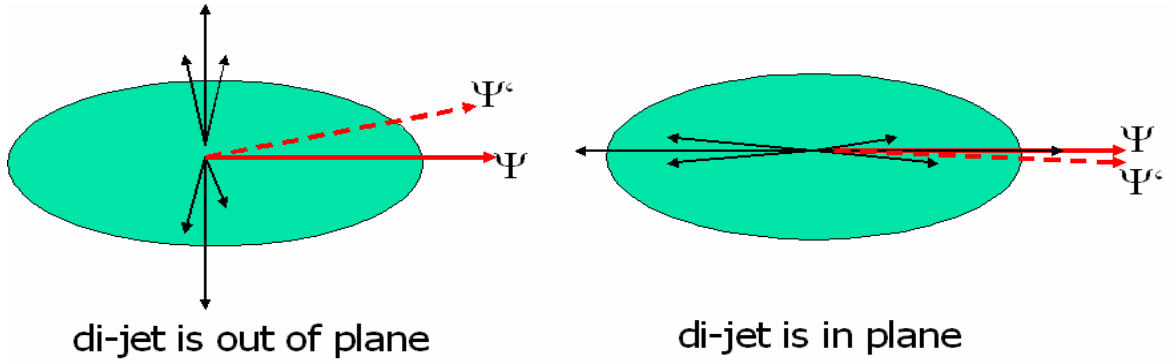

Figure 2.3.1: The effects of the dijets on the RP angle [a] determination. a) di-jet is aligned with out of plane direction, b) di-jet is aligned with in plane direction.

In Heavy-ion collisions, high p_T particles (> 2 - 3 GeV/c) come mainly from jets. The RXP detector is located away from the mid-rapidity, so it is not directly biased by the high p_T

particles. However because the swinging of the away side jet, the away side jet corresponding to near side jet at mid-rapidity can still bias the RP angle measured at forward rapidity. This effect, termed as jet autocorrelation effect, is the focus of this section.

2.3.1 Simulation framework

The bias effect is studied by embedding a di-jet into an background event with a given RP direction. We use PYTHIA event for the di-jet and use HIJING event for the background event. As shown in Fig., HIJING event reproduce the measured event multiplicity quite well. We slice the minbias HIJING event into 5% centrality bin according to the collision impact parameter as shown in Fig.2.3.2,
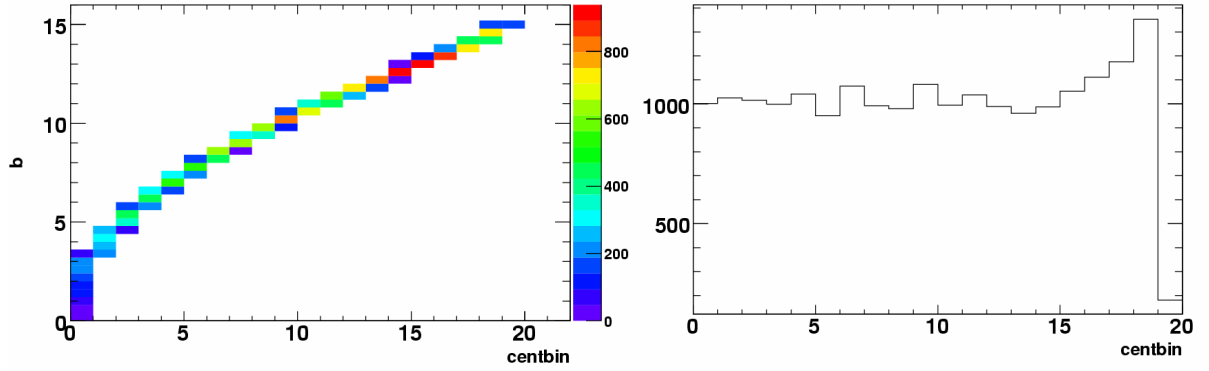

Figure 2.3.2: a) The relation between the impact parameter (B) and centrality bin. b) The number of events for each centrality bin (in 5% steps).

We assign a random RP direction for each HIJING event, and weight each particle according to,

$$w = 1 + 2v_2(p_T,\eta)\cos(2(\phi-\Psi)) \qquad (3)$$

The weight is chosen such that the resulting azimuth anisotropy of the event is consistent with the measurement v_2. The weighting is done for each centrality according to measurement. Fig.2.3.3 shows the input v_2 for various centrality bins and also the η dependence.

Each PYTHIA event is required to have a $p_T > 6$ GeV/c leading hadrons at PHENIX η acceptance $|\eta_{trig}| < 0.35$. So each of such events contains a ~ 10 GeV/c di-jets. Fig.2.3.4 shows η dependence of the particles with $p_T > 6$GeV/c, and also some of the kinematics ($\Delta\eta$) of di-jets at the near side and the away side. Note that we embed the whole PYTHIA event instead of the di-jet itself into the HIJING event, but if we assume the underlying event is isotropic in azimuth, then they don't create any bias effects.

We studied the jet autocorrelation effect for two conditions,

1) Embed the PYTHIA event into HIJING event without considering the detector response. Only charged hadrons are used for this study.
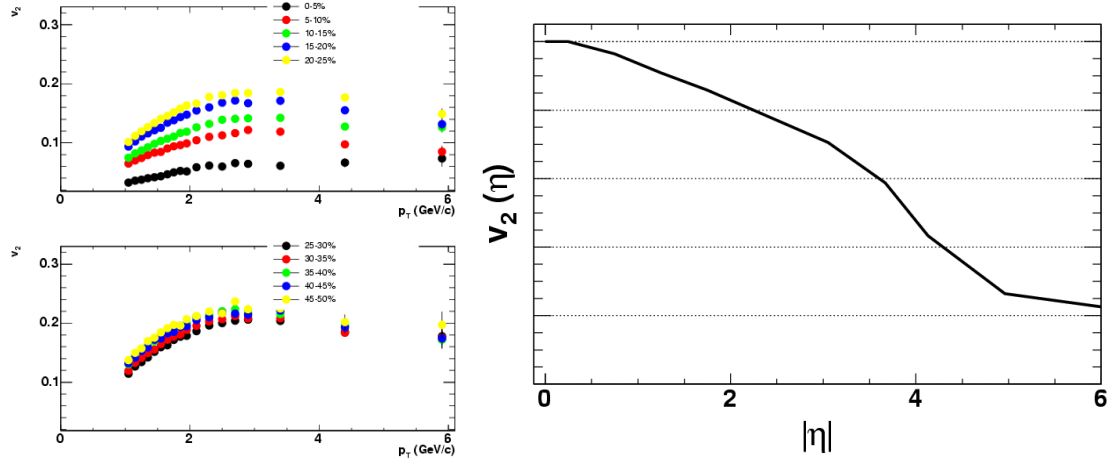
Figure 2.3.3: a) The input p_T dependence of v2 for various centrality bins. b) the ´ dependence (used for all centrality).
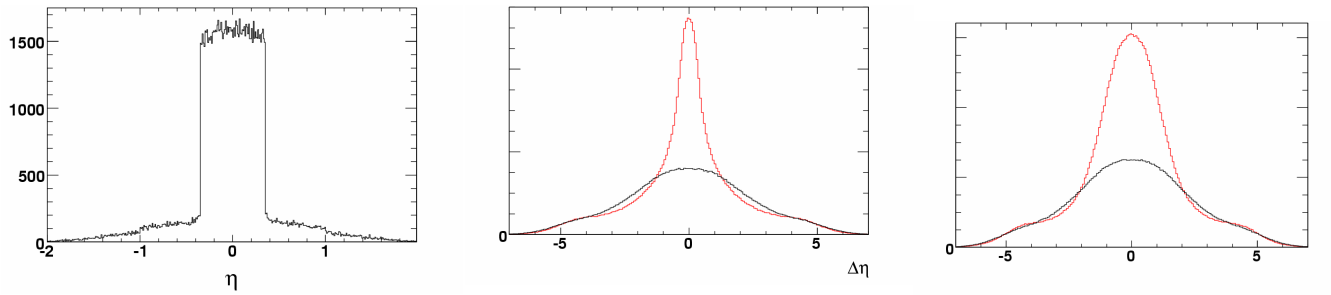

Figure 2.3.4: a). η dependence of $p_T > 6$ GeV/c particles. b). $\Delta\eta$ of triggers at the near side (red for same-event pairs, and black for mixed-event pairs), c). $\Delta\eta$ of triggers at the away side (red for same-event pairs, and black for mixed-event pairs).

2) Run full PISA simulation of the PYTHIA and HIJING event before merging the two together. All hits in Reaction Plane detectors are considered for the RP determination.

We have obtained results for both conditions, but for simplicity, we present the results mainly for the first condition, and then point out the additional information obtained for the second condition.

2.3.2 RP resolution and Fake v2

Fig.2.3.5a shows the RP angle resolution before and after merging the PYTHIA event for 25-30% centrality bin in 1:0 < $|\eta|$ < 2:8. Fig.2.3.5b shows the difference between the two RP angles, i.e $\delta\Psi$ in Eq.1. Clearly, the $\delta\Psi$ is so small that it does not affect the final RP resolution.

The centrality dependence of the RP resolution is shown in Fig.2.3.6, calculated as the average of the cosine of the two time of the difference between the measured RP angle and the true RP angle: $<\cos2(\Psi_{measure} - \Psi_{true})>$. As one can see the centrality dependence have the characteristic shape, it peaks around centrality bin 4-5 (20-30%), and is small
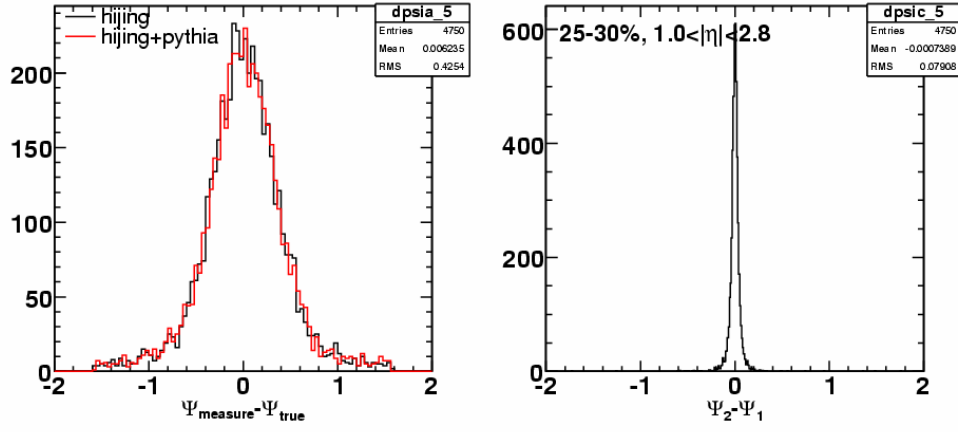
Figure 2.3.5: a) The RP angle residual distribution for HIJING (black) and HIJING+PYTHIA (red) in 25-30% centrality. b) The difference of the RP angle between HIJING and HIJING+PYTHIA .

for both central and peripheral bin. The resolutions after including the PYTHIA event, indicted by the open circles, are slightly worse But the deviation is only significant for the very peripheral bins.
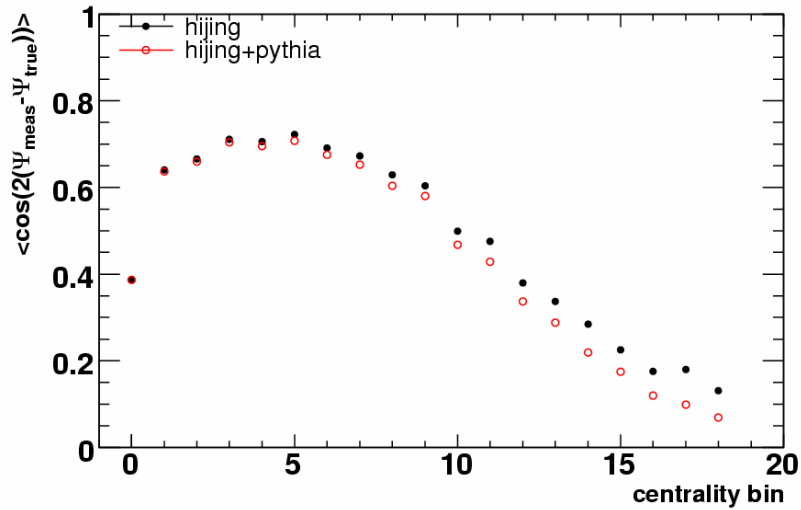
Figure 2.3.6: Centrality dependence of the RP resolution for charged hadron in $1.0 < |\eta| < 2.8$. Close and open symbols represents the using RP from HIJING events and HIJING+PYTHIA, respectively.

Fig.2.3.7 shows the effects of the fake v_2 due to the bias on the RP angle determination for two centrality bins (top: 20-25%, bottom: 60-65%). We plot the difference of the angle between trigger hadron at mid-rapidity and the measured RP angle. The left panels show that when the RP from only HIJING events are used, the distribution of the triggers are essentially flat as expected. While the distribution of the triggers developed some v_2 shape when the RP angle from the merged event are used. In addition, we can see the fake v_2 for 60-65% are significantly larger than that for 20-25%, presumably due to the smaller HIJING multiplicity in 60-65% bin.
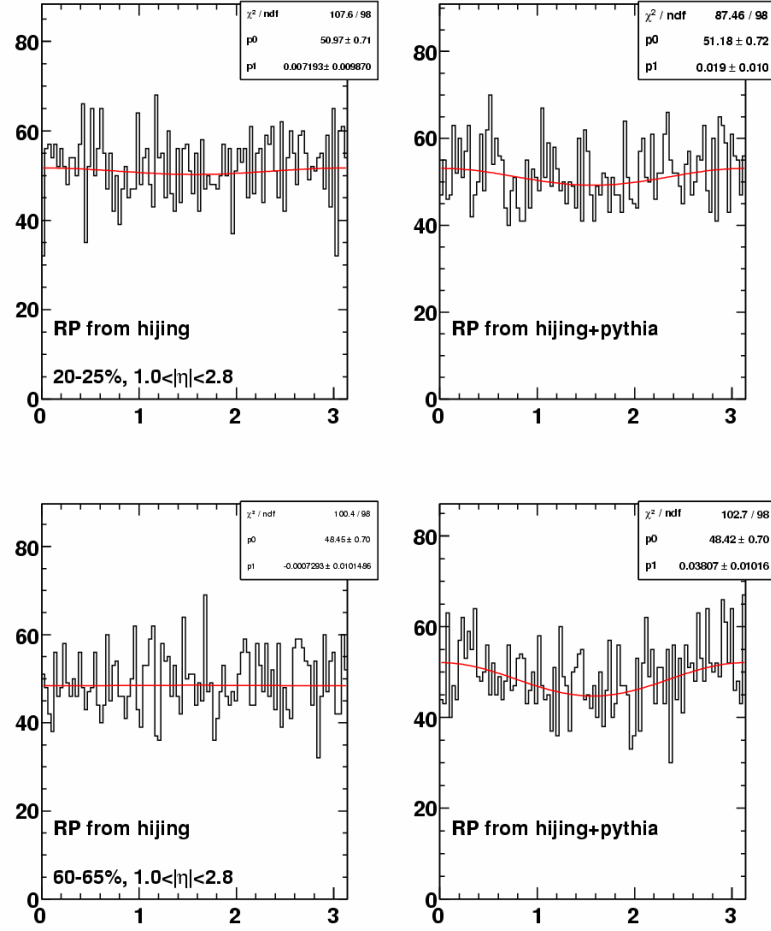
Figure 2.3.7: The distribution of the triggers at mid-rapidity relative to the RP determined by the charged hadrons at $1.0 < |\eta| < 2.8$ for two centrality bins. Top row:20-25%, bottom row: 60-65%. Left panel: using RP from HIJING. Right panel: using RP from HIJING+PYTHIA.

We can plot this fake v_2 as function of centrality as shown in Fig.2.3.8a. We see the fake v_2 is on the order of 2% in central collisions and increase to more than 10% for peripheral bin. We also show the v_2 using the HIJING event only, which is consist with zero as expected. There are some non-statistical fluctuation since we reuse the HIJING event several times in the embedding due to limited HIJING statistics. So in fact the difference between the two set of data points are better measure of the true fake v_2. These differences are shown in Fig.2.3.8b. Note that, the fake v_2 is still need to be corrected by the RP resolution to get the final v_2.

2.3.3 Dependence on the jet multiplicity

It is well known that the jets are modified in Heavy-ion collisions, it was observed by both PHENIX and STAR experiments that both the shape and the yield of the away side jet are modified at RHIC. And these modifications are found to be strongly depends on the p_T.

Figure 2.3.8: a) Centrality dependence of fake v_2 using the RP from HIJING (open circles) and HIJING+PYTHIA(closed circles). b) The difference between the two.
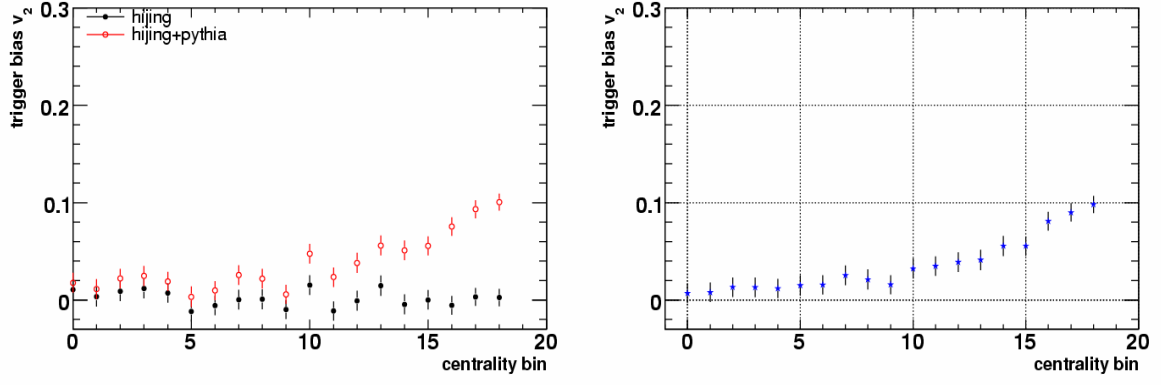
For example, the jet shape are found to be strongly broadened at low p_T but is relatively unchanged at high p_T ; The jet yield is enhanced at low p_T but is suppressed at high p_T . Jets with higher multiplicity would introduce a larger auto-correlation effect.

This effect is estimated by weighting the jet multiplicity by factor of 2 in the calculation of the RP angle. Fig.2.3.9 shows the results for one rapidity window ($1.0 < |\eta| < 2.8$). Comparing with Fig.2.3.6 and Fig.2.3.8, we can see the both the change in the RP resolution and fake v_2 are approximately doubled.
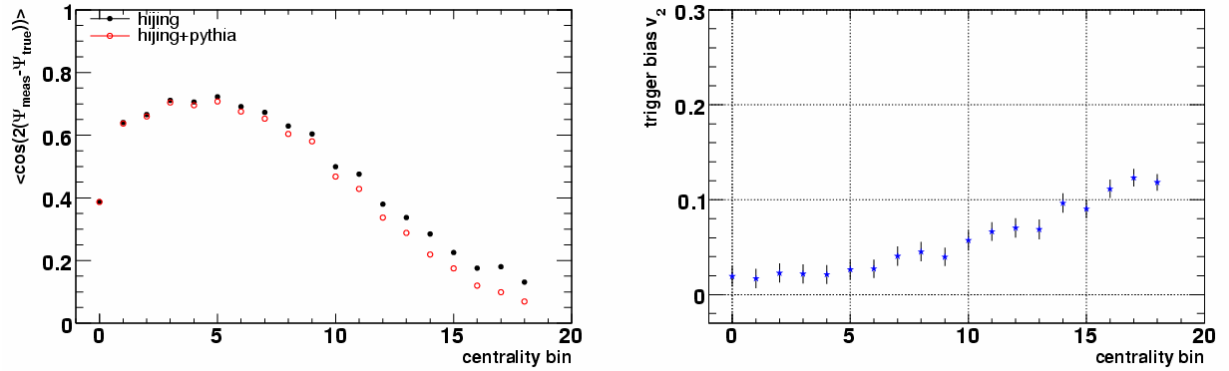
Figure 2.3.9:

2.3.4 Rapidity dependence

We studied 8 difference rapidity windows for the auto-correlation effect: 0.4-2.8, 0.6-2.8, 0.7 2.8,0.8-2.8, 1.0-2.8, 1.5-2.8, 2-2.8, 3-4. The number of particles from PYTHIA embedded into HIJING events significantly decrease towards high rapidity window (see Fig.2.3.10), but in the meanwhile, the multiplicity from HIJING also decrease, leading to a reduction of the RP resolution. However since the jet is trigged at mid-rapidity, we expect the fake v_2 should decrease as one moves away from mid-rapidity. Fig.2.3.11 shows the fake v_2 .

The two most important quantities, RP resolution and Fake v_2, are summarized in Fig.2.3.12, Fig.2.3.14. The ideal rapidity window would be the one that retains reasonable RP resolution
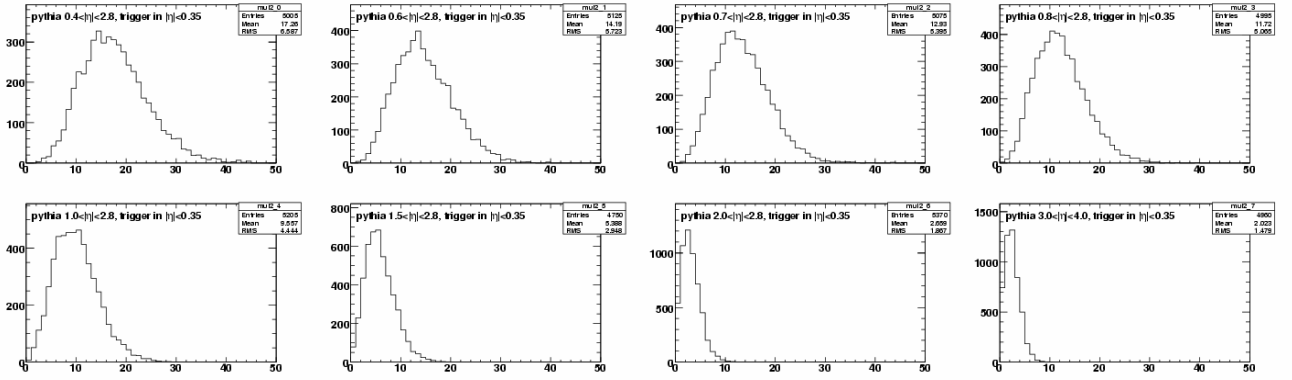
Figure 2.3.10: Rapidity dependence of the PYTHIA event charged hadron multiplicity, each event contains a dijet with a trigger hadron in mid-rapidity.
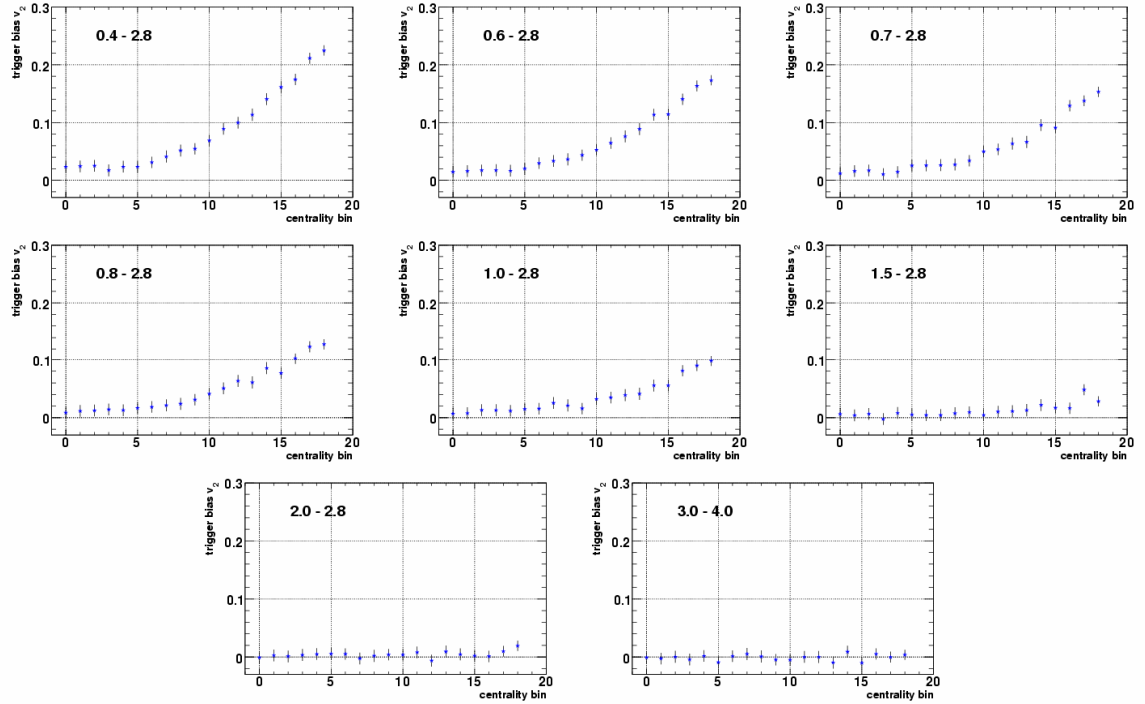
Figure 2.3.11: Centrality dependence of the raw fake v₂ for various rapidity window.

and simultaneously minimize the fake v_2. One reasonable choice is $1.0 < |\eta| < 2.8$. For this bin, the RP resolution is still pretty high (~0:72), the fake v_2 is not so big (~2-4%) in 20-30% centrality bin. The fake v_2 only becomes big for the peripheral bin (50-60%). To correct for the small fake v_2 in peripheral bin, we propose to subdivide the η into two windows: 1.0-1.5, and 1.5-2.8. The first window has some bias effect while the second η window has very small bias effect. For some analysis such as J/Ψ v_2 or v_2 at low p_T, both window can be used. For high p_T analysis which is affected by the auto-correlation, one have to develop a procedure to correct the bias effect in the first window before combining the second one.
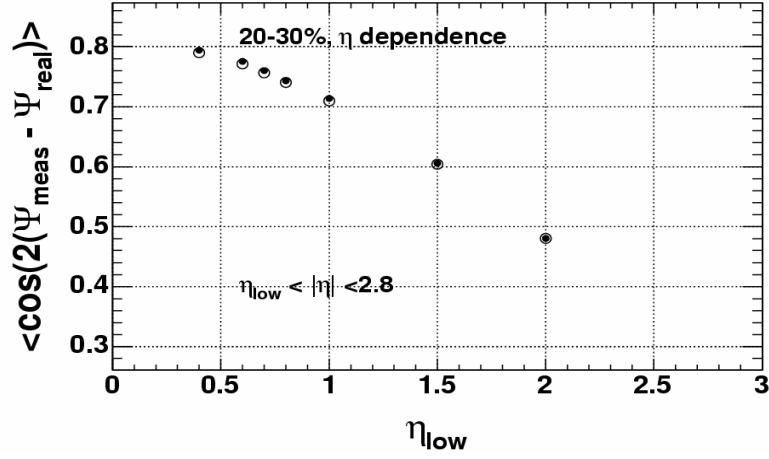
Figure 2.3.12: The RP resolution for various rapidity window (as function η_{low} , where $\eta_{low} < |\eta| < 2.8$.
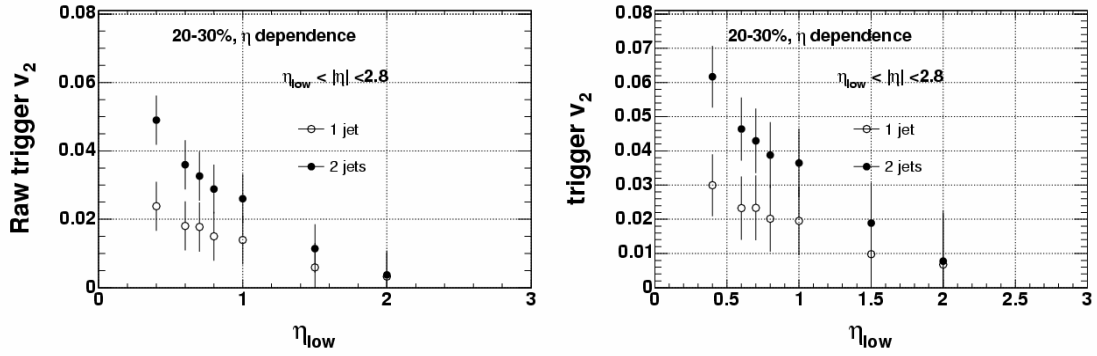
Figure 2.3.13: The fake v_2 for 20-30% centrality for various rapidity window. a) raw fake v_2, b) corrected for RP resolution. The open symbol represents the normal jet multiplicity and the filled symbol represents the jet with twice multiplicity.
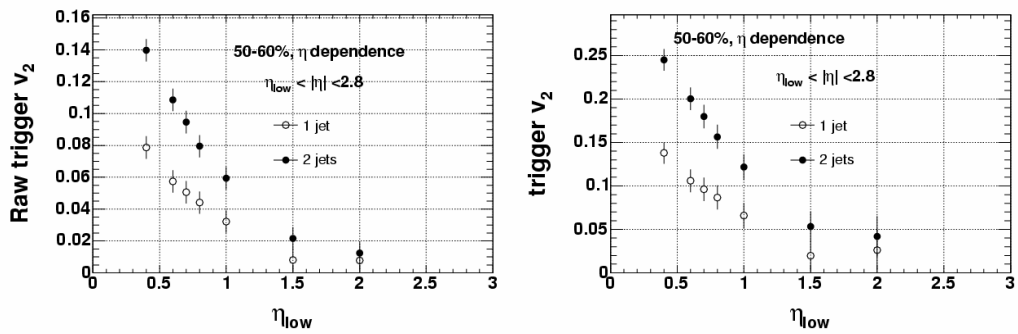
Figure 2.3.14: The fake v_2 for 50-60% centrality for various rapidity window. a) raw fake v_2, b) corrected for RP resolution. The open symbol represents the normal jet multiplicity and the filled symbol represents the jet with twice multiplicity.

2.3.5 Comparison with results using full PISA simulation

In full PISA simulation of the RXP detector, not only charged hadrons but also pi0s will contributes to improving the RP resolution (via convertors). Fig.2.3.15 shows the fake v_2 for using only primary charged tracks that hit the RXP detector in $1.0 < |\eta| < 2.8$ in the left panel and the fake v_2 for using all hits in the RXP detector in the same rapidity window. This can be compared with Fig.2.3.8 where only primary charged particles were used in the ideal case (no decay no stopping by detectors etc). We can see, the fake v_2 in all three cases are very similar which is probably due to the factor the relative contribution from the PYTHIA event is the same with or without the full simulation. On other hand one can see the RP resolution for using only primary hits and all hits differs by about 20%. That means the contribution from secondary particles from convertor are very important for improving the RP resolution.
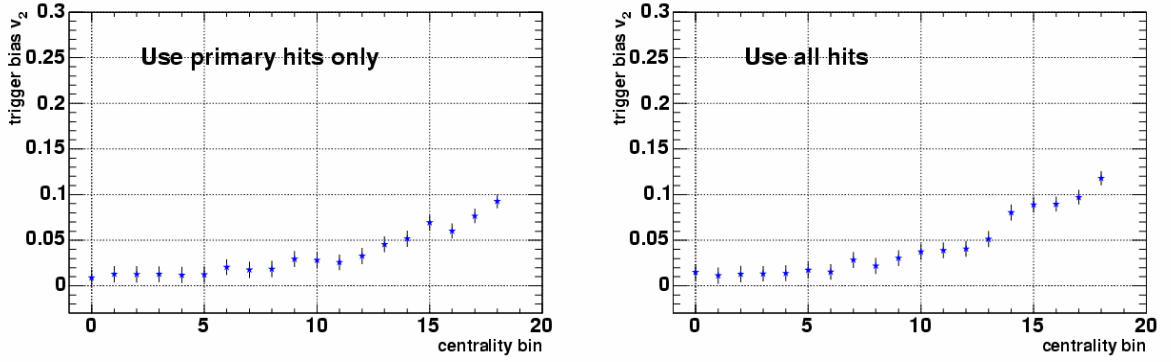
Figure 2.3.15: Centrality dependence of fake v_2 for $1:0 < j´j < 2:8$ with full PISA simulation for a) using only primary hits, and b) using all hits.
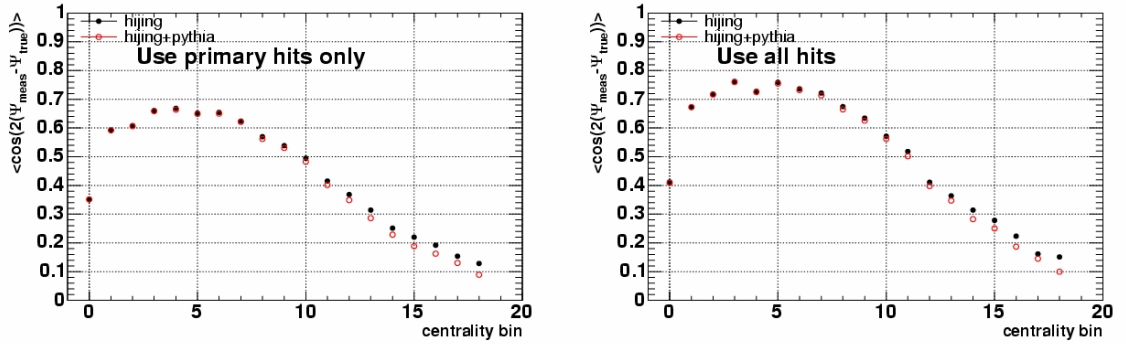
Figure 2.3.16: Centrality dependence of RP resolution for $1.0 < |\eta| < 2.8$ with full PISA simulation for a) using only primary hits, and b) using all hits.

2.3.6 pT dependences

Fig.2.3.17 shows rapidity and transverse momentum distributions of charged hadrons in
pythia p+p at 200GeV. The black point is with no bias and red/blue data are with bias of
high pt trigger in the central arm acceptance for near/away side regions, respectively.

Figure.2.3.17 : rapidity and pT distribution in pythia p+p at 200GeV, colored data are biased samples with
high pT track trigger in central arm acceptance.
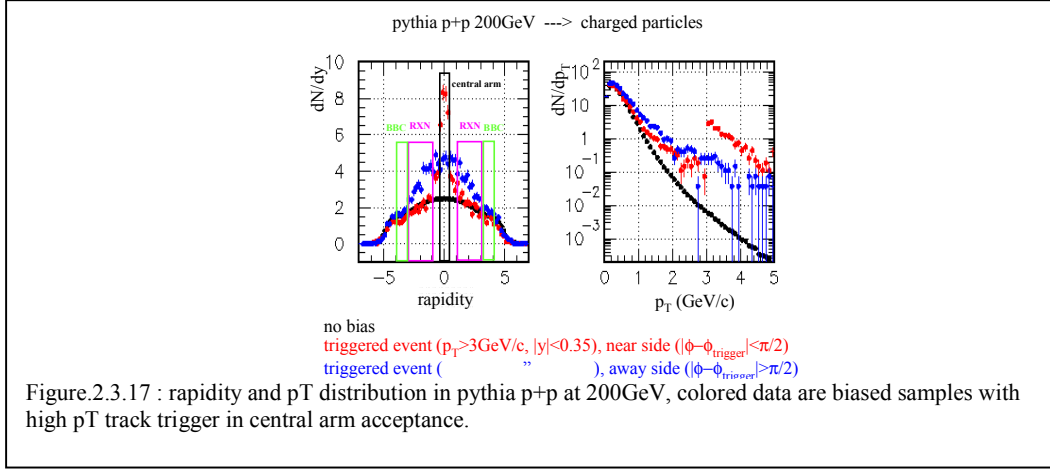
Fig.2.3.18 shows jet yield (top-middle) and jet v2 (bottom) assumption used in the
following simulation, jet events are taken from the pythia event with high trigger in the
central arm. Three different jet yields are tested from the left to right panels, v2 and v4
for the thermal flow particles are generated according to the measured pT and rapidity
dependence of v2 and multiplicity. The simulation was done with or without v2 of jet as
shown in the bottom panels.

Figure.2.3.18 : different jet yield and jet v2 assumptions with respect to the thermal flow particle

Figure.2.3.19 : simulation with mid-central 20-40% case and jet yield #2 case, the jet v2 is varied from top to bottom panels. The left panels show raw v2 with calculated reaction plane from BBC (red) or RXN (blue) compared with true reaction plane (black). The both middle and right panels show the corrected v2, where the middle panels are corrected with true resolution, while the right panels are corrected with estimated resolution via sub-event method (north – south correlation).

Comparison between middle and right panels in Fig.2.3.19 (where there is no visible difference between middle and right panels in case with jet) shows that the resolution estimation works with sub-event methods via north and south correlation. No jet case should give no difference between middle and right panels by definition, if there is no additional correlation between north and south rather than the flow. This can be explained by the large enough rapidity gap between north and south arms of the new rxn detector, so that the jet correlation (unmodified from p+p) between north and south is small. However we do see small difference between mid-rapidity v2 measured with RXN (blue) and one measured with BBC (red) for a large jet v2, this tells us that there is a small effect of jet-like auto-correlation between the new RXN detector and central arm charged particle. This is summarized in the Fig.2.3.20, where the jet yield is varied from the left to the right panels and jet v2 is varied from the top to the bottom panels. The Fig.2.3.20 shows that v2 measured by the new RXN reaction plane (blue) is systematically larger than one measured by BBC reaction plane (red), because of the stronger jet auto-correlation in the new RXN detector (smaller rapidity gap) compared to the one in the BBC, and this effect seems to be larger for large jet yield as well as for the large jet v2.

mid-central
(20-40%)

jet yield #1   jet yield #2   jet yield #3

black : true v2

blue : measured v2
       w.r.t. RXN R.P.

red : measured v2
      w.r.t. BBC R.P.

jet v2=0

jet v2=0.13

The jet effect on
RP angle is small,
because of the
high multiplicity

jet v2=0.26

Figure.2.3.20 : Comparison between v2 measured with the new RXN detector (blue) and v2 measured with the BBC (red). Slight difference between blue (v2 w.r.t. RXN) and red (v2 w.r.t. BBC) is seen, where red (v2 w.r.t. BBC) follows the black (true v2), which shows the a small effect on the auto-correlation between central arm and the new RXN detector.

peripheral
(60-90%)

jet yield #1   jet yield #2   jet yield #3

black : true v2

blue : measured v2
       w.r.t. RXN R.P.

red : measured v2
      w.r.t. BBC R.P.

jet v2=0

jet v2=0.13

The jet effect on RP
angle is significant in
peripheral events,
even with the same
relative jet yield w.r.t.
flow particles as in
the previous page.

jet v2=0.26

Figure.2.3.21 : The same comparison as the previous figure with peripheral case. The effect of auto-correlation is much stronger for the peripheral case, because of the small multiplicity.

As shown in the Fig.2.3.21, the effect is stronger for the peripheral events, even with the same relative jet yield and jet v2 compared with the thermal flow particles.

2.4 Optimization of detector parameters

Fig.2.4.1 shows the azimuthal segmentation dependence of reaction plane resolution for various cases, where the left panel shows comparison between scintillator and cherenkov radiator including one dead slat cases, and the right panel includes the 2, 3 dead slat cases, several dash/dot lines are with several different relative orientation of two dead slats. The effect becomes smaller with more than 12 azimuthal segmentations, therefore we aim for the 12 segments detector for our default option.

Figure.2.4.1 : reaction plane resolution as a function of azimuthal segmentation for various cases.

Figure.2.4.2 : reaction plane resolution as a function of radial position on the RXN detector.
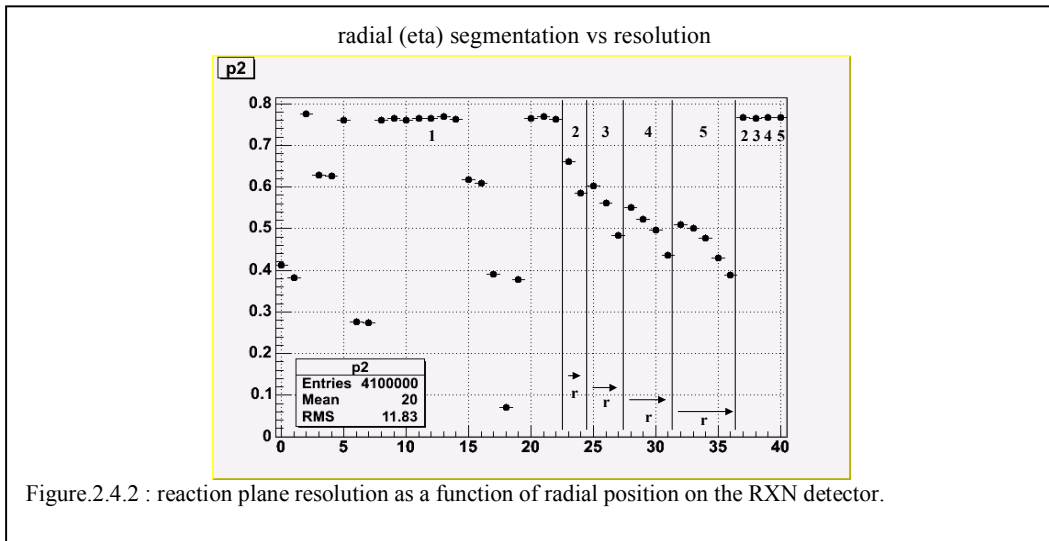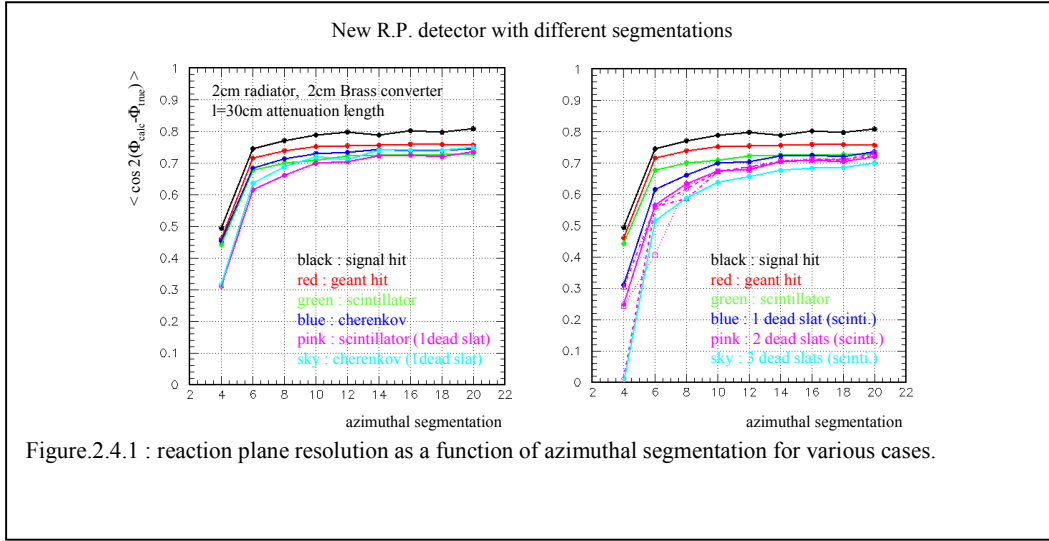
In Fig.2.4.2, the 4 regions (2/3/4/5) indicate the number of radial segmentation for the RXN detector. The resolution for each radial segment for each segmentation case is shown in each region. The combined reaction plane resolutions are shown at the most right 4 points for each segmentation case, it does not help to improve the resolution with finer radial segment, but it could be because that there is a kind of radial position weighting already/automatically given by the attenuation effect. The main purpose to have radial segmentation is to give a possibility to study auto-correlation and remove by measuring the rapidity gap dependence of v2 measurements. Fig.2.4.3 and Fig.2.4.4 show the correlation between the number of geant hit per segment and the amplitude (dE/dx) per segment for several different Brass converter thicknesses (Fig.2.4.3) with fixed scintillator thickness 2cm and for several different converter materials (Fig.2.4.4) with sandwich type detector configuration.

Figure.2.4.3 : Brass converter thickness dependence with fixed scintillator thickness 2cm for reaction plane resolution and correlation between geant hit and amplitude per segment

Figure.2.4.4 : converter material (Brass, Lead and Tungsten) dependence with sandwich type detector configuration for correlation between geant hit and amplitude per segment
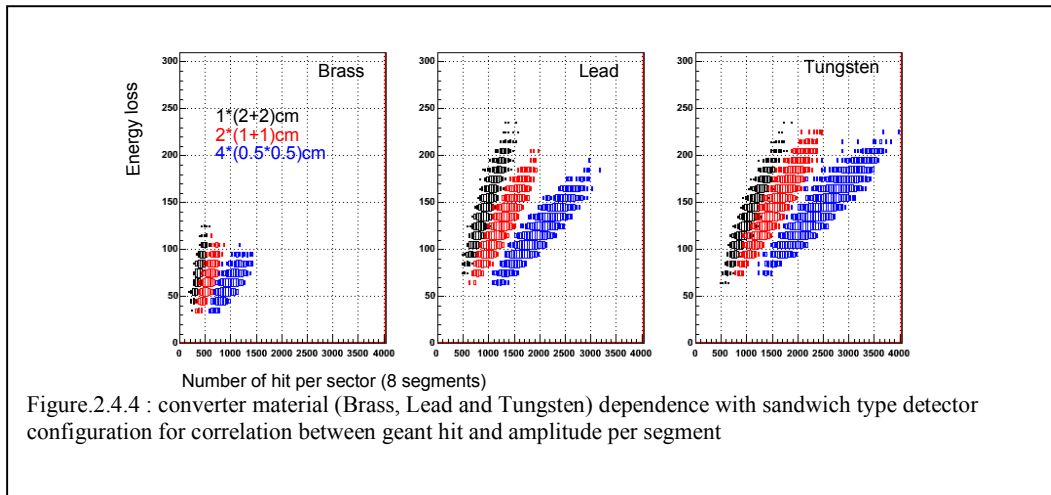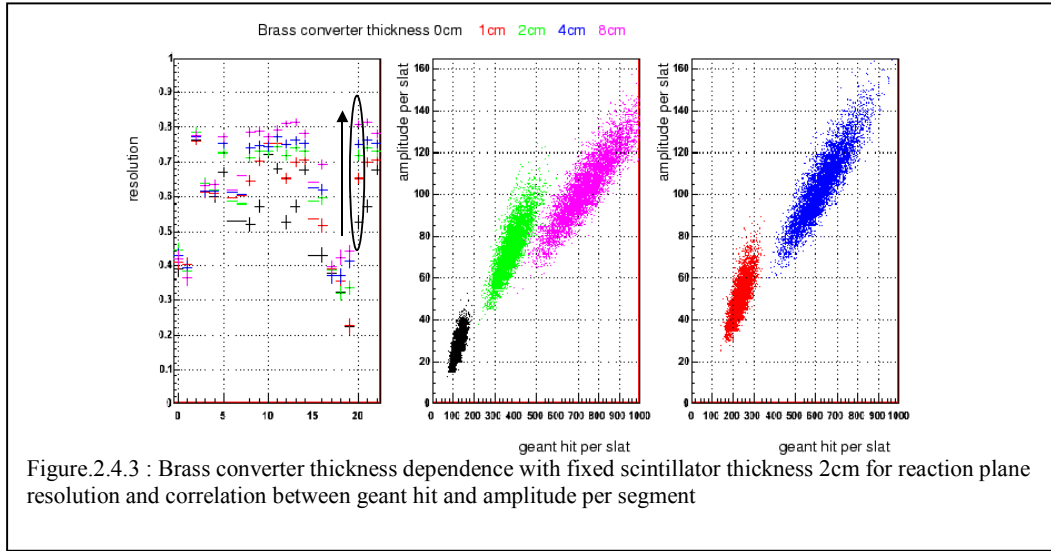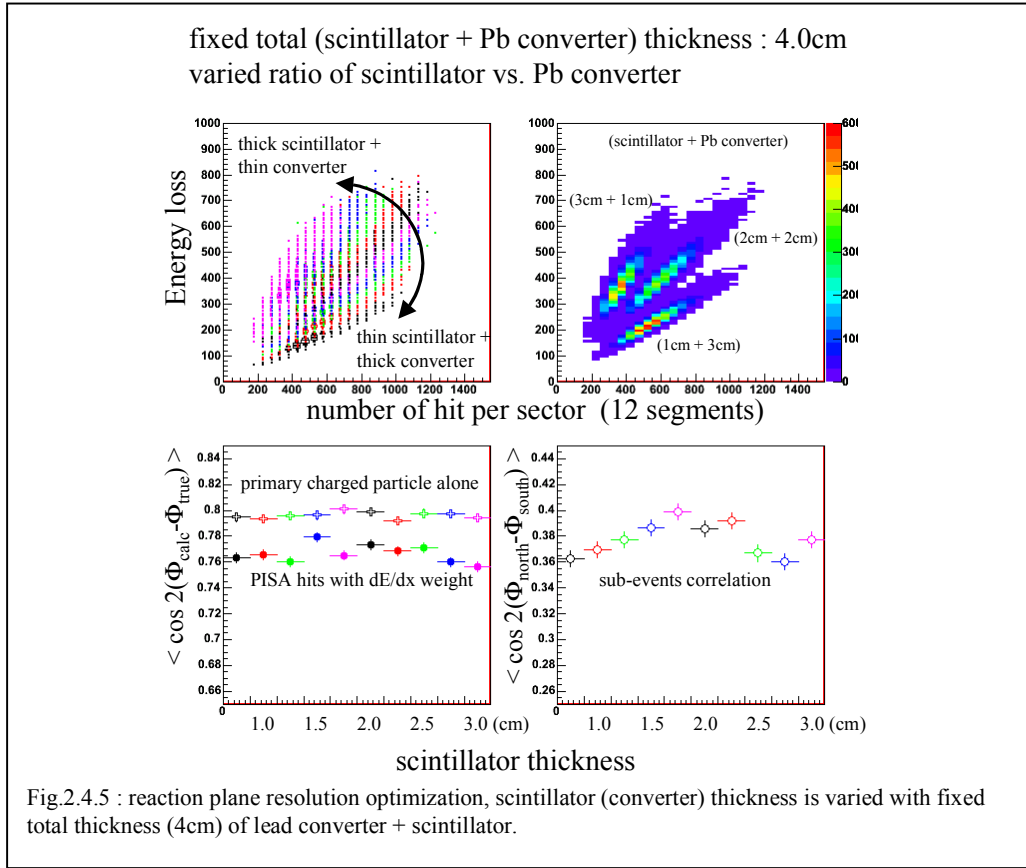
The Table.2.4.1 and Table.2.4.2 show the results of reaction plane resolution for the previous 2 figures for several different Lead or Brass converter thicknesses (Table.2.4.1) with fixed scintillator thickness 2cm and for several different converter (Brass, Lead and Tungsten) materials (Table.2.4.2) with sandwich type detector configuration. The resolution increases with increasing the thickness up to 8cm with Brass converter, while the resolution has a maximum at about 2-4cm with Lead converter. The resolution at the same 2cm thickness is better with Lead converter than with Brass converter. Since the available space of the detector is about 4cm in total including the both converter radiator, the conversion with Brass is not enough and we'll be able to optimize the performance with Lead converter. Although it seems that the sandwich type is slightly better as shown in Table.2.4.2, a simpler configuration for the RXN detector with 2cm Lead converter and 2cm scintillator was chosen for the final design.

Scintillator thickness (cm)	2	2	2	2	2
Conveter thickness (cm)	0	1	2	4	8
Resolution (Br)	0.53	0.65	0.71	0.76	0.80
Resolution (Pb)	0.53	0.73	0.75	0.75	0.68

Table.2.4.1 : reaction plane resolution for different converter thickness (Brass and Lead) with fixed scintillator thickness (2cm).

Scintillator (n*x cm)	1*2	2*1	4*0.5
Converter (n*x cm)	1*2	2*1	4*0.5
Resolution (Br)	0.70	0.71	0.67
Resolution (Pb)	0.74	0.78	0.78
Resolution (W)	0.76	0.79	0.79

Table.2.4.2 : reaction plane resolution for different converter (Brass, Lead and Tungsten) materials with sandwich type detector configuration

fixed total (scintillator + Pb converter) thickness : 4.0cm
varied ratio of scintillator vs. Pb converter

Fig.2.4.5 : reaction plane resolution optimization, scintillator (converter) thickness is varied with fixed total thickness (4cm) of lead converter + scintillator.

The Fig.2.4.5 shows a reaction plane optimization to find a best choice of scintillator (Lead converter) thickness for a fixed total thickness of 4cm. The top panels show correlation between the number of geant hit per segment and the amplitude (dE/dx) per segment for different choices. The thicker scintillator gives larger amplitude per particle and the thicker converter gives more conversions, which increase the number of particles, however if it's too thick they get absorbed. The optimum seems to be about 2+2cm case.

3. Design of the Reaction Plane Detector

3.1 Light Readout device

The light readout device needs to be insensitive to the strong magnet field and also have good dynamic range and signal-to-noise ratio. There are two possible options available: Avalanche photodiode (APD) and fine mesh PMT. The Hamamatsu fine mesh dynode photomultiplier is designed to operate in strong magnet field over 1.0 Tesla. The model R5924 has been used in various efforts in PHENIX to build detectors in the area near the nosecone where the magnetic field is close to 1.0 Tesla. Avalanche photodiode (APD) is high speed photodiode with high sensitivity achieving an internal gain via applying a reverse HV. Because of its small size, it can be directly attached to the scintillator without the necessity of using light guides. This can significantly simplify the detector design compared to using PMTs. It's also not sensitive to the strong magnet fields and much cheaper ($75 including the charge sensitive amplifier) than the fine-mesh PMT ($4k). The only concerns are the signal/noise ratio and dynamic range. If both can fulfill our needs, APD would be a much be an ideal choice for the reaction plane detector.

3.1.1 Option on APD or PMT

In this section, we calculated the signal-to-noise ratio for the APD (S8664-55) adopted by PHENIX MPC (see fig.3.1.1). The APD has 5x5mm active area with one side directly attached to a charge sensitive amplifier (CSP). The signal is further amplified before entering FEE. Since the whole readout chain is available, we did the calculation and cosmic-ray test on the signal/noise ratio assuming the same setup will be used for the reaction plane detector.
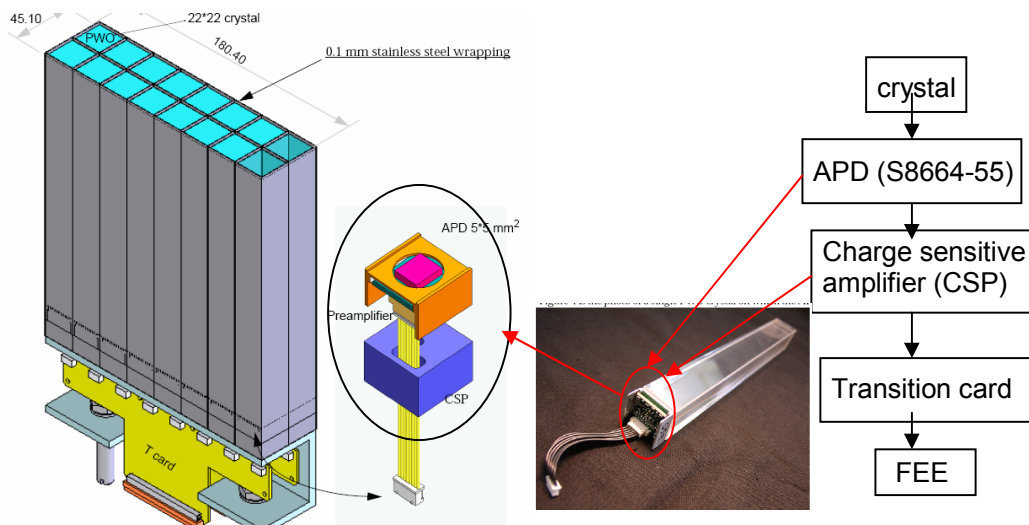

Figure 3.1.1 APD application in CMS/PHOS experiment

We expect the detector to cover collisions in a wide range of centralities and require the signal/noise ratio of 1 MIP signal high since in very peripheral collisions, the number of hits per channel is about one. The following parameters of the APD are used for the calculation

- active area: 5mmx5mm
- Q.E.~70%@ ~400nm. 40%@~300nm
- gain 100@350V@20 degree C. PHOS/MPC use gain=50.
- noise (APD+CSP): 500 e for 1 micro-second integration time and 1500 e for 100ns integration time (from Terry, Mickey).

Since the dE/dx from a MIP in plastic scintillator is about 2MeV/cm, the energy loss in the 2cm scintillator is 4MeV/MIP. About 3% of the lost energy is converted into light. This means one MIP will inspire 40000 photons. With 1MeV=1.6e-5 Watt, 1MIP deposit 6.4e-5watt*3.0%=1.92e-6w into the detector. The photon Sensitivity (PS) for APD and fine mesh PMT (R5924) are calculated as the following

- Q.E. = PS*1240/lamda
- Q.E. (APD)=70%@400nm, i.e. PS(APD)=0.21A/w
- Q.E. (R5924 fine mesh tube)=22%@400nm, i.e. PS(R5924)=0.07A/w

The signal observed from R5924 PMT per MIP particle is

I = rdf * E_depo*PS = rdf * 1.92e-6w*0.07A/w=rdf*1.34e-7A,

, where *I* is the current and *rdf is the reduction factor* including PMT acceptance and light attenuation. With the R5924's gain at HV=1200 of about ~2e5, the voltage output is V=I*50ohms*gain=rdf * 6.7e-6 V*2e5= rdf * 1.34V. The observed PMT pulse height is ~80mV@1200V and it leads to rdf(R5924)= 0.06. The APD rdf is deduced assuming rdf (APD) / rdf (R5924) is proportional to the ratio of their active area, i.e. area(APD)/area(R5924) =25mm^2/1963mm^2, therefore the rdf(APD) = 25/1963 *0.06 = 7.6e-4. The signal from APD is rdf * N_photon * Q.E. * APD_Gain = 7.6e-4 * 4e4 * 70% * APD_Gain, i.e. 1063 photo-electrons per MIP for the gain of 50. The output voltage from CSP is V_out = APD_charge/C_f ~0.14mV/MIP, where C_f is the CSP feedback capacitance (~1.2pf). The noise of APD+CSP noise based on the PHOS R&D results is ~500e to 1500e depending on the integration time. This means the Signal/Noise ~ 1-2 for per MIP for us and this is too low.
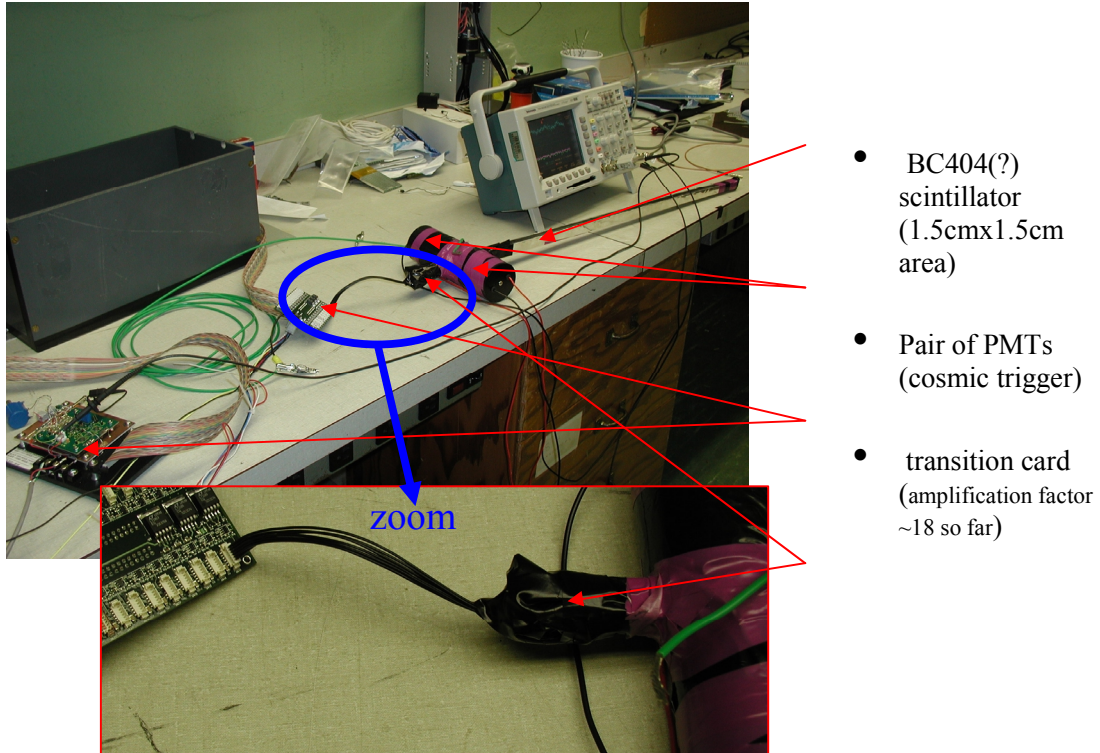
Figure 3.1.2 test setup for testing APD signal from cosmic-ray

We did the cosmic-ray test to confirm the calculation. The same electronic readout chain for the MPC is used for the test (see fig.3.1.2). Two PMTs are attached to a stick of BC404 on opposite side to serve as the cosmic-ray trigger. The APD is attached to on end of the stick. The gain of APD and transition card are adjusted to 50 and 18, respectively. CSP provide a factor of ~2 more amplification. The noise is ~10mV as shown in fig.3.1.3 and is very close to the optimized value observed during the MPC test. In most cases, signal is submerged into the noise. In rare cases, we could see clear signal due to the landau fluctuation. This shows the signal/noise ratio is <=1.0 and is in rough agreement with the calculation. The conclusion is we will use fine mesh PMT for the light readout.
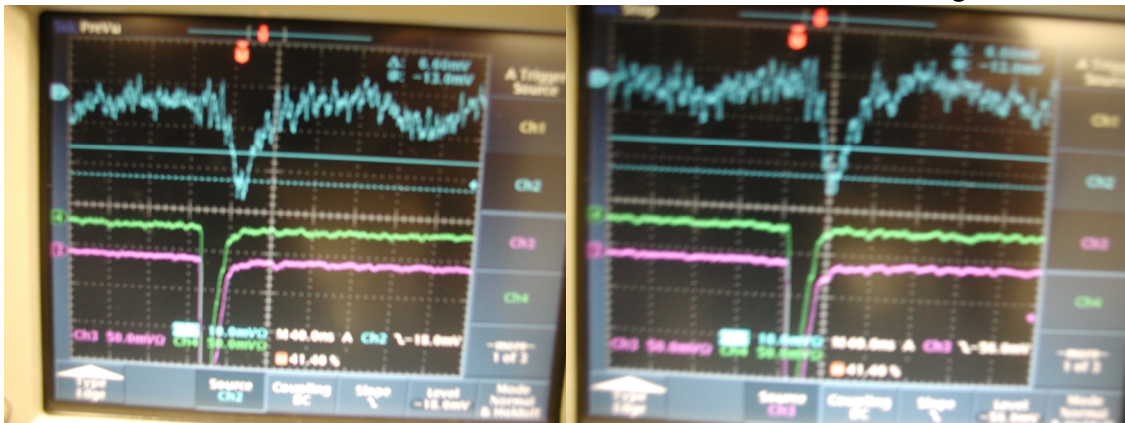

Figure 3.1.3   observed cosmic-ray signals

3.1.2 PMT Performance in magnet field

The performance of the fine mesh dynode photomultiplier is known to be sensitive to the angle between the tube axis and magnetic field line. It is very important to fully understand the tube response at different angles in order to constrain or simplify the detector design. The company provided the results for only 30 and 0 degrees. We did a test to check tube gain and MIP peak resolution under different angles and field strength using the calibration magnet in the BNL magnet division.

The source of signal comes from a LED. Figure 3.1.4 shows the test stand holding the tube and the aluminum box containing the LED with an optical fiber connection in between. A small piece of glass plate is glued at one end of the fiber serving as the interface between the tube window and the fiber to avoid variation of light input during the test. A U-shape plastic piece bound with the tube is glued to the wood support at the required angle. Figure 3.1.5 shows the experimental setup for the test. The aperture of the dipole magnet controlled by a computer is about $50 \times 20 \times 300 cm^3$. Its maximum field strength can reach 1.2 Tesla. The up and down side correspond to the south and the north pole, respectively. The test stand is inserted deeply into the magnet to ensure uniform field around the tube. A field probe is also inserted into the magnet to about the same place where the tube stands to make sure the field surrounding the tube has the required strength. A PHENIX standard PDAQ system is setup for the data acquisition. A pulser (Agilent 33250A) is used to generate 50Hz -2V pulse with 20ns width and 5ns rise time to drive the LED. The pulse width and rise time is chosen to be similar to the MIP signal. The magnet is ramped up and down for each photo tube at a given angle between 4kG to 10kG that covers the range of field strength in the PHENIX central inner region.
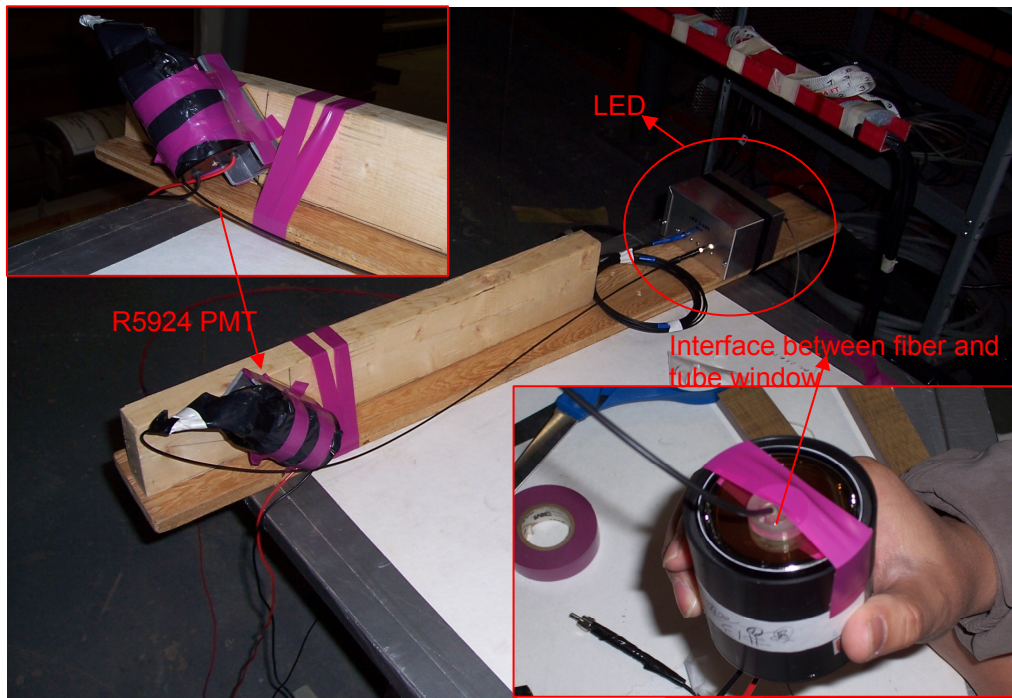
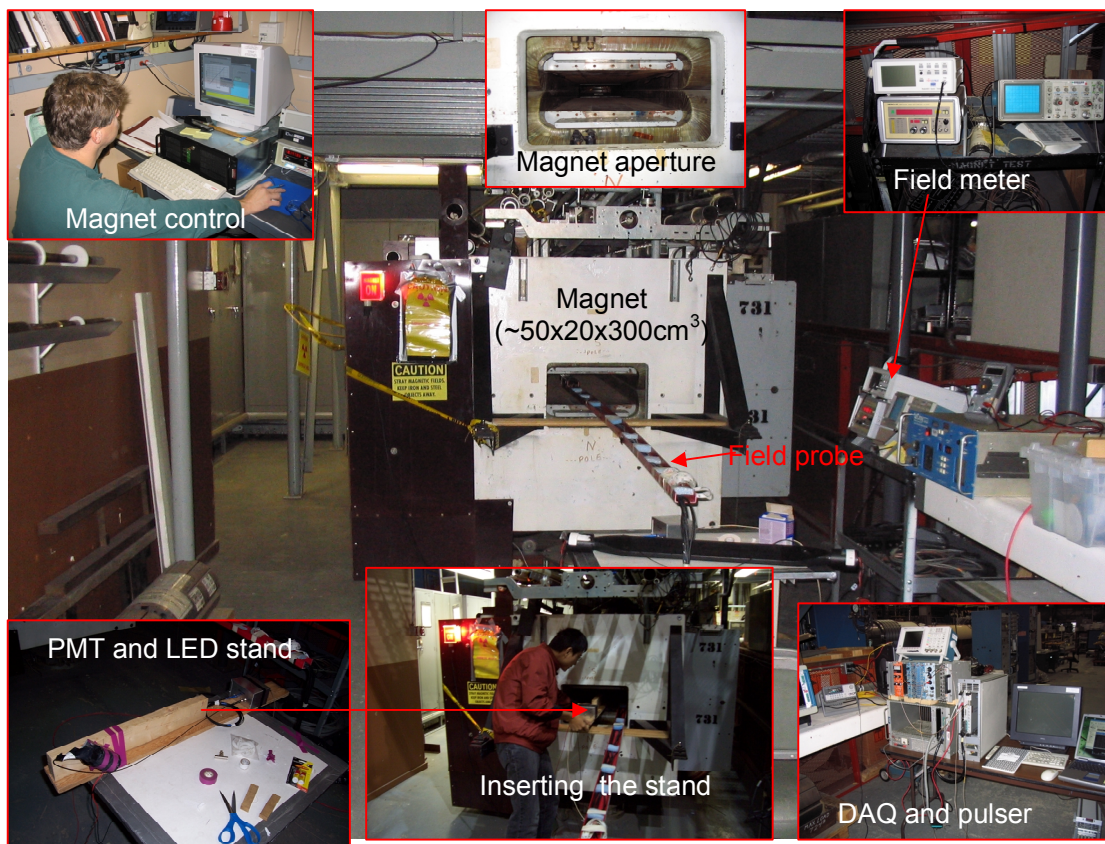Figure 3.1.4: Test stands to hold LED and tubes with fiber connection in between

Figure 3.1.5: Experimental setup diagram

Two issues are addressed in this study: the change of the gain and the change of the MIP peak resolution in different conditions. The latter is very important to the detector signal to background ratio.

The company has the results on gain variation at 0 and 30 degrees for the module R5924 and at a broader range of angle for another model but at limited field strength as shown in fig.3.1.6. There has been a misunderstanding based on the experience from regular photomultipliers that the tube performs best at 0 degree since the electrons suffer less bending force compared to those at other angles. The results for the R5924 show that the tube gain is in fact higher at 30 degree than at 0 degree up to 1.5T. The right hand plot shows the results for R5946 which is presumably similar to R5924. One can see the tube produces higher gain with larger angle below ~200G. Above 200G, the gain drops quickly to zero at 90 or 75 degree.
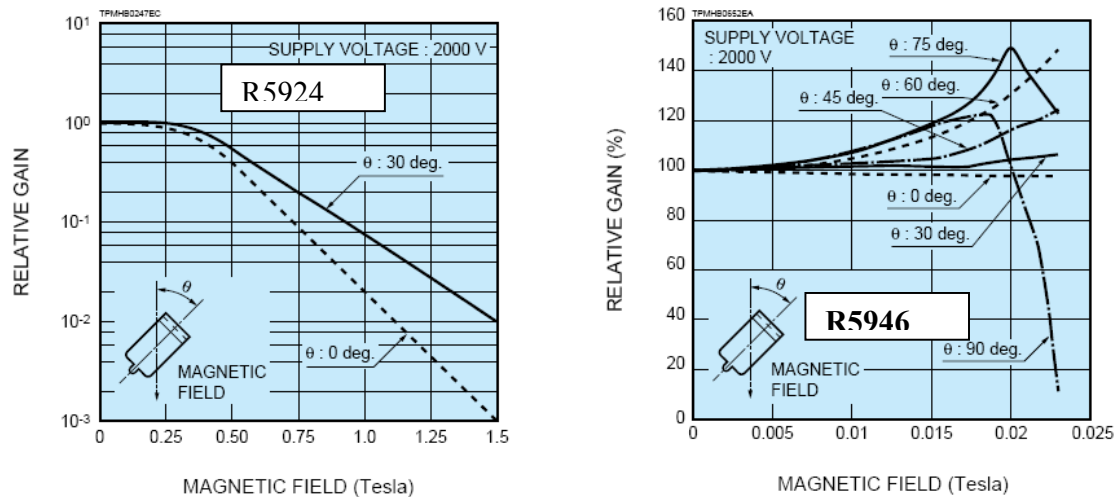
Fig.3.1.6 Hamamatsu test results on two models

It's a surprise that the performance does not dependent very much on the strength of the field component perpendicular to the tube axis. It's very likely due to the mechanical structure of the tube. Fig.3.1.7 shows our test results for the R5924 gain variation with different angles and field strength at different HV's. The ADC value is directly achieved from the DAQ when the pulse height is larger than the discriminator threshold, otherwise it's calculated assuming the ratio of ADC is equal to that of the pulse height. One can see the tube performs best at ~45 degrees up to 10kG. At 50 degree it still works but the gain is lower than that at 0 degree angle. Above 60 degree, the gain drops immediately to zero at B>100G which is similar to the company's results for another model. The gain increases exponentially with HV as expected except that the saturation starts to appear at very high gain. We tested another tube to make sure the results are repeatable.
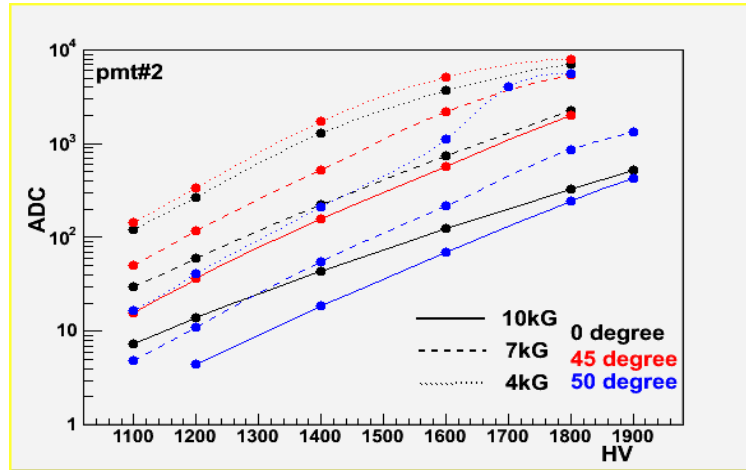
Figure 3.1.7. Tube response at different angle and field strength vs. HV

To answer the second question, i.e. the change of MIP resolution under strong field, ADC distribution is plotted in the following two cases:

- Similar gain but different angle, HV or field strength.
- Different gain but same HV and field strength.

The results are shown in fig.3.1.8. In both cases, the width/mean ratio of the distribution is quite similar and all show sharp peak. This means the MIP resolution is not affected much by the strong field. All 14 available R5924 tubes were scanned and show similar behavior.
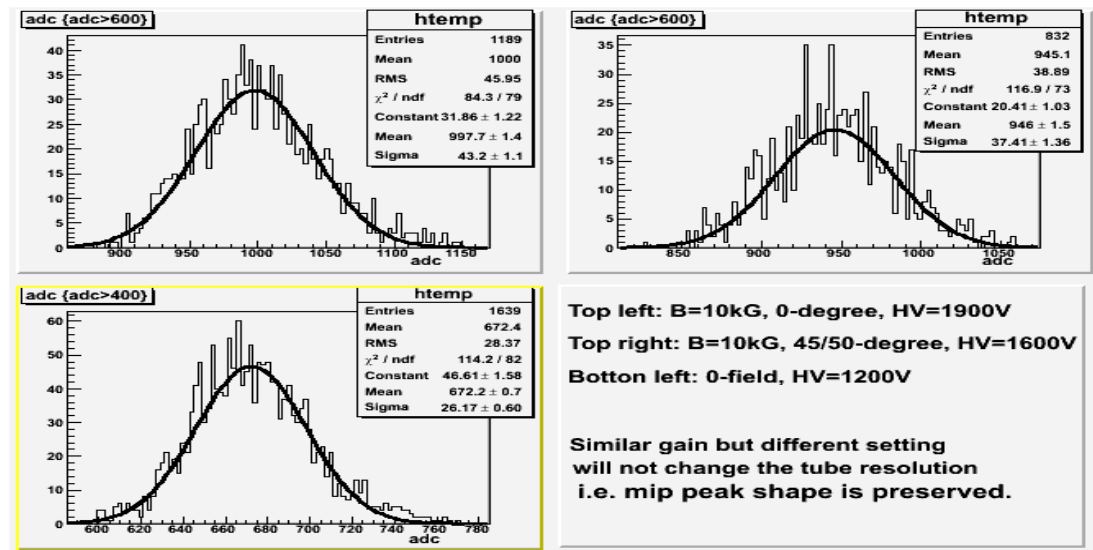
Figure 3.1.8(a). ADC distribution at different HV, field strength or HV but with similar gain.
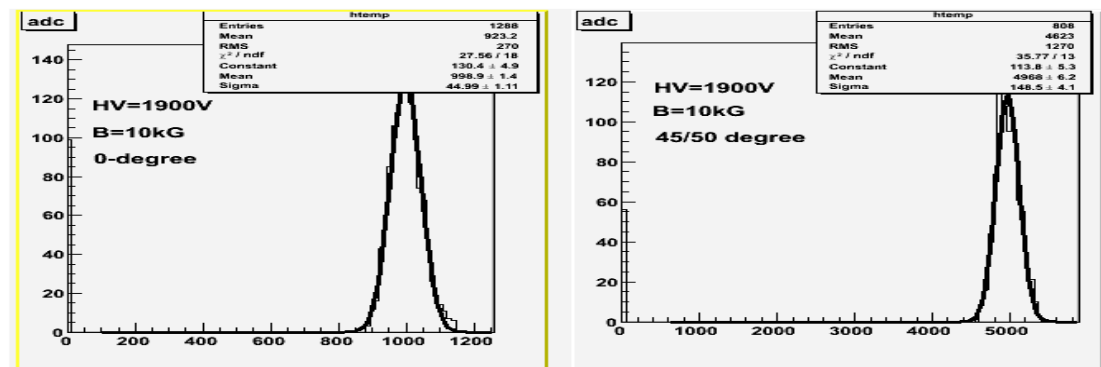

Figure 3.1.8(b). ADC distribution with the same HV and field strength but different gain

As the results show that the tube can not function inside even very weak field (100G) at an angle above 60 degree, one can map out the locations in the PHENIX inner central region that the tube can function using the standard field map assuming a certain angle between the tube axis and the beam pipe. The fig.3.1.9 shows the angle between the field lines and the tube axis versus the radial distance from the beam pipe under the ++ field assuming tube axis is parallel to the beam pipe. The angle is calculated as atan(Br/Bz)*180/3.14, where the phi component is neglected since they are small. Each sub-panel corresponds to a different slice of space along the beam direction. The left hand plot of fig.3.1.9 shows the sketch of PHENIX inner region. The blocks with different color show the region where the tube can work. The small red blocks correspond to R5924 tubes with properly scaled size.
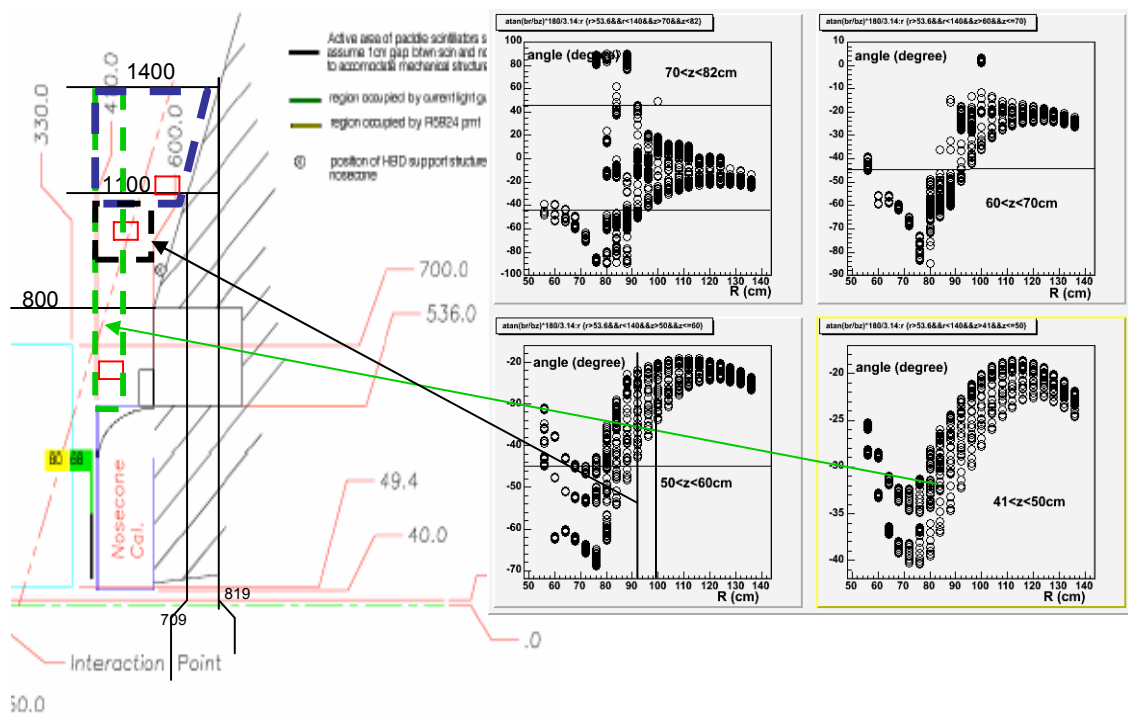
Figure 3.1.9 Angle between field line and tube axis in PHENIX central inner region assuming the tube axis is parallel to the beam pipe.

One can see the region at |Z| > 41cm is very limited and the situation can be even worse since the field map might not be very accurate close to the iron. Another test using the PHENIX magnet should be done to confirm above results. We did similar calculation to define the PMT working zone in both ++ and +- field configuration with PMT axis oriented at 0 or 30 degrees relative to the beam pipe. The results are shown in figure 3.1.10. We also did a test in PHENIX IR to confirm the results. The details is shown in next section.
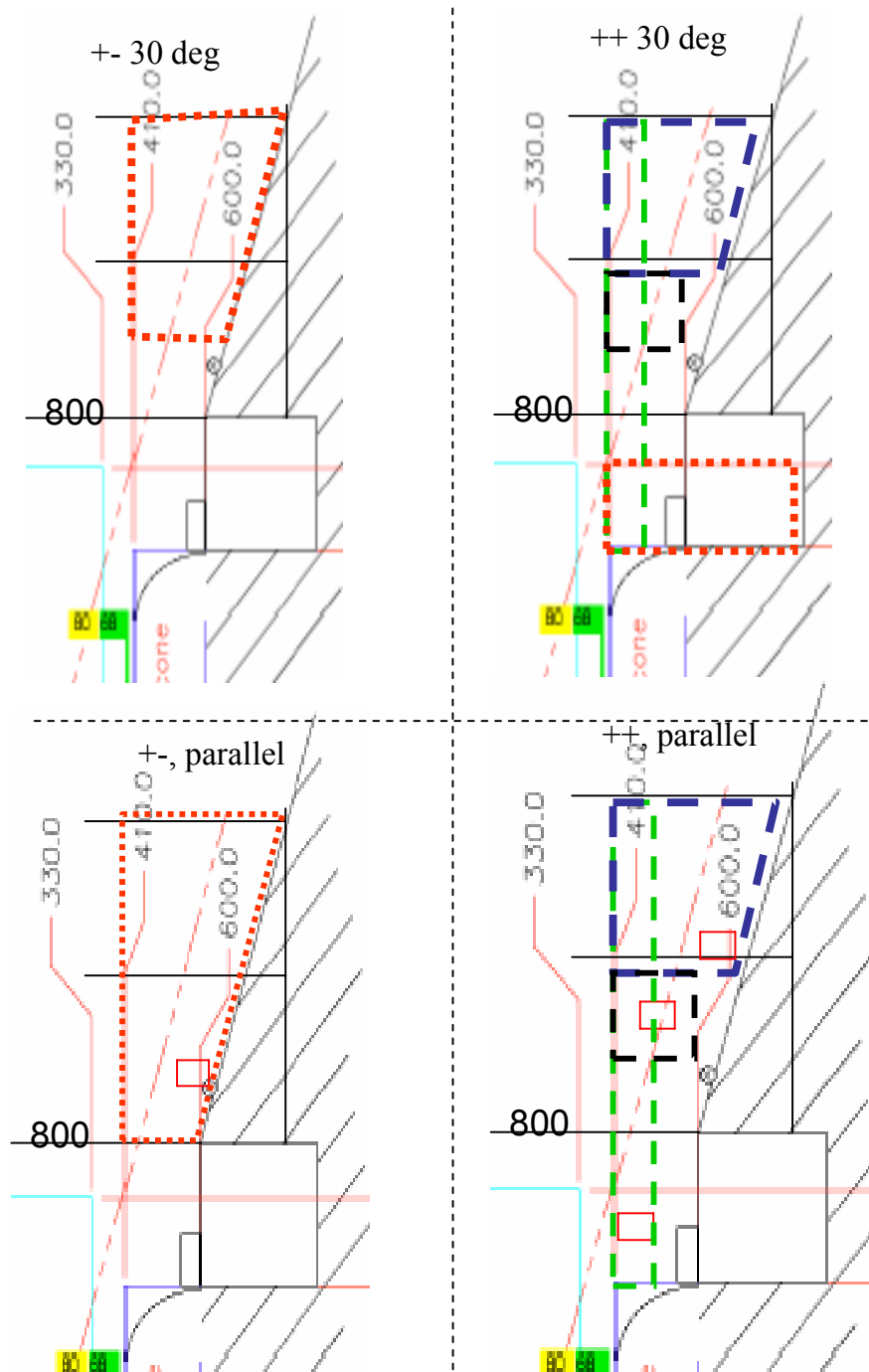
Fig.3.1.10 PMT working zone calculated from the PHENIX field map in ++ and +- field configuration.

3.1.3 Performance of PMT in the PHENIX Interaction Region

A series of tests were conducted to observe the performance of the photomultiplier tubes to be used in the reaction plane detector in the magnetic field environment of the PHENIX interaction region (IR). The calculations shown in section 3.1.2 provided guidance concerning where it was expected that the tubes would perform nominally in both the ++ and +- field configurations. A test stand was constructed to simultaneously hold 8 photomultiplier tubes, R5924. The tubes were positioned at 4 different radii (80, 90, 110, 130 cm) from the beam pipe and two different positions in phi separated by 120 degrees as shown in figure 3.1.11. A led pulser system was used to trigger the tubes and the signal was read out using an oscilloscope positioned outside of the IR. The pulse height was measured as the magnetic field was ramped to full field. Tests were conducted for two different magnetic field settings and two different photomultiplier tube orientations.
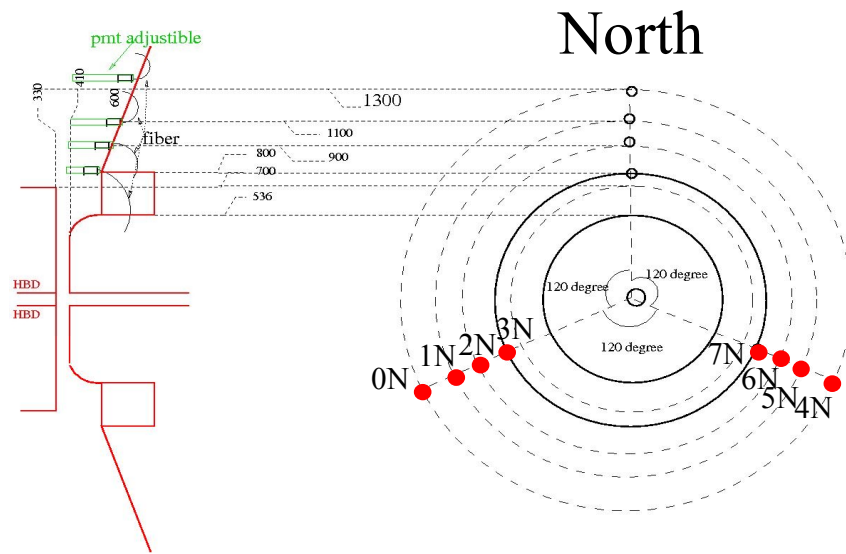

Figure 3.1.11: Side and frontal views of the North nosecone with the reaction plane detector photomultiplier tubes mounted at 4 different radial positions and two positions in phi.

In the first set of tests, the photomultiplier tubes were oriented parallel to the beam pipe with the photomultiplier tube base facing the nosecone for both magnetic field settings. At each position the gain of the tubes was measured with the magnetic field at 0%, 25%, 50%, 75% and 100% of the full field strength. The results of these tests are

shown in figures 3.1.12 and 3.1.13. The ratio of the gain of the tube at the designated magnetic field setting relative to the gain at zero field for each of the tubes is plotted versus the magnetic field strength. It can be seen that in the ++ field configuration the tube gain is only weakly affected by the magnetic field, while in the +- field configuration all of the tubes show a reduced performance at full field relative to at zero field. The pmt's placed closest to the beam pipe, R=80 cm and 90 cm, show approximately a factor of 5 reduction in gain at full field.
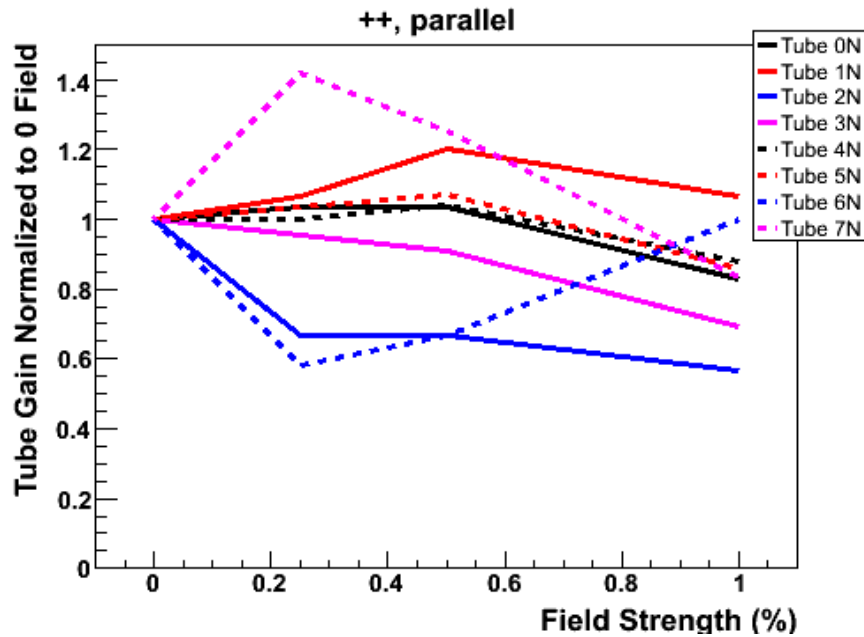

Figure 3.1.12: The ratio of the observed pmt gain relative to the value at zero field plotted versus the fraction of the magnetic field strength for the ++ field configuration with the pmt's oriented parallel to the beam pipe.

Figure 3.1.13: The ratio of the observed pmt gain relative to the value at zero field plotted versus the fraction of the magnetic field strength for the +- field configuration with the pmt's oriented parallel to the beam pipe.

In the second set of tests, the photomultiplier tubes were oriented at 30 degrees with respect to the beam pipe and with the tube base pointing towards z=0. At each position the gain of the tubes was measured with the magnetic field at 0%, 25%, 50%, 75% and 100% of the full field strength. The results of these tests are shown in figures 3.1.14 and 3.1.15. The ratio of the gain of the tube at the designated magnetic field setting relative to the gain at zero field for each of the tubes is plotted versus the magnetic field strength. It can be seen that in both the ++ and the +- field configurations the tube gain is affected by the magnetic field. In the +- field setting the pmt's placed closest to the beam pipe, R=80 cm, do not function while at each of the other radial positions the gain is reduced by at least a factor of 2.
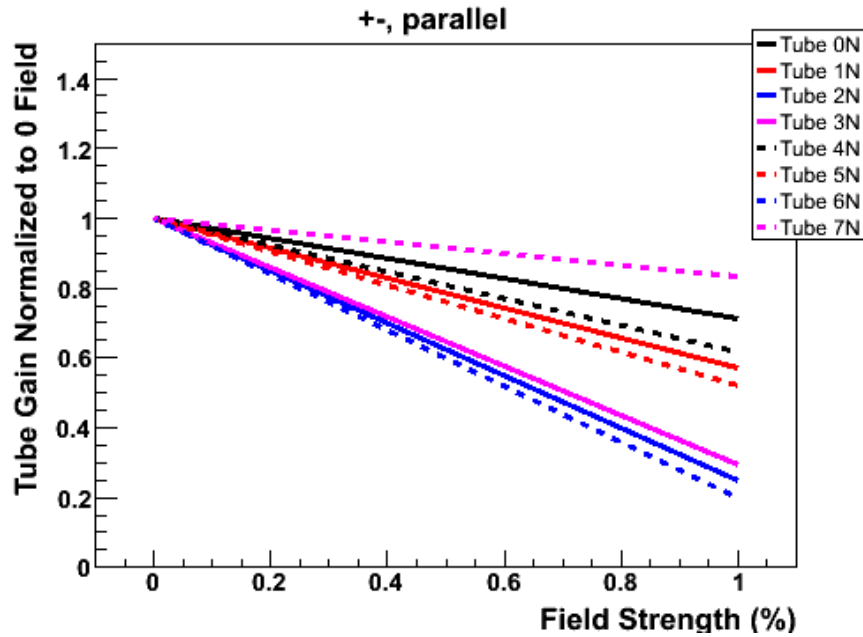
Figure 3.1.14: The ratio of the observed pmt gain relative to the value at zero field plotted versus the fraction of the magnetic field strength for the ++ field configuration with the pmt's oriented at 30 degrees with respect to the beam pipe.
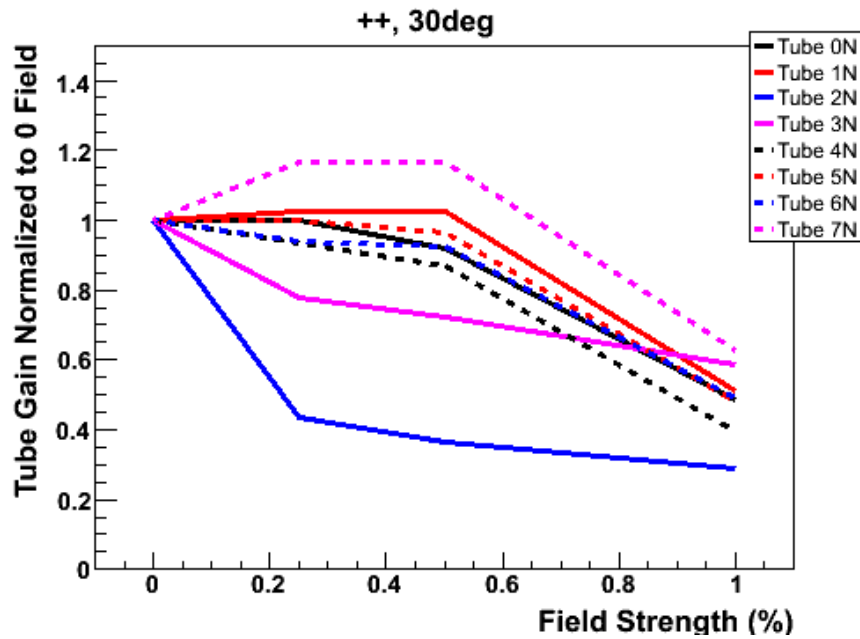

Figure 3.1.15: The ratio of the observed pmt gain relative to the value at zero field plotted versus the fraction of the magnetic field strength for the +- field configuration with the pmt's oriented at 30 degrees with respect to the beam pipe.

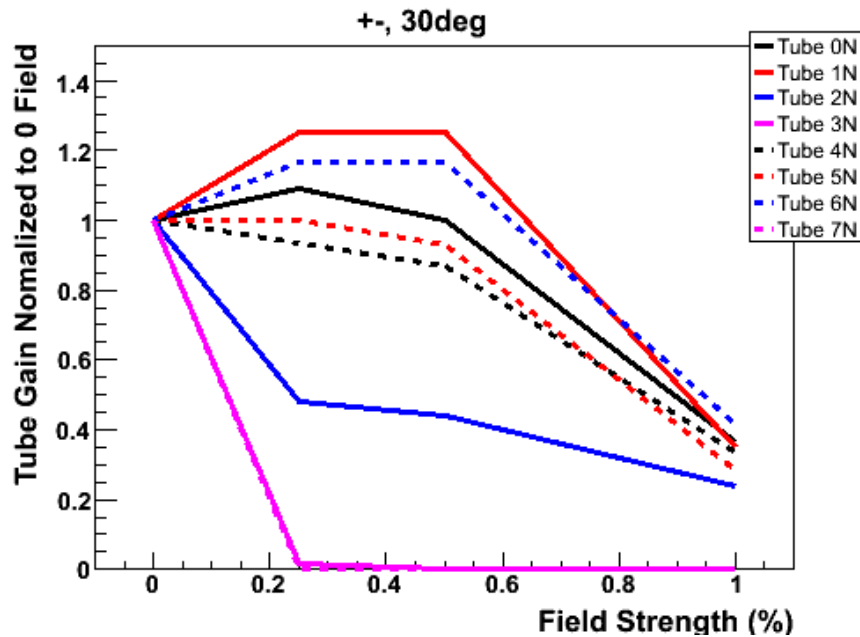The results of these tests define both the location and orientation at which the photomultiplier tubes will perform optimally. The +- field configuration provides the strictest constraints on the pmt placement. Comparison of the measured pmt gains in the

parallel and 30 degree orientations for the +- configuration shows that the pmt's should be placed at a radius greater than 90cm and that in the parallel alignment the reduction in gain is less at R>90cm than in the 30 degree alignment. For these reasons in the reaction plane detector design the photomultiplier tubes will be placed parallel to the beam pipe at a radial distance of 110 cm.

3.1.4 PMT Response linearity

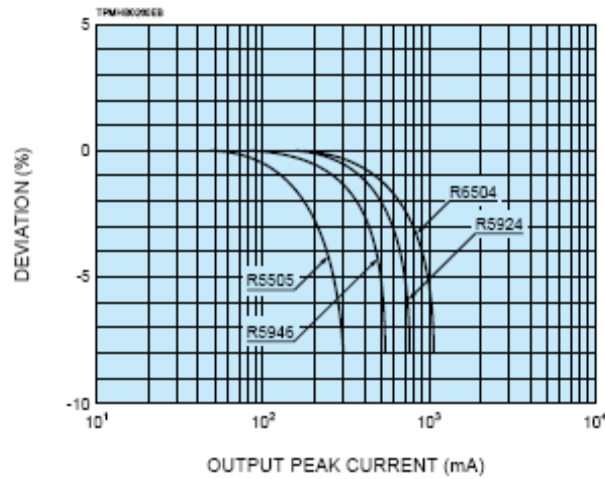The linearity of the tube can be seen in fig.3.1.16

Figure 3.1.16   PMT response linearity in pulse mode

The results show a 5% deviation from linearity of the tube response at an output pulse peak current of 700mA for R5924 and the deviation increases sharply after that. Assuming the PMTs is finally adjusted to 50mV, i.e. 1mA per MIP, each tube can receive about 700 MIP hits and still perform linearly within 5%. The results from HIJING simulation show that the number of hits seen by the detector is about 4000 per arm in 0-5% central Au+Au collisions, this means the PMTs will perform linearly is the number of channel per arm is above 8. However, there is the concern that the present condition in PHENIX might go beyond the PMT's DC linearity range. We did the estimation to check this possibility.
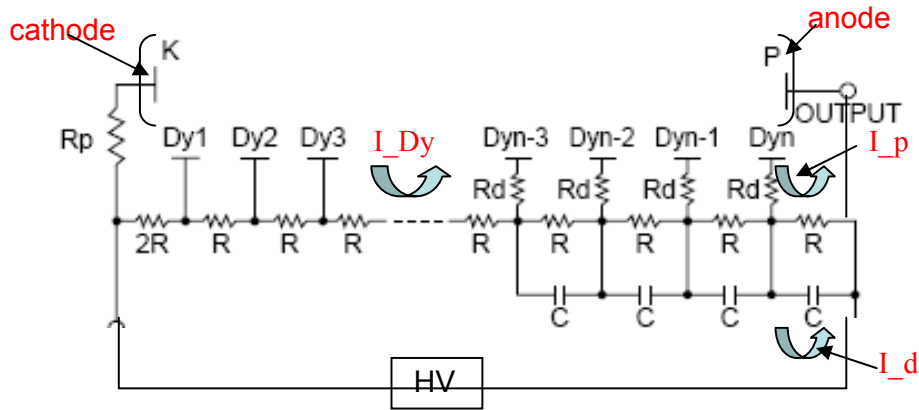
Figure 3.1.17 diagram of PMT HV divider,

Fig.3.1.17 shows the diagram of PMT HV divider where I_p is anode current, I_d is HV divider currents. In DC mode, I_p has opposite direction to I_d. When I_p increases, ΔV for each stage drops and leads to the reduction of gain, i.e. non-linearity appears. I_p is usually required to be 2-5% of I_d for good linearity. In pulse mode, if the duty cycle is small, as in our case, the I_d and I_p is decoupled by the capacitance. The linearity can reach the space charge limit. We are in pulse mode, but connect to the DC mode because of the capacitance decoupling effect.

The projected average run7 Au+Au rate is about 5kHz . The total number of charged particle in 0-5% central collision is ~8000. Since the multiplicity is roughly proportional to N_part, the detector see ~2700 in Minbias events. Assuming 20 channels for the detector, each channel collect 2700/20 = ~140 charged particles. Assuming we set PMT to 1mV per MIP output which corresponds to about 10mV signal output per photon, we have 1mV/50ohm = 0.02mA/MIP, or 0.02mA*140 = 2.8mA per Minbias collision. Each pulse is ~20ns wide, i.e. charge=2.8mA*20ns = 56pc. In most central collision, each pulse will be about 4*56pc=224pc. Taking into account the possible fluctuation of a factor of 2, each pulse is about 2x224pc = 450pc. For H6614-70 assembly, resistor for each stage is 330kohm, capacitance: 0.01uF. The RC is 330kohm*0.01uF =3.3e-3 seconds. Since it takes about 5*RC to reach 1% of V_0, we have 3.3e-3*5 ~0.02s for the pulse to die out. For each collision, I_p ~ 2.8mA*20ns/0.02s = 2.8e-9 A. During the 0.02s, we have 0.02s/(1/5kHz) = 100 collisions, therefore the total currents is about 2.8e-9A*100 collisions ~0.28uA. This need to be 2-5% of the I_d, i.e. I_d should be 6-14uA. The divider currents for most of the assembly is ~400uA at 2.5kV. To achieve 1mV per mip signal, HV need to be set at ~800V, i.e. the divider current is about 400uA*2500/800 ~130uA which is much higher than the current limit for good linearity.

3.2 Radiator and light guide

Figure.3.2.1 : beam test setup at KEK-PS T1 beam line
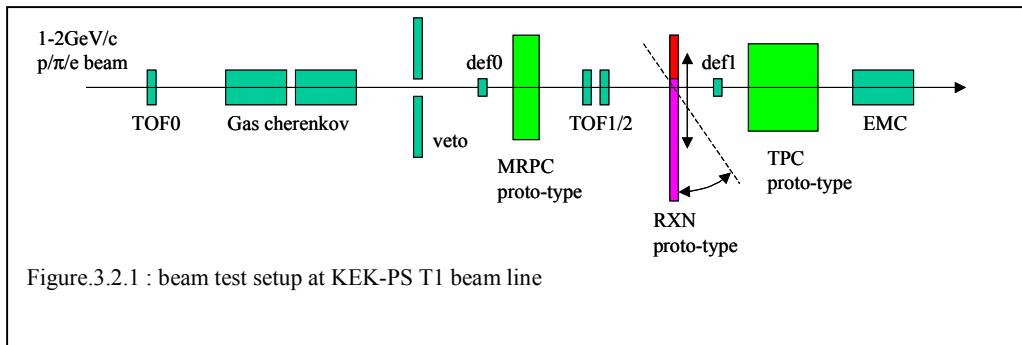
The Fig.3.2.1 shows the test beam setup at KEK-PS. The main aim of this proto-type beam test is to measure (0) the position/angle dependence of the pulse height per particle with several different detector configuration (1) scintillator with solid light guide, (2) scintillator with fiber read-out, (3) scintillator or cherenkov radiator. The Fig.3.2.2 shows the spectrum shape of PMT, scintillator and light guide. Scintillator (BC412) or UV (and non-UV) acryl (normally used for light guide) is used for a scintillation or cherenkov radiator. Acryl light guide or wavelength shift fiber (BCF92) is used to transmit lights to PMT. The Fig.3.2.3 shows several mechanical designs of the proto-type detector. Detectors with different shapes of the light guide are also tested. For the fiber read-out option, the fibers are embedded in every 1cm.

Figure.3.2.2. : spectrum shape as a function of wavelength for PMT, scintillator and light guide
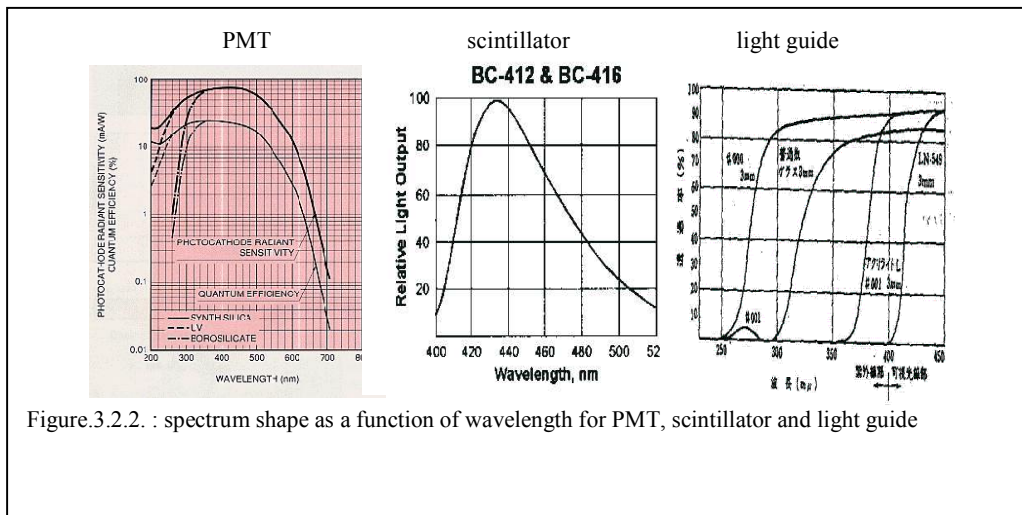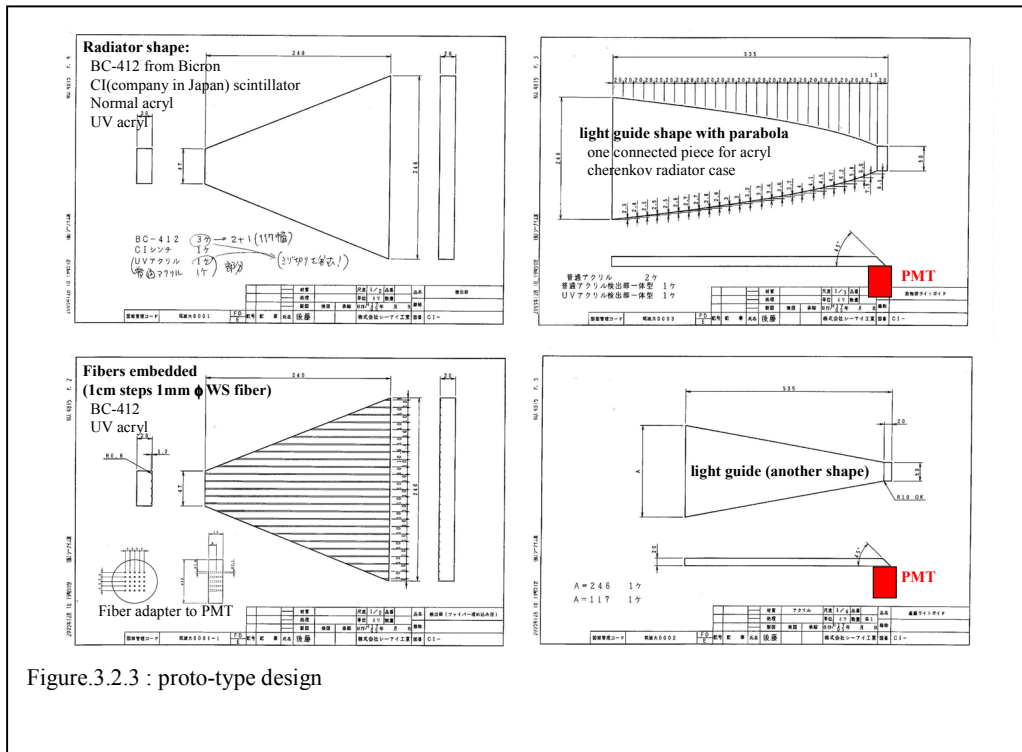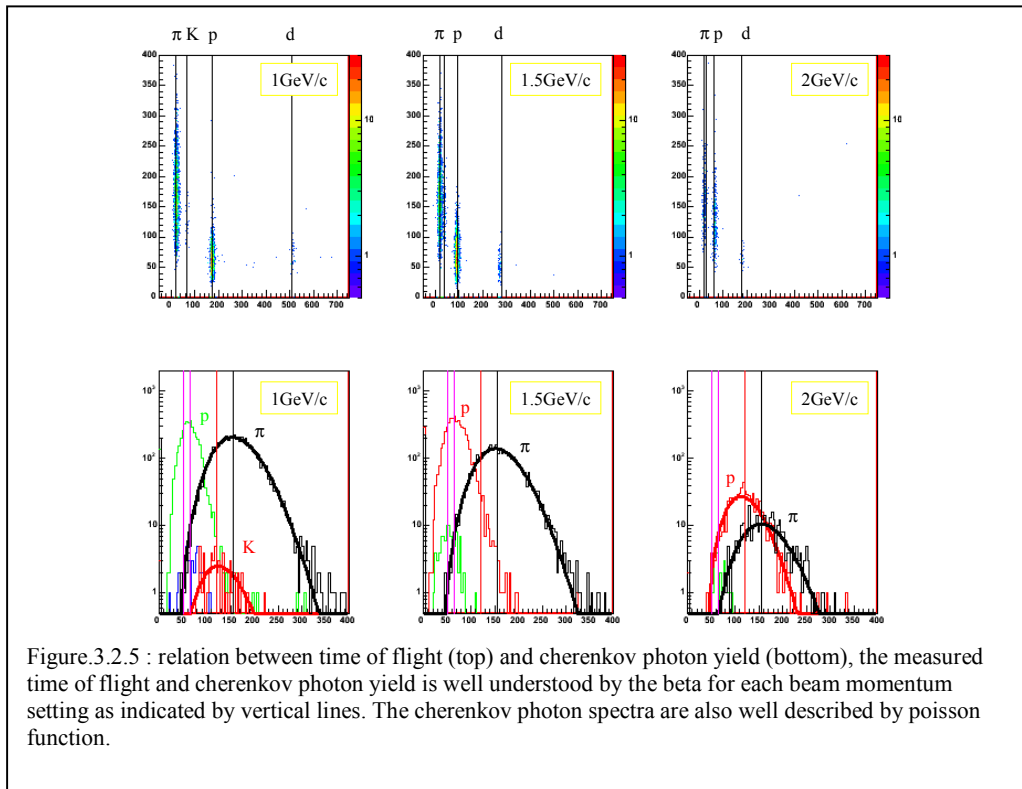
Figure.3.2.3 : proto-type design

The Fig.3.2.4 top panel shows pulse height distributions for various detector proto-types, scintillator with solid light guide (blue), scintillator with fiber light guide (red) and acryl cherenkov radiator (black). The bottom panels show the correlation between the pulse height and time of flight measurement, and the bottom-right panel is a zoom-in of the bottom-left panel for the small cherenkov pulse height. The Fig.3.2.5 shows correlation between time of flight and cherenkov pulse height (top) and cherenkov pulse height distribution (bottom), where both the time of flight and cherenkov photon yield are well understood as shown by vertical lines for each beam momentum setting from left to right panels. Poisson function fitting were performed to extract the cherenkov photon yield. The Fig.3.2.6 shows the resulting position dependence of pulse height, scintillator with solid light guide (top), scintillator with fiber light guide (bottom) and UV acryl cherenkov radiator (middle). The vertical axes are pedestal subtracted ADC, and corresponding measured photon yield with (1) scintillator with solid light guide is about 500pe, (2) scintillator with fiber light guide is about 20pe, (3) UV acryl cherenkov radiator is about 7pe.

Beam is 1cm² and perpendicular at the center of the detector, we compare three options:

2cm BC412 scintillator + solid light guide

2cm BC412 scintillator + BCF92 fiber

2cm Acryl cherenkov + solid light guide

Pedestal (~50) not subtracted

Figure.3.2.4 : pulse height and time of flight distributions for 3 detector options. Beta dependence of scintillation lights as well as cherenkov lights are clearly seen.

Figure.3.2.5 : relation between time of flight (top) and cherenkov photon yield (bottom), the measured time of flight and cherenkov photon yield is well understood by the beta for each beam momentum setting as indicated by vertical lines. The cherenkov photon spectra are also well described by poisson function.

Figure.3.2.6: position dependence of pulse height for 3 detector proto-types.

Based on the beam test, we are able to make decision among the following four options:

1. 2cm Acryl cherenkov + fiber guide.
   - 14 pe for 4cm thick cherenkov. At HV=2kV, corresponding to ~2-4mV signal which is too small to be considered.
2. 2cm Acryl cherenkov + solid light guide
   - Large weighting effect due to angle of incidence effect. Light guide can have too much weight.
   - Light guide does not allow the flexibility of grouping/relocate PMTs.
   - Large non-uniformity if light collection to worsen the reaction plane resolution.
3. 2cm BC412 scintillator + 2cm convertor + solid light guide
   - need to use converter as required by scintillator: 64kg of lead.
   - Light guide does not allow the flexibility of grouping/relocate PMTs.
   - Non-uniformity if light collection to worsen the reaction plane resolution.
4. 2cm BC412 scintillator + 2cm convertor + BCF92 fiber
   - Reasonable S/N ratio.
   - Fiber allows flexibility to group/relocate PMT
   - Light collection is uniform, attenuation is easy to calculate/calibrate.

We decide to adopt option 4, i.e. 2cm BC412 scintillator + 2cm convertor + BCF92 fiber, for the final detector design.

3.3 Detector Configuration

The reaction plane detector will be a paddle type detector situated in front of the nosecone. The active area will be composed of plastic scintillating material. BC-412 has been used for simulation and testing purposes. The scintillator will have a thickness of 2cm and will be positioned at 38<|z|<40 cm. The inner edge of the scintillator will begin at r=5 cm and extend to r=33 cm. This allows the detector to cover a pseudorapidity range of 1.0<|η|<2.8. This coverage was chosen to balance the competing effects of maximum acceptance and jet induced autocorrelations with the central arm. As figure 2.1.16 in the simulations section shows, the reaction plane resolution is only weakly dependent upon the segmentation of the detector in phi as the number of sectors increases above 8. However, the effect of dead channels is minimized for a segmentation greater than 10.   For this reason the proposed reaction plane detector will be segmented into 12 sectors in phi. Each phi sector will be further divided into two radial sections. The inner eta segment will extend from a radius of 5cm to 18cm and the outer eta segment will continue from 18cm to a radius of 33cm. This effectively divides the detector into two rapidity regions, 1.0<η<1.5 and 1.5<η<2.8, which will allow the possibility to study the effect of jet induced autocorrelations on the reaction plane determination if sufficient photomultiplier tubes are available to read out both eta segments independently.
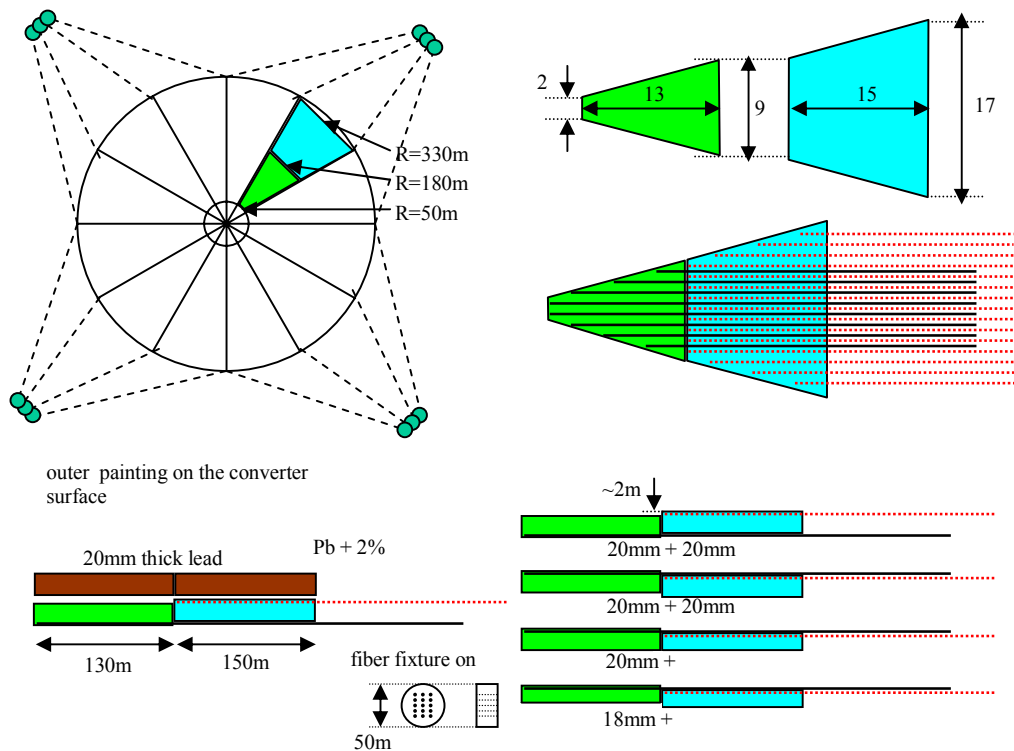

Figure 3.3.1: Front view of the reaction plane detector.

Embedded fiber light guides made of BCF92 will connect the plastic scintillator to the photomultiplier tubes. An adapter in which the fibers can be embedded will be used to join the fibers to the photomultiplier tube. The use of fiber light guides has several advantages for this detector design. Most significantly, the light collection along the radial length of the scintillator is more uniform using embedded fibers than solid light guides. Additionally, the fibers allow for flexibility in the final positioning the photomultiplier tubes. This is important due to the sensitivity of the tube response to the magnetic field and will allow the tubes to be repositioned if necessary after installation. Figure 3.2.2 shows a side view of the reaction plane detector situated in PHENIX.
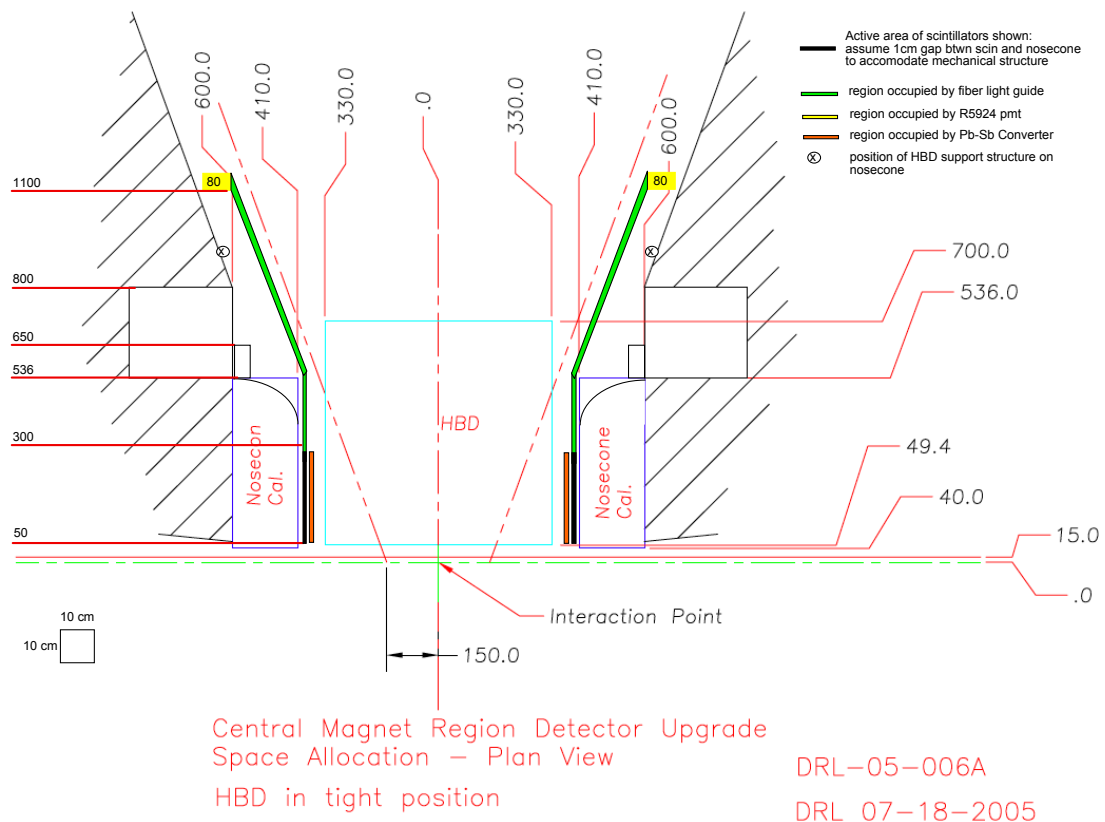

Figure 3.3.2: Side view of the reaction plane detector in PHENIX.

Mesh dynode photomultiplier tubes, Hamamatsu R5924, will be used due to the strength of the magnetic field in the region where the reaction plane detector will be positioned. As discussed in Section 3.1, the performance of the tubes is greatly affected by their orientation with respect to the magnetic field lines. This provides stringent constraints on the placement of the tubes. In order to maximize tube performance and minimize background in the central arm acceptance, the photomultiplier tubes will be placed parallel to the beam pipe at r = 110 cm and z = 61 cm. The performance of the

tubes at this position has been tested in PHENIX as described in section 3.1.4. A possibility exists for borrowing a set of photomultiplier tubes from KEK experiment E325. These tubes are model number R5524 and possess similar properties to the R5924. Bench top tests of the R5524 will be needed due to the age of the tubes.

Simulations have shown that the reaction plane resolution is enhanced by the addition of a converter in front of the scintillator active area. There exists a gap of 7 cm in the z-coordinate between the nosecone and HBD volume. Allowing for 1 cm of buffer region between the HBD and the reaction plane detector and 2 cm of plastic scintillator, there remain 4 cm of space. Allowance must be made to accommodate the mechanical support of the reaction plane detector, therefore it is proposed that a 2 cm thick lead-antimony composite converter be installed directly in front of the scintillator. The addition of 2-3% of antimony hardens the converter material and will improve the mechanical stability of converter when it is mounted.

A LED calibration system will be used online to monitor the stability of the detector and during installation to test the photomultiplier tubes. It is proposed that the same system be used for reaction plane detector as is used in the Aerogel and MPC subsystems. The driver board for this system is a NIM module with 8 output channels. Each of these channels can be subdivided further into 8 sub-channels using small dispatch board, therefore each board can drive 64 LEDs. A maximum of 48 channels will be needed by the reaction plane detector.

3.4. Readout Electronics

To instrument the RXNP phototubes with PHENIX-compatible readout electronics the obvious choices would to be use one of the existing FEM for the PMT-based detectors, particularly[1] the BBC or the EMCal. The BBC readout electronics offer superior timing resolution and a proven LLVL-1 system for triggering, whereas the EMCal electronics emphasize linearity and dynamic range while providing some LVL-1 triggering capability. Since the RXNP detector is not intended to serve as a trigger or start timing detector (in contrast to the old NTC systems in the same location), but its physics performance does depend on the digitization of the light output being linear over a fairly wide dynamic range (approx. 200 to 1), the EMCal system is the natural candidate. Practical considerations reinforce this choice, in that time is currently available from EMCal FEE experts for the RXNP project, while BBC FEE experts are sufficiently rare and otherwise committed as to be effectively unavailable.

In the Reference Design presented here the RXNP would be read out by a single EMCal FEM, which would require at most two ASIC daughter cards. This FEM will sit in a new rack intended to hold the HBD high voltage system, and which is currently being installed in a location atop the upper field return piece (the "bridge") of the central magnet. The HBD HV rack will have sufficient space and cooling capacity for one

---

[1] We have not separately considered the RICH electronics, which are in many ways similar to the EMCal.

EMCal FEM. Low-voltage DC power (+/- 5V, with approx. 50 watts on +5) will be provided by standard PHENIX supplies drawing on AC power available in the rack. The exact cable run from the RXNP PMT's to the bridge rack remain to be specified, but can probably share space with the trays for the HBD HV supply cables. We do not expect this to present a problem.

The RXNP FEM must be included in a PHENIX granule, of course. To simplify the design and minimize work the RXNP will be included as part of the already-existing FCAL granule, which also uses EMCal electronics. Timing modebits from the FCAL GTM can be actively or passively split, and a DCM of the correct type is available in the DCB currently receiving the FCAL FEM output. Optical fibers are already available and in place between the rack room and the central magnet (left over from the MVD).

Interference with the FCAL system is absolutely minimal since the RXNP FEM can be timed in independently of the rest of the FCAL system just by changing the length of the fiber from the GTM; this can be done even while the beam is on. Some work will be required to adjust the zero suppression table of the readout DCM so that any empty ASIC card channels are not read out, but this problem has already been solved for the PbSc monitoring FEM's. Normal programming of the RXN FEM, ie DAC settings, will have to be carried out, but there is no reason to expect these to be very different from those used in the EMCal system. An ARCNET pathway will have to be established to the RXN FEM; this is currently TBD, but should not present a serious problem.

From experience with the T0 counter using similar scintillator and similar phototubes operated in a linear range, we expect one RXNP detector element to produce, nominally, 20 pC of charge per MIP. This can easily be processed by an EMCal FEM to provide single-MIP resolution. The nominal full-scale input for an EMCal channel is 512 pC, and the dynamic range (ie full-scale to noise level ratio) is between approx. 1000-1 (using a single gain range) and 10,000-1 (using both gain ranges). In designing the cable plant for the RXN attention must be paid to several issues. Mechanically the EMCal ASIC daughter boards accept analog input on four-wide mini-coax connectors. Electrically the analog inputs provide 93 ohm termination, and the cable run is of sufficient length (5-10 meters) that a clean impedance match will probably be required to preserve the rising edge of the signal to allow timing measurement at the nanosecond level. Satisfying both of these constraints will require coordination with the tube base design. Some custom work may be necessary at the cable ends, but for this small number of channels the amount of labor should not be large.
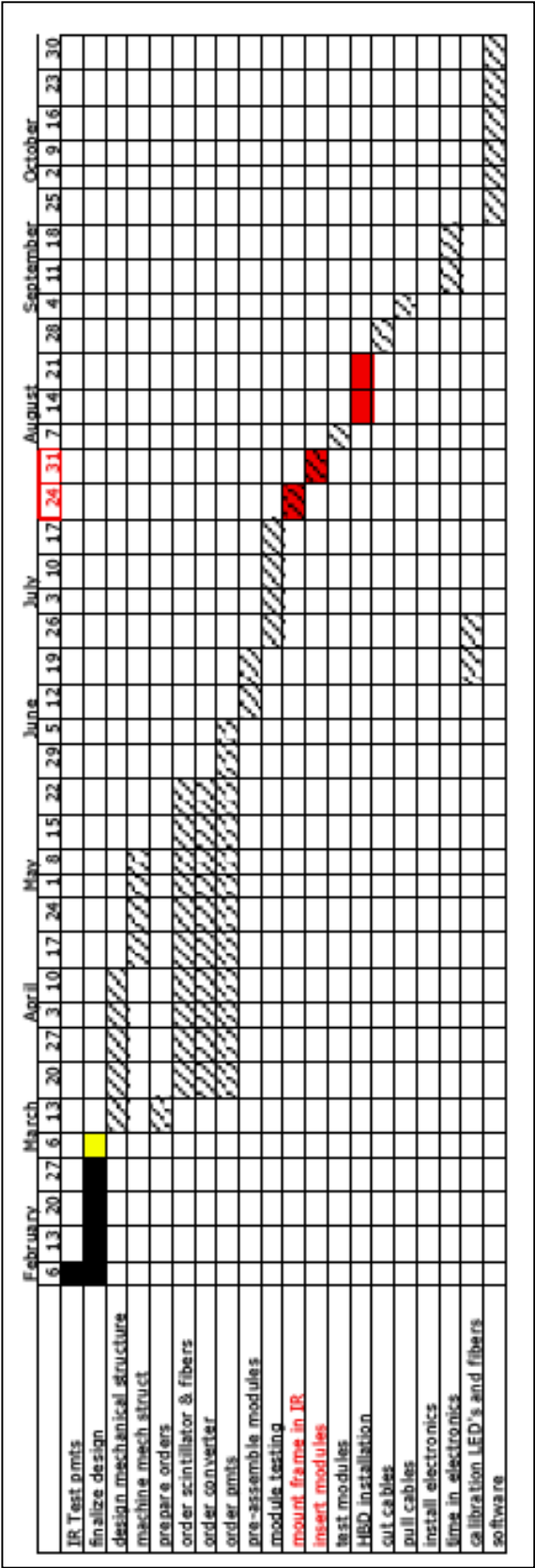
4. Resources, Costs and Schedule

Total cost of the proposed RxNP is <u>~$90k w/new PMTs or $50k w/ KEK E325 PMTs</u>. It is broken down into the following:

- **scintillator paddles and light guide: $30k**
  - 2 eta_segments X12 slats X 2 (arms) + 4 backups: $30k for scintillator and light guide   material + paddle production in Japan.
- **pmt: $40k w/new PMTs and $0 w/E325 PMTs**
  - Optioin#1: $40k
    - 1 eta_segments X12 slats X 2 (arms) + 4 backups = 28 PMTs
      - 14 R5924 at BNL + 4 at Tsukuba Univ=18: $0k
      - Need 10 additional tubes. Each tube: $4k. Total will be $4k X 10 = $40k
  - Option#2: $0
    - 2 eta_segments X12 slats X 2 (arms) + 4 backups = 52.
    - Possible support of ~48 R5542 from KEK E325. Official request from Hideto to KEK. Better performance than R5924 except older.
    - Available R5924 can be as backup.
- **lead converter: $4k**
  - Lead + sb from Japan.
  - machining and material price unknown yet. Assuming it's similar to the earlier quote for copper.
- **Cables and connectors + FEM LV power supply: ~ a few $k**
- **Design, build and mounting supporting structure for mounting the detector: a few $k**
  - Best option is Don Lynch to design and PHENIX technician to build.
- **LED calibration system: $1k**
  - Steve Boose driver board (MPC). 1 board can drive 64 channels. $1k/board
- **Travel funds: $11k**
  - 2-3 students from abroad (e.g. Tsukuba) and other states.travel to BNL and stay for 2 months for testing and commissioning and doing shift of the detector.
  - per diem: $1k x 3 people x 2 months=$6k
  - housing: $2k
  - flight ticket: $3k
- **Free items:**
  - **HV: $0**
    - From existing
  - **Test stands and lab: $0**
    - Hi-bay at BNL physics department or PHOBOS paddle test lab at BNL chemistry department.
  - **FEMs: spares**
  - **Software: $0k.**
    - Simulation and offline software, e.g. fun4all
    - Online Monitoring. Replace the NTC software?
    - HV control. Using the NTC.

The following table shows the currently planned schedule for the detector construction:

Acknowledgments